U.S. DEPARTMENT OF COMMERCE
Elliot L. Richardson, Secretary

NATIONAL OCEANIC AND ATMOSPHERIC ADMINISTRATION
Robert M. White, Administrator
ENVIRONMENTAL RESEARCH LABORATORIES
Wilmot N. Hess, Director

NOAA TECHNICAL REPORT ERL 356-WMPO 7

Rainfall Estimation From Geosynchronous Satellite Imagery During Daylight Hours

CECILIA G. GRIFFITH
WILLIAM L. WOODLEY
STEPHANIE BROWNER
JOSE TEIJEIRO
MICHAEL MAIER
DAVID W. MARTIN
JOHN STOUT
DHIRENDRA N. SIKDAR

BOULDER, COLO.
February 1976

For sale by the Superintendent of Documents, U. S. Government Printing Office, Washington, D. C. 20402

NOTICE

The Environmental Research Laboratories do not approve, recommend, or endorse any proprietary product or proprietary material mentioned in this publication. No reference shall be made to the Environmental Research Laboratories or to this publication furnished by the Environmental Research Laboratories in any advertising or sales promotion which would indicate or imply that the Environmental Research Laboratories approve, recommend, or endorse any proprietary product or proprietary material mentioned herein, or which has as its purpose an intent to cause directly or indirectly the advertised product to be used or purchased because of this Environmental Research Laboratories publication.

CONTENTS

CONTENTS (contd.)

ILLUSTRATIONS

ILLUSTRATIONS (contd.)

ILLUSTRATIONS (contd.)

TABLES

ACRONYMS

ATS	Applications Technology Satellite
DC	Contour division
DCU	Digital count
DU	Density control unit
ESMR	Electronically Scanning Microwave Radiometer
FACE	Florida Area Cumulus Experiment
GARP	Global Atmospheric Research Project
GATE	GARP Atlantic Tropical Experiment
IR	Infrared
I^2S	International Imaging Systems
McIDAS	Man Computer Interactive Data Access System
NESS	National Environmental Satellite Services
NHEML	National Hurricane and Experimental Meteorology Laboratory
RFC	Research Facilities Center
SFSS	Satellite Field Services Station
SMS	Synchronous Meteorological Satellite
SSEC	Space Science and Engineering Center
VIMHEX	Venezuelan International Meteorological and Hydrological Experiment
WINDCO	Wind computation program

SYMBOLS

A_C — Cloud area (km^2) as measured from the satellite image.

A_E — Echo area (km^2) as determined from radar; in this study, defined by the 1 mm/hr rainrate.

a_i — The fraction of a cloud mass (usually a hurricane) defined by higher brightness contours:

$$a_i = \frac{A_J - A_{J+1}}{A_{80}},$$

where A_J and A_{J+1} are satellite cloud areas measured at two successive brightness contours. For a_1, A_J is always defined to be A_{80}.

A_{80} — Cloud area (km^2) defined by the 80 digital count contour on the ATS-3 images. A_{90}, A_{105}, A_{120}, etc. are similarly defined.

b_i — An empirically derived coefficient which accounts for higher brightness levels above the 80 DC contour:

$$b_i = \frac{A_{80}}{A_J},$$

where A_J is the satellite-measured cloud area at a defined digital count level. For b_1, $A_J = A_{80}$.

$\overline{d}$ — Mean cross section (km) of the hurricane in the direction of storm motion, and defined by the 80 DC contour.

$\overline{D}$ — Daily average hurricane rainfall (mm/day).

f_i — The fractional cloud mass brightness level covering the target (T) over which the rain calculation is being made. It is defined to be:

$$f_i = \frac{A_{JT} - A_{(J+1)\ T}}{A_{JC} - A_{(J+1)\ C}}$$

where J and J+1 denote two successive brightness levels, A_{JT} is the area at J DC within the target, A_{JC} is the area of the cloud mass and similarly for the remaining quantities. The lowest contour is always 80 DC.

GT — Groundtruth estimate of rain.

I — Rain intensity coefficient in the echo area-rain volume relationship which accounts for echo growth trend. Units are m^3/km^2.

r_V Rain volume per 5 minutes defined by three empirical functions of echo area and echo growth trend. Units are m^3/5 min.

R_V Rain volume as defined for r_V, but for a specified time period (e.g., 30 minutes, 24 hours, etc.). Units are m^3.

S Satellite estimate of rain.

$\overline{V}$ Mean speed of the hurricane (km/day) over the period of calculation.

ABSTRACT

A method to estimate rainfall from visible geosynchronous satellite imagery during daylight hours has been derived and tested. Based on the finding that areas of active convection and rainfall in the tropics are brighter on the satellite visible photographs than inactive regions, ATS-3 images were calibrated with gage-adjusted 10-cm radar data over south Florida. The resulting empirical relationships require a time sequence of cloud area, measured from the satellite images at a specified threshold brightness, to calculate rain volume over a given time.

Verification tests were performed over two areas in south Florida that differ in size by an order of magnitude (1.3×10^4 vs. 1.1×10^5 km^2). Satellite rain estimates were made and compared to rain volumes measured by a combined system of gages and radar. Accuracy did not appear to be a function of the size of the region over which the estimates were made, but was found to be a function of time. For hourly comparisons, the satellite and groundtruth rain estimates differed by an absolute factor of two or greater; over longer periods ($\geq$ 5 hours) accuracy improved, being within an absolute factor of 1.5 of the groundtruth measurement.

Two additional tests for which groundtruth was available were also made. By means of the VIMHEX gage network, satellite estimates were calculated on 9 days to test the applicability of this scheme to a tropical area other than the region of derivation. Comparison with groundtruth resulted in a difference of an absolute factor of 2.3, in the mean. However, the quantity and quality of satellite and groundtruth data for the Venezuelan tests were less satisfactory than those for Florida.

In the second case, rain was calculated over the country of Honduras during the 5 days of hurricane Fifi's passage. When compared to the gage data, the daily satellite estimates ranged from a 19 percent underestimate to a 72 percent overestimate, but differed by only 13 percent at the end of the period.

Use of this method as a forecasting tool for hurricane-caused flooding is investigated in a study of selected hurricanes: Debbie (1969), Celia (1970), Edith (1971), Agnes (1972), Carmen (1974), and Fifi (1974). Relative rankings among these storms of total daily rain volume and daily area-averaged rain depth as calculated from satellite images were made. Agnes, Carmen and Fifi were found to be relatively wet storms, with Debbie, Celia and Edith being relatively dry.

RAINFALL ESTIMATION FROM GEOSYNCHRONOUS SATELLITE IMAGERY DURING DAYLIGHT HOURS

Cecilia G. Griffith, William L. Woodley, Stephanie Browner
Jose Teijeiro and Michael Maier
National Hurricane and Experimental Meteorology Laboratory

and

David W. Martin, John Stout, and Dhirendra N. Sikdar[1]
Space Science and Engineering Center, University of Wisconsin-Madison

1. INTRODUCTION

The estimation of rainfall over extensive areas is important to several disciplines. Meteorologically such estimates are needed for improved calculations of both the water balance over oceans and continents, and the heat balance of the atmosphere. In the past, global rainfall has been calculated as a residual in these budget calculations. Riehl (1954) points out that this residual is of utmost importance because it is the transfer of latent heat from the ground to the atmosphere, made possible by condensation and rainfall, that balances the earth's loss of heat to space. It would be desirable to measure this important term directly. Of more immediate concern, better global rain measurements are necessary to determine the hydrologic and agricultural potential of remote areas, to detect excessive rains for flood warnings, and to evaluate and predict the flood potential from the rains of tropical cyclones.

It is not always possible to measure rainfall by conventional means. Although raingages are used extensively, worldwide, for rain measurement, it is difficult to install them in rough terrain, and virtually impossible over water areas. In many instances, the available raingage readings are representative of the immediate environment only. For example, mountain stations are subject to orographic effects and island stations are subject to diurnal heating. Island rainfall is frequently unrepresentative of precipitation over the oceanic surroundings. Even over flat terrain, readings from isolated raingages may not be characteristic of the true area rainfall, particularly so if the precipitation is from convective clouds (Woodley et al., 1975).

Radar is receiving increased attention for rain measurement. It provides greater areal coverage than raingages, but lesser accuracy. Ground-based radars still cannot scan the vast oceanic areas. Furthermore, radar measurement of rainfall requires a degree of technical sophistication found only in limited areas of the globe.

With the advent of the U.S. satellite program in 1960, the potential for forecasting was immediately obvious. As better resolution sensors were orbitted, special applications were investigated, rain estimation being one. Various estimation schemes have been devised using visible or infrared imagery from geosynchronous or polar orbiting satellites. Martin and Scherer (1973) provide a complete review, up to 1973, of all methods to estimate rainfall from either visible or infrared satellite imagery. Since then,

[1]Dr. Sikdar is now at the University of Wisconsin-Milwaukee.

data from the Nimbus 5 microwave radiometer (ESMR), have been used to delineate rainfall over ocean areas (Allison et al., 1974).

The results reported in this document have been obtained with ATS-3 imagery. Data from geosynchronous satellites are ideal for meteorological problems, because the complete life cycle of a cloud can be documented. Moreover, earlier studies (Martin and Suomi, 1971; Woodley and Sancho, 1971; Woodley, Sancho and Miller, 1972) have indicated that the bright regions on visible photographs of the ATS correlated well with regions of rainfall.

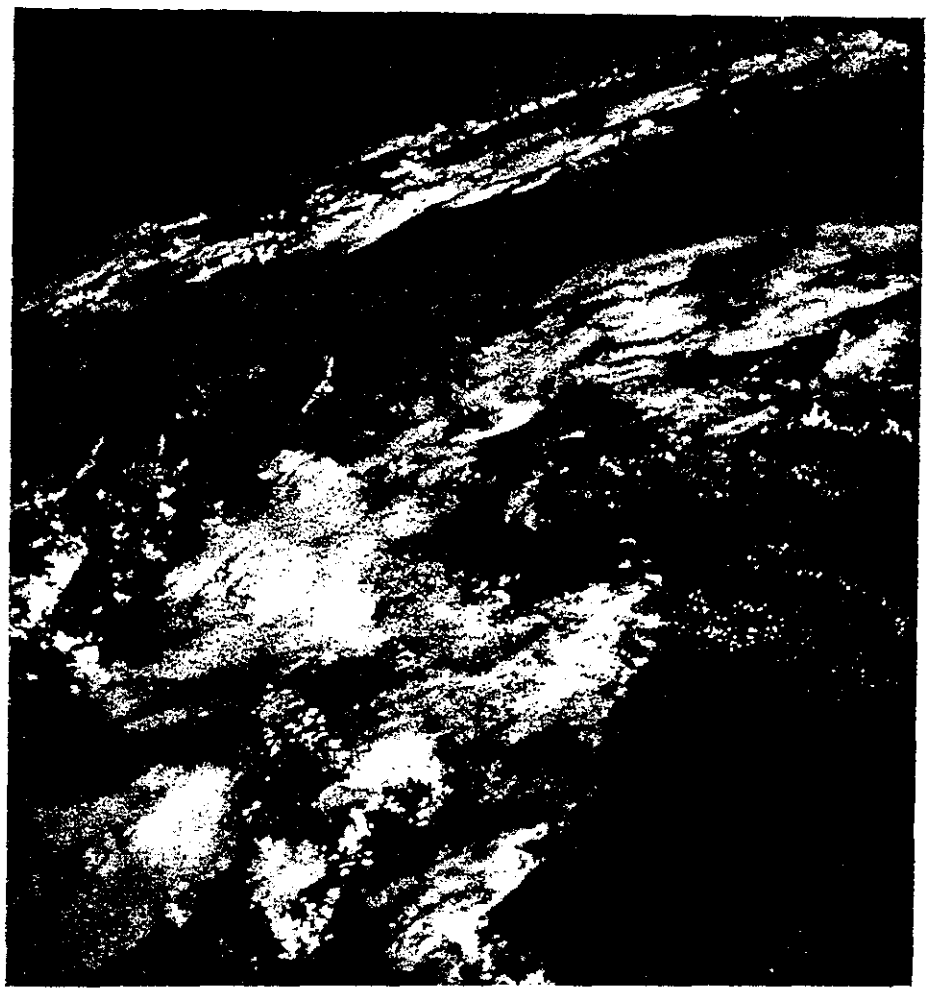

Figure 1. An example of active convection growing above the cirrus layer, from a NASA photograph.

Critics of visible data have contended that cirrus contamination would present a grave problem for rain estimation, because there would be little or no difference in brightness between relatively thick cirrus and active convection. But growing convective towers do penetrate the cirrus layers, as can be seen in the dramatic NASA photograph of figure 1. Furthermore, cloud stage of development information obtained from the geosynchronous time histories is invaluable for offsetting the masking effects of cirrus.

The assumption of this estimation scheme - bright clouds are thicker and thick clouds are wetter - is supported by the results of Griffith and Woodley (1973) and Reynolds and Vonder Haar (1973), although neither study indicates that a unique correspondence between cloud brightness and rainfall can be inferred. Despite the fact that the physical link could be better understood, it will be demonstrated that daily rainfall can be estimated to within an absolute factor of 1.5 or better over an area of $10^5 km^2$.

To some extent, the estimation accuracy sought by any scheme is a function of the derived data's ultimate use. For example, long term global precipitation estimated would require an accuracy of better than 30% (S. Manabe[2], personal communication), whereas daily precipitation estimates over agricultural areas would need accuracies of better than 20% (N. Strommen[3], personal communication). At the inception of this work it was held that estimates of the same accuracy as the groundtruth would be very good, given the limitations of the satellite data. From the tests shown here, it would be reasonable to believe that accuracies of $\pm$ 20 to 30% could be achieved by higher resolution data or further refinements.

Although this method is properly limited to the estimation of Florida convective rainfall during daylight hours, the relationships may be valid for other areas with similar convective regimes. Tests of this hypothesis have been made.

2. RESEARCH TOOLS

To derive this method we measured several quantities from a satellite image, and then related these quantities to rain volume. The data of this study were satellite images; the research tool was a measuring device suitable for the type of satellite image processed; a gage-radar groundtruth system of rain measurement was the means of verification. The specifics of the three items are presented here.

To follow the time evolution of clouds, this method requires a sequence of satellite images. When the project began, the only geosynchronous satellite observing Florida was the Applications Technology Satellite, ATS-3. Thus, the majority of the results described in this document have been derived from ATS imagery. This satellite[4], launched in November 1967 and operational until November 1974, had a 2 n mi resolution at the time of launch. Unfortunately, the spatial resolution had degraded since then. From mid-1971 until cessation of operations, the satellite had been in an excellent position for viewing Florida, because it was located at 70°W and the equator. During the periods of the Florida studies, the summers of 1972 and 1973, the ATS spin-scan radiometer, orginally designed to transmit images in three visible channels, was sensing in the green channel only. No geosynchronous infrared (IR) data were available until the launch of the Synchronous Meteorological

[2]NOAA/Geophysical Fluid Dynamics Laboratory

[3]NOAA/Center for Climatic & Environmental Assessment

[4]A complete descripiton of the ATS experiments is found in NASA's Meteorological Data Catalogs for the ATS, and in Warnecke and Sunderlin (1968)

Satellite (SMS-1) in late May 1974.

The time resolution of the ATS images is variable. The Suomi spin-scan camera utilizes the spin of the satellite to scan east-west across the earth. Successive scan lines fill in the earth's image from north to south as the optics of the camera are mechanically moved. With the ATS radiometer, the geographic starting point of an image is fixed at roughly 60°N. The time interval between two successive pictures depends upon the geographic coverage of the first image. A full disk image (nominally 90° N to 90° S) required 27 minutes. Shorter intervals indicate that less area in the southern hemisphere has been imaged. Most of the 1972 data were received at a frequency of one picture every 27 minutes. In 1973, after 1700 Z, the images generally are at intervals of 20 minutes (3/4 disk), with all others being full disk. This shorter interval allowed better temporal resolution for our studies.

Two types of ATS imagery have been used in this study. Taped satellite images, recorded at the Wallops Island, Virginia ground station, were processed at SSEC on McIDAS, the Man Computer Interactive Data Access System. NHEML utilized ATS photographic negatives recorded and processed at the Miami Satellite Field Services Station (SFSS). The taped images have the advantages of the full scale (0-255 digital count) brightness resolution, and lower noise levels. They can be remapped to the scale and projection of other data. Using McIDAS, navigations are generally more accurate, and images can be viewed in sequence. Details on McIDAS are in Smith (1974) and Chatters and Suomi (1975).

Although the ATS negatives have approximately one-quarter the brightness resolution of the tapes, and more noise due to transmission from Wallops Island to Miami, via Suitland, Maryland, with a false-color scanning densitometer they can be processed more quickly and inexpensively. The equipment is reliable and the processing straightforward. The densitometer used for this study is a Digicol, manufactured by International Imaging Systems. The instrument displays on a monitor (in either black and white or color) all or part of the image on a film transparency. Images can be enhanced and a particular brightness threshold can be color coded. Area is measured as a percentage of the monitor display; thus the Digicol's measuring capability is not suited for defining areas of individual clouds. A full description of the Digicol and of its operation is in Appendix A.

With the densitometer, ATS-3 negatives were magnified approximately 33 times by a 55 mm lens and a 2.5-cm spacer, and were displayed on the monitor so that a rectangle approximately 5° latitude x 6° longitude, centered on Florida, was in view. At this magnification, referred to as the Standard Height, the scan lines of the image were clearly visible. Table I lists all camera and Digicol DCU settings used with the ATS-3 negatives to achieve this magnification.

Developing and verifying a relationship between cloud area and rainfall depends upon a reliable system of convective rain measurement. Raingages in sufficient density are ideal for areal convective rain measurement. Unfortunately, it is impractical, if not impossible, to gage an area large enough to serve as a standard for estimates of rainfall from satellites. Consequently,

Table 1. Camera and DCU settings for a 33x magnification of ATS-3 negatives (Standard Height)

Lens Configuration:	55 mm Nikon and 2.5-cm spacer
Camera focus:	24.1 cm
Camera height[a]:	3.75 cm[b]
Camera f-number[c]:	f/16
RANGE[c]:	3
DCU mode:	DENSITY
Kodak gray wedge steps for DCU calibration:	#3 and #11.
Area viewed on monitor:	6.1° longitude x 4.5° latitude, when centered on Miami.

[a]Given the camera focus, camera height is adjusted until the scan lines of the negative are sharp.

[b]Height is measured from the lens nadir to the light table.

[c]These numbers may change because of internal settings in the Digicol.

we have chosen gage-adjusted S-band radar measurements of rainfall as described by Woodley et al. (1975) as the standard of comparison for satellite rain estimates. The radar provides the equivalent of an infinitely dense raingage network and a first estimate of the true areal rainfall. Raingages distributed in clusters provide for adjustment of the radar rain estimates.

3. PROCEDURES

3.1 Normalization of Photographs

Because of the variability among ATS negatives, a normalizing technique is applied to all negatives. Four normalizing standards have been tested and are described in Appendix C. The normalizing procedure itself is listed in section A4.6. The reader is referred to Mosher (1973) and Martin and Sikdar (1974) for details of the normalization scheme that has been applied to digital satellite data.

A standardization procedure is necessary because line noise, signal amplitude, recorder response, and/or photochemical processing vary somewhat from image to image. The standard presently in use is the brightest cloud (on each negative) within 1 hour of longitude of the geographic region of interest. The standard brightest cloud density of 1.09 density units (DU) defines a correction factor, c, so that $c = 1.09 - \rho_{cb}$, where ρ_{cb} is the density of the brightest cloud on a particular image. This value, c, is algebraically added to all density measurements made on that image. If the gray range of the negative is brighter than average, c will be negative and all measured densities will be reduced by the value of c. Likewise, if the image is darker than usual, all densities will be increased by c.

The value of a standardization procedure is demonstrated in figures 2 and 3. Figure 2 is a graph of the density data prior to standardization, and figure 3 is the same data after standardization[5]. Some decrease in the scatter can be seen.

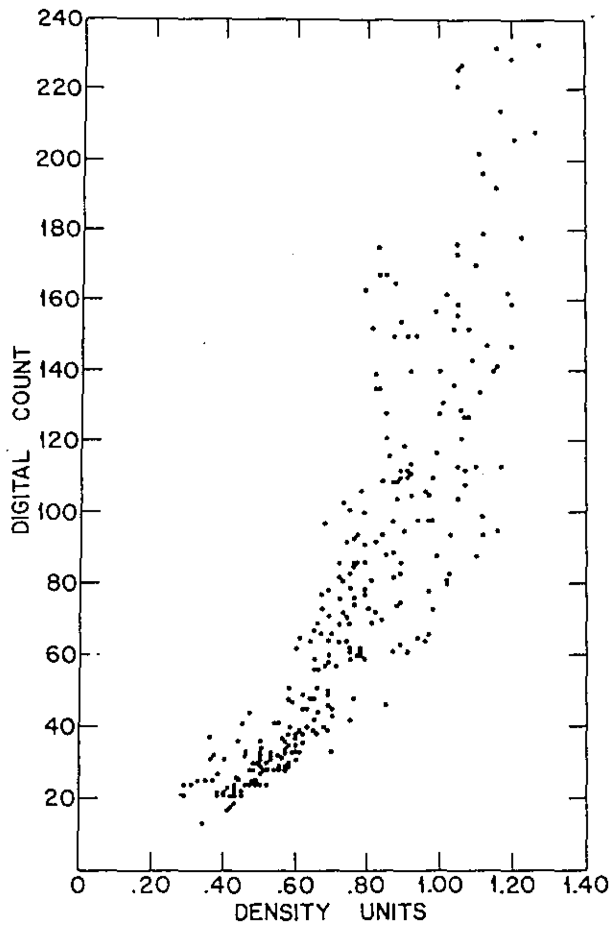

Figure 2. Density unit - digital count relationship for the ATS-3 Standard Height before salt flat normalization.

[5] The data of figure 3 have been standardized using the salt flat, Salar de Uyuni. See section C3 for details. Standardization by the brightest cloud gives comparable results.

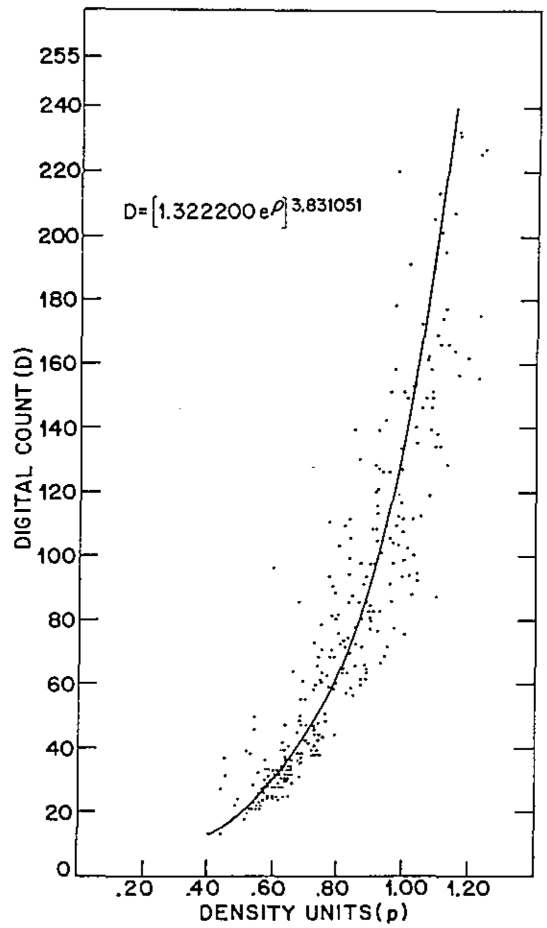

Figure 3. Density unit - digital count relationship for the ATS-3 Standard Height after normalization.

3.2 Brightness Versus Rain Frequency

To determine a brightness cutoff by which to define cloud area, a study of echo occurrence beneath a satellite-observed bright cloud mass as a function of the maximum brightness within the cloud was undertaken on McIDAS. The measurement of maximum digital count within a cloud, as well as the superposition and comparison of cloud and echo displays to ascertain echo occurrence, were performed on WINDCO (the Wind Computation program), the forerunner of the McIDAS. Six days in 1972 were studied - Julian days 192 (10 July), 195 (13 July), 200 (18 July), 222 (9 August), 228 (15 August), and 230 (17 August). Satellite cloud data were the taped ATS images, and radar data were microfilm of the Miami WSR-57 radarscope. The WSR-57 is a 10-cm wavelength radar; thus, its echoes at a 0.5^{o} antenna elevation represent precipitating cloud only.

Figure 4 shows the initial analysis of these types of data. The data have been grouped into intervals of 10 digital counts (DC), and plotted versus the percentage of clouds in that interval having echoes. The number in

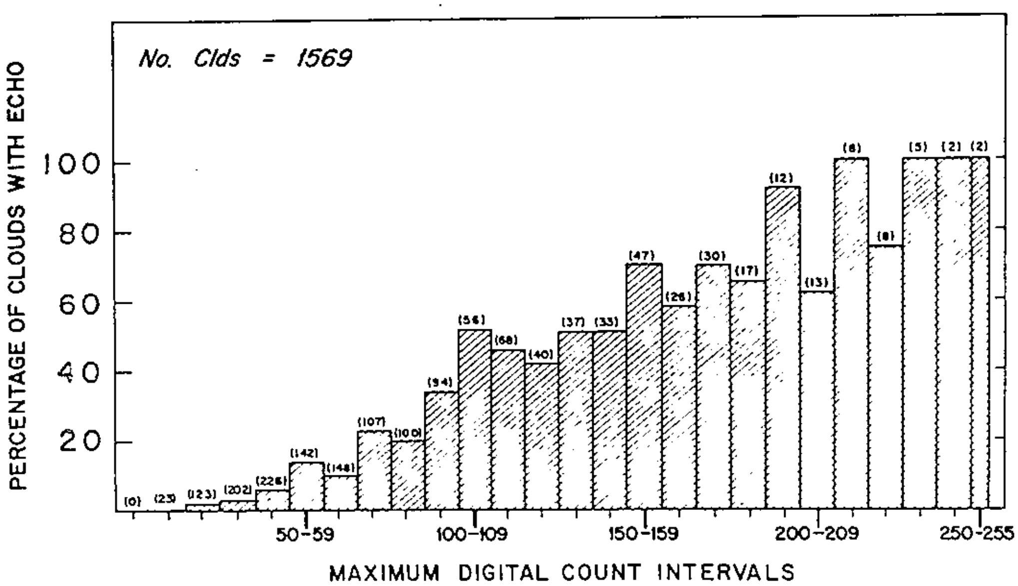

Figure 4. Echo frequency as a function of maximum digital count within a cloud. Data have been analyzed in intervals of ten digital counts. The numbers in parentheses indicate the total number of clouds in each interval.

parentheses above each bar indicates the number of clouds in that brightness interval. As expected, the fraction of clouds with echo in each interval increases with digital count (i.e., with brightness). The fluctuations in echo percentage above 150 DC are probably due to cirrus contamination in those intervals.

More informative presentations of these data are given in figures 5 and 6. Unlike figure 4, which is an interval-by-interval analysis, the data in figures 5 and 6 are cumulative, from 255 DC and from 0 DC, respectively. The data have been plotted by successively including intervals of 10 DC, 255-250, 255-240, 255-230, etc. in figure 5, and 0-9, 0-19, 0-29, etc, in figure 6.

Figure 5 indicates the percentage of clouds reaching a given digital count, or higher that have echoes associated with them. For example, 68 percent of the clouds that have a maximum digital count between 140 and 255 have echoes. Figure 6 demonstrates the percentage of clouds at a given digital count, or less, that have echoes. Thus, 15 percent of those clouds with a maximum digital count of 139 or less have associated echoes.

Using figures 5 and 6, a brightness threshold of 80 DC was chosen. At this threshold, 48 percent of the clouds with a maximum digital count between 80 and 255 DC have echoes, while only 9 percent of the clouds with a maximum digital count of 79 DC or less have echoes. Thus, some clouds at or above this threshold will not be precipitating, while other precipitating clouds will be missed at this cutoff. Figures 5 and 6 merely give an indication of

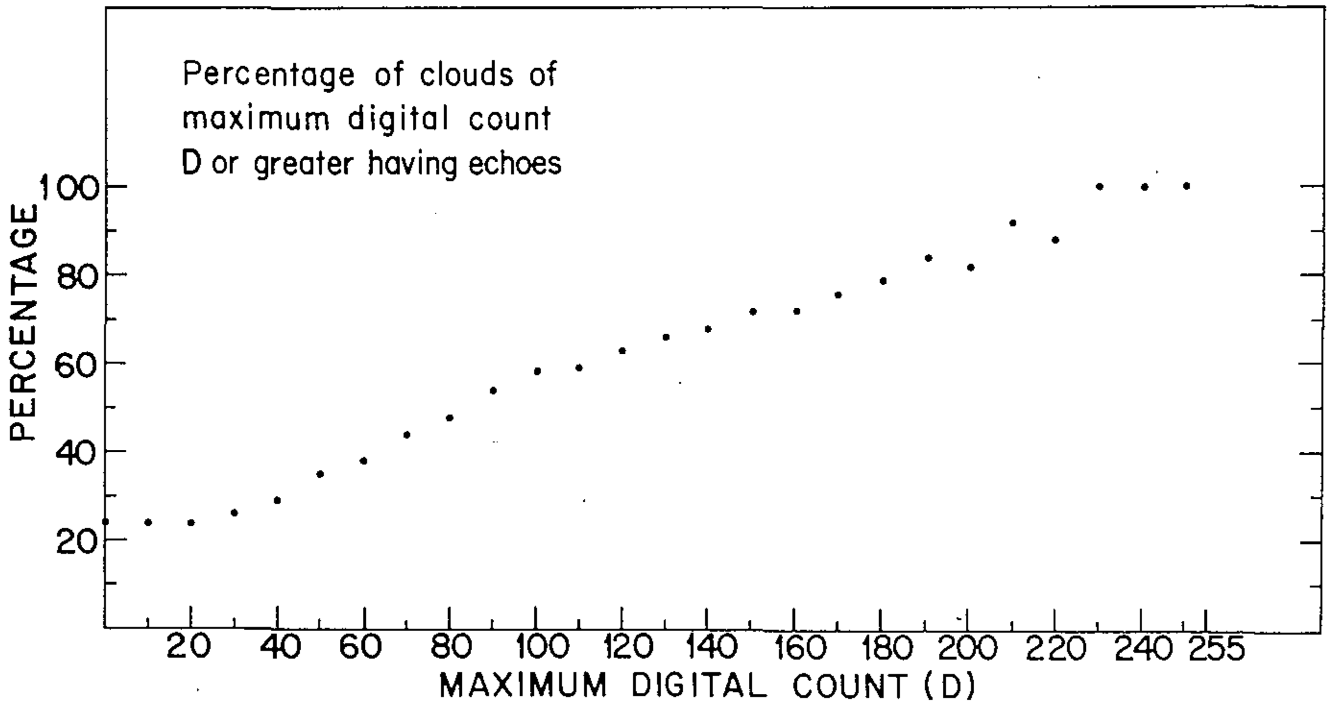

Figure 5. Cumulative echo frequency as a function of maximum digital count within a cloud. These data have been accumulated from 255 DC, and indicate what percentage of clouds, at a given digital count or higher, have associated echoes.

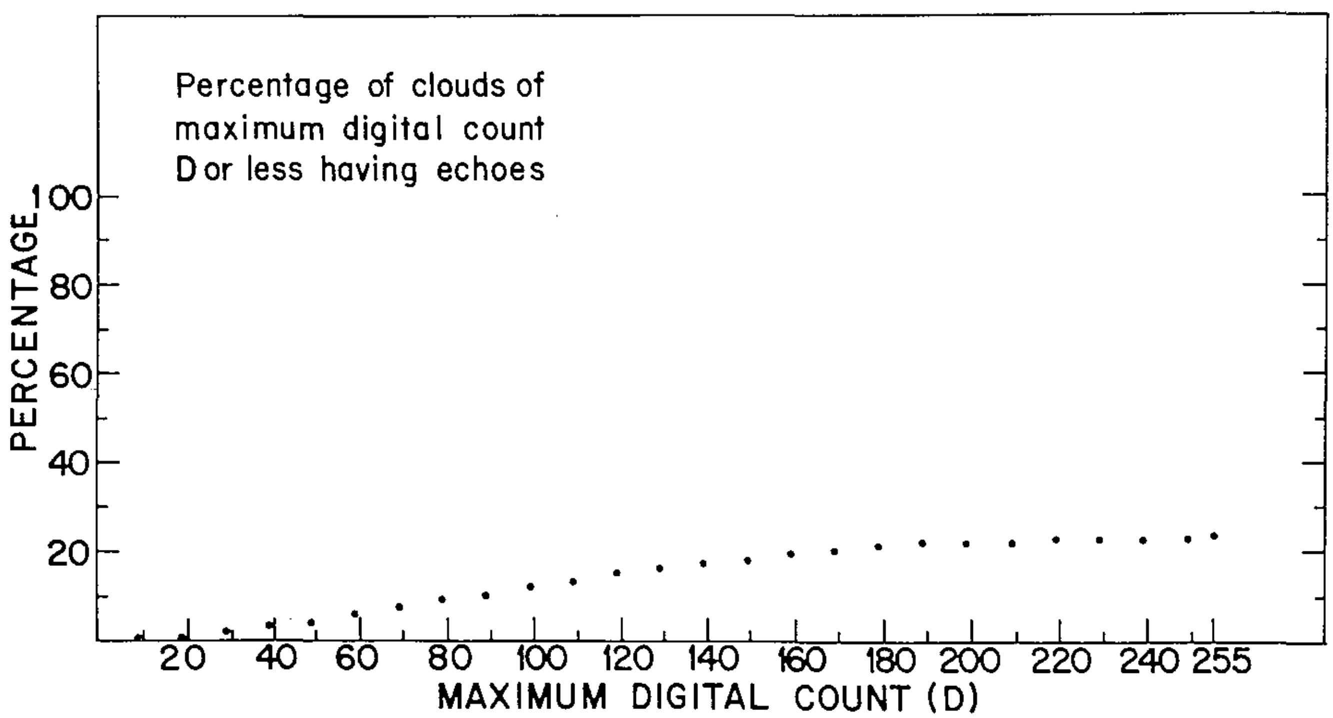

Figure 6. Cumulative echo frequency as a function of maximum digital count within a cloud. These data have been accumulated from 0 DC, and indicate what percentage of clouds, at a given digital count or lower, have associated echoes.

the overestimate of echo occurrence at the 80 DC threshold; they imply nothing about the error of rain volume estimates.

3.3 Brightness Transfer Function

All brightness measurements made with the Digicol are in terms of density units. The transfer function from digital count to density units (DU) for the Standard Height (the 33x ATS image magnification specified by the parameters in table 1), has been shown in figure 3. The equation of best fit gives density a logarithmic dependence on digital count. This dependence results because in the density mode all signals are processed through a log amplifier. From figure 3 it can be seen that at the Standard Height the 80 DC threshold is equivalent to 0.86 DU.

3.4 Derivation of the Method

Cloud brightness is positively correlated with rainfall; as brightness increases, the probability of rainfall increases. Although one-half of the clouds with maximum brightnesses of 80 DC or greater have echoes, this brightness-rainfall relationship is strongly time-dependent. The correspondence between cloud brightness and rainfall at the earth's surface is better when a cloud system is young and vigorous than when it is old and decaying. Consequently, any attempt to relate cloud brightness to precipitation frequency, intensity and extent must consider changes with time. The method must also have general applicability to cloud masses of any size.

The fundamental premise of this method was that the time behavior of clouds and echoes would approximate the simple model shown in figure 7. The top row represents the cloud as seen on a series of six satellite pictures, whereas the bottom row is the corresponding echo at the same times. Both clouds and echoes grow to a maximum and then decay. Maximum cloud area, A_M, is singled out, because both cloud and echo areas will be normalized by this quantity.

In deriving an empirical relationship between satellite-measured cloud characteristics and rainfall, complete satellite and radar, histories of several cloud systems on 11 days[6] were followed. Three of the 11 days were processed entirely by SSEC, 7 by NHEML, and 1 jointly by the two groups. At SSEC digital ATS-3 and WSR-57 tapes were electronically superimposed and processed on McIDAS. At NHEML, the ATS-3 negatives were analyzed on a scanning densitometer and the echo data were processed either by hand from the radar microfilm, or with the appropriate digitized radar software (Wiggert and Ostlund, 1975).

---

[6]They are Julian days: 166 (15 June), 177 (26 June), 183 (2 July), 187 (6 July), 188 (7 July), 192 (11 July), 197 (16 July), 214 (2 Aug), 216 (4 Aug), and 222 (10 Aug); all data are from 1973. As of writing, time histories of two days of SMS-1 1 km data have been analyzed on McIDAS, but are not included in the relationship shown.

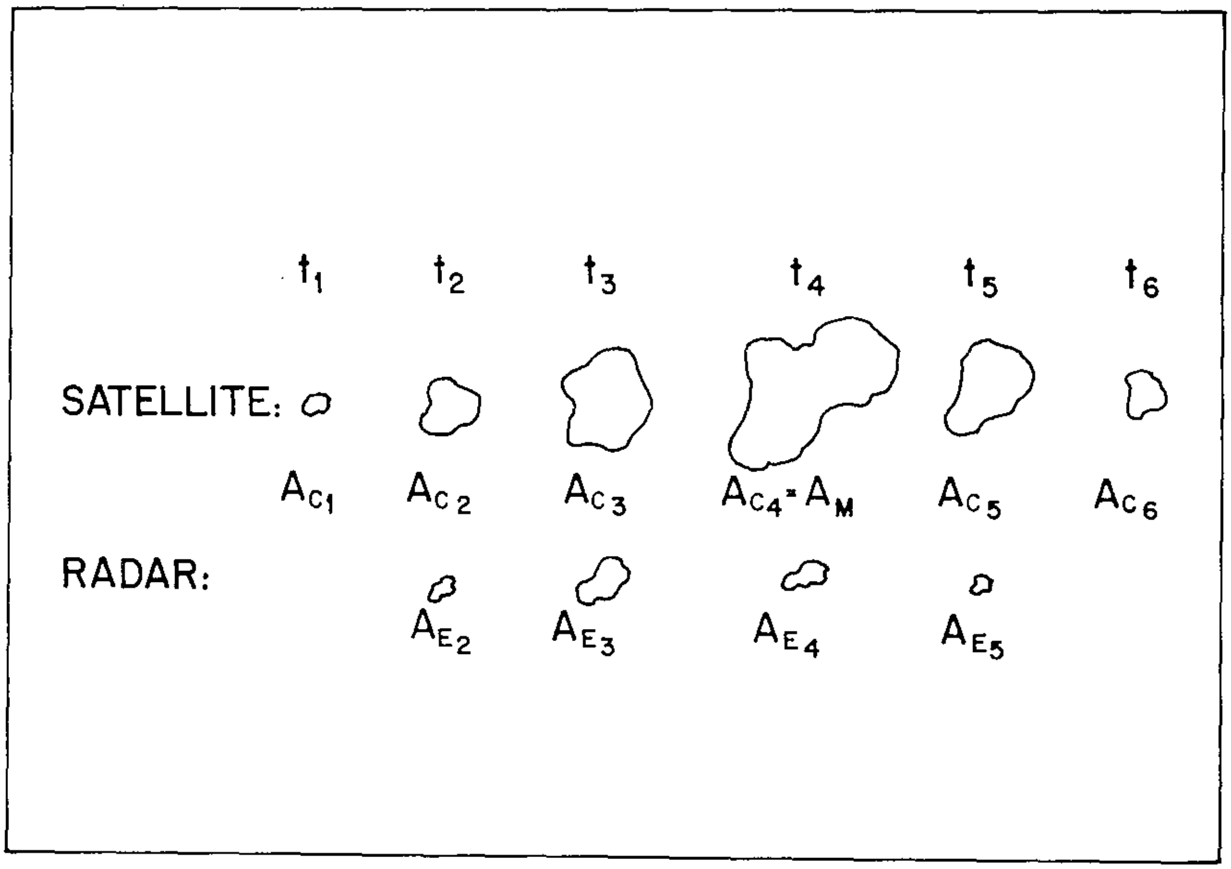

Figure 7. A schematic of simultaneous cloud and echo tracings from the satellite and radar, respectively. Note the lag between maximum echo area and maximum cloud area.

The ATS digital tapes contain the full resolution of a 0-255 scale, whereas the negatives have been compressed to a brightness resolution that is one-quarter of that on the tapes. Photographic processing effects, as well as transmission line problems, are inherent. Additionally, the noise of the densitometer is superimposed on the NHEML data set.

These time histories of cloud and echo are discussed in Martin and Sikdar (1973), Martin and Sikdar (1974), and Martin, Stout and Sikdar (1975). Included in these reports are graphs which show the time-evolution of cloud area, echo area, and radar measured rain volume. The results strongly support the previously suspected relationship between visible cloud and associated radar echo. Furthermore, the histories reinforce the observation of weather modification experiments (Staff, Experimental Meteorology Laboratory, 1974) that a variety of regimes can be found in Florida from one day to the next. Any relationships developed will therefore approximate the mean Florida situation.

The first step linking brightness to rainfall is shown in figure 8. Cloud masses with threshold brightness of 80 DC were related to those associated radar echoes having a rainfall rate of at least 1 mm/hr. After cloud areas and echo areas were measured at these respective thresholds, all measurements

Figure 8. The cloud area - echo area relationship. Both cloud (A_C) and echo (A_E) areas have been normalized to the (relative) maximum cloud area (A_M). Data have been averaged over intervals of 0.10x A_C/A_M. The curve is an eyeball fit to the mean data. Median values are also plotted.

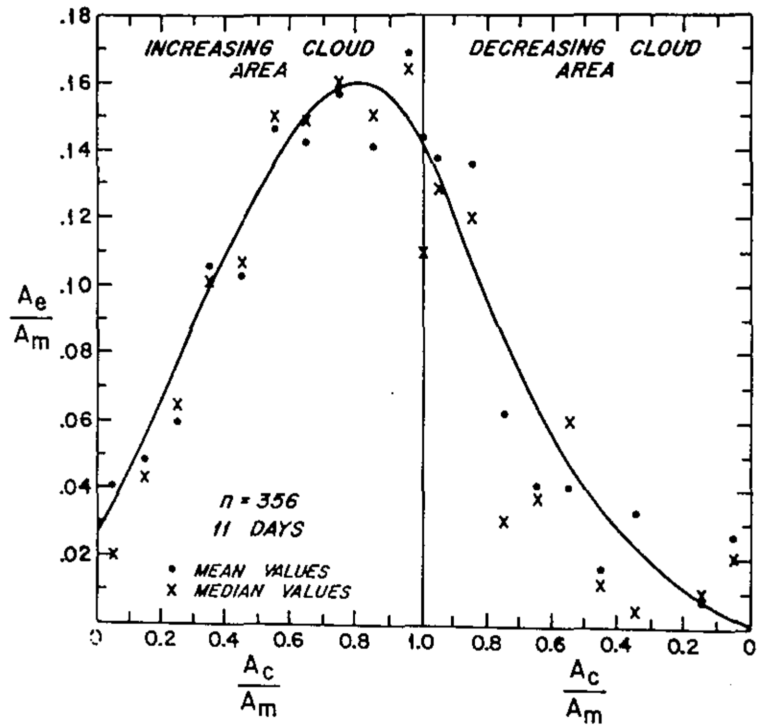

for a particular cloud were normalized to the relative[7] maximum area achieved by the cloud system so that a relationship with general applicability could be generated. Thus, the ratio A_C/A_M versus the ratio A_E/A_M is shown, where A_C is cloud area at 80 DC, A_M is the relative maximum 80 DC cloud area, and A_E is echo area associated with the cloud. The A_E/A_M values have been averaged over intervals of 0.10 A_C/A_M; mean and median values per interval are plotted. The resultant asymmetric curve is due to echo area peaking before the 80 DC cloud area reaches its maximum. Physically the radar, which observes a slice through the cloud, senses the maximum rain area of the cloud before the impulse producing the rain is obvious at the cloud top which the satellite views. The time difference between the echo and cloud maximum areas is usually 45 to 75 minutes.

In using the normalized cloud area - echo area relationship to obtain rainfall, a complete history of the subject cloud mass on the satellite photographs is required. The maximum cloud area A_M is determined, the ratio A_C/A_M is calculated for each picture, and A_E/A_M values are read from table B1. When the cloud mass is increasing to its maximum area, the left portion of the diagram is used; if it is decreasing from its maximum, the right portion is used. Knowing the value of the ratio A_E/A_M and of A_M itself, echo area A_E is obtained. Then entering A_E in the appropriate echo area - rain volume relationship for the geographic region in which the cloud occurs, rain volume is calculated. Once this procedure has been followed for all photographs, an estimate of total rainfall is obtained. A detailed rain calculation using the densitometer is presented in Appendix B.

[7]As described in Appendix B, ATS-3 cloud entities generally showed multiple relative maxima rather than a single max. With the improved resolution SMS visible data, most clouds show a single max.

The echo area - rain volume relationships for south Florida have been derived from digitized Miami WSR-57 radar observations. The relationships, which have been stratified by echo growth trend, are:

$$r_V = (1.30 \times 10^3)\ A_E \qquad \text{(increasing echo area)} \tag{1}$$

and

$$r_V = (0.66 \times 10^3)\ A_E \qquad \text{(decreasing echo area)} \tag{2}$$

where r_V is rain volume (m^3) per 5 min and A_E is echo area (km^2) defined by the 1 mm/hr rain rate. The constants in (1) and (2) include the conversion from units of km^2-mm/hr to m^3/5 minutes. To avoid discontinuities in the calculated rainfall as echo area changed from increasing to decreasing, a third relationship was also used. Referred to as the intermediate relationship, it is:

$$r_V = (0.98 \times 10^3)\ A_E \qquad \text{(intermediate echo area)} \tag{3}$$

where the variables are defined as above. Echo growth trend (increasing, decreasing or intermediate) is inferred from cloud growth, as described in Appendix B.

The asymmetry of the normalized cloud area - echo area curve is significant because it permits some compensation for the bright, but inactive, cirrus canopies that form during the dying stages of deep convection. Thus, for a particular value of A_C/A_M, the ratio A_E/A_M and, consequently, the echo area is greater for a cloud increasing to its maximum than it is for a cloud decreasing from its maximum. This reduced echo area is converted to rainfall by means of (2), which provides a smaller rain volume relative to that obtained with (1).

A second important feature of the method is its applicability to cloud masses of any size. This is accomplished by normalizing all measurements for a particular cloud system to its maximum area A_M. In principle, this procedure should allow one to estimate rainfall from individual clouds as well as large cloud clusters.

An alternate relationship directly linking cloud area to rain volume has been derived and is shown in Martin, Stout, and Sikdar (1975). This relationship is formally similar to that of figure 8 with rain volume normalized by maximum cloud area replacing the normalized echo area. The rationale for keeping echo area explicitly in the estimation scheme as used here was that the derivation at NHEML was facilitated by doing so. Moreover, it was planned to further stratify the echo area-rain volume equations into nine relationships to fine tune the method.

Several problems had to be solved before the rain estimates using satellite imagery could be made. The first was a complication resulting from the use of the densitometer. When the cloud masses on a negative are color-contoured and then traced onto acetate, a certain color is assigned to the rain threshold of 80 digital counts. Marginal clouds, such as small growing rain areas or decaying anvil canopies, do not color solidly with this threshold

Figure 9. The "old" method of tracing the 80 DC contour. Holes in this contour are represented by slanting lines. The Florida coastline and FACE target are also shown.

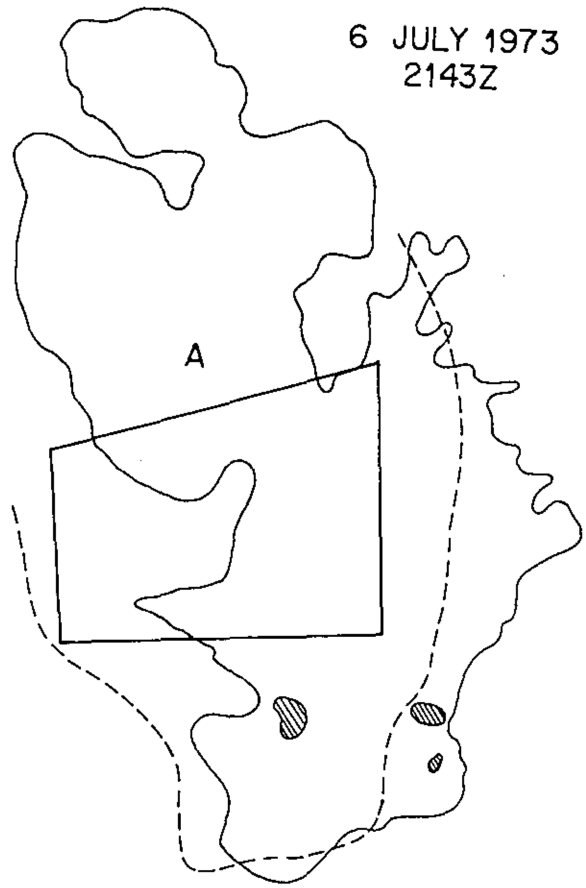

color, but contain a mix of colors, some corresponding to lesser brightnesses. This is the case over south Florida in the schematic representation of a densitometer display (figure 9), where an envelope has been drawn around the threshold color. Yet, this type of tracing includes too much nonprecipitating clouds. To put upper and lower limits on the satellite result that could be obtained by an objective measure of cloud area, it was decided to trace the areas by two methods. The first (or old) method was to include all picture elements with at least some of the desired color into the tracing of the cloud (fig. 9), to maximize the inferred rainfall. The second (or revised) method was to subjectively include only those portions of the cloud mass where at least 50 percent of the picture element was the threshold color (fig. 10). This minimizes the rainfall. It remains to be seen whether the two methods bracket the groundtruth.

A second problem has been inherent to the method from the outset. The relationship of figure 8 considers only cloud threshold brightness and does not incorporate higher level brightness information. This is not a serious problem for cloud masses of the size studied in Florida because the brightness cores generally occupy only a small fraction of the cloud. However, for cloud systems such as hurricanes, this limitation can be very serious. Incorporation of the higher brightness information is described and employed in estimates of hurricane rainfall (section 6).

Figure 10. The "revised" 80 DC contour (stippled) superimposed on the "old" 80 DC contour of figure 9.

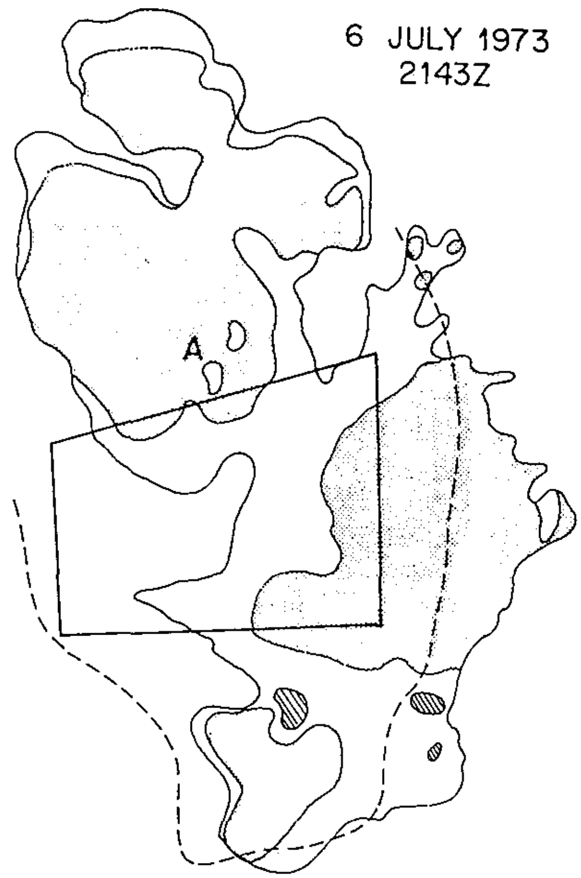

The third difficulty was the calculation of rainfall for a specific geographic area. It often happens that during its lifetime only a portion of a subject cloud traverses the given geographic area. How does one apportion the rain from these clouds? The following options were investigated: (1) consider only those portions of the subject clouds actually in the area, calculate rain volumes for each portion separately, then sum to get a total rainfall in the area; (2) determine the portions of the clouds in the geographic area, and treat as one cloud for the rain calculation; or (3) define cloud "entities," calculate the rainfall from each entity and then apportion the rainfall in the area of interest based upon the fraction of the entity actually in the area. (See fig. 11 for a schematic of these options.) The third scheme seemed the most logical, and was the scheme used in the method's derivation. This third procedure is detailed in Appendix B.

Last, because estimates were to be made over a specific geographic area within which gages were located, the problem of picture gridding had to be overcome. Conventional gridding (by means of acetate overlays) was too inaccurate. Quite often there is little land-water contrast in the early and late images, clouds obscure the coastline or other land features on many pictures in the sequence, and the grid itself is distorted or imprecise. Since echoes must indicate the presence of a cloud, some of the 80 DC cloud

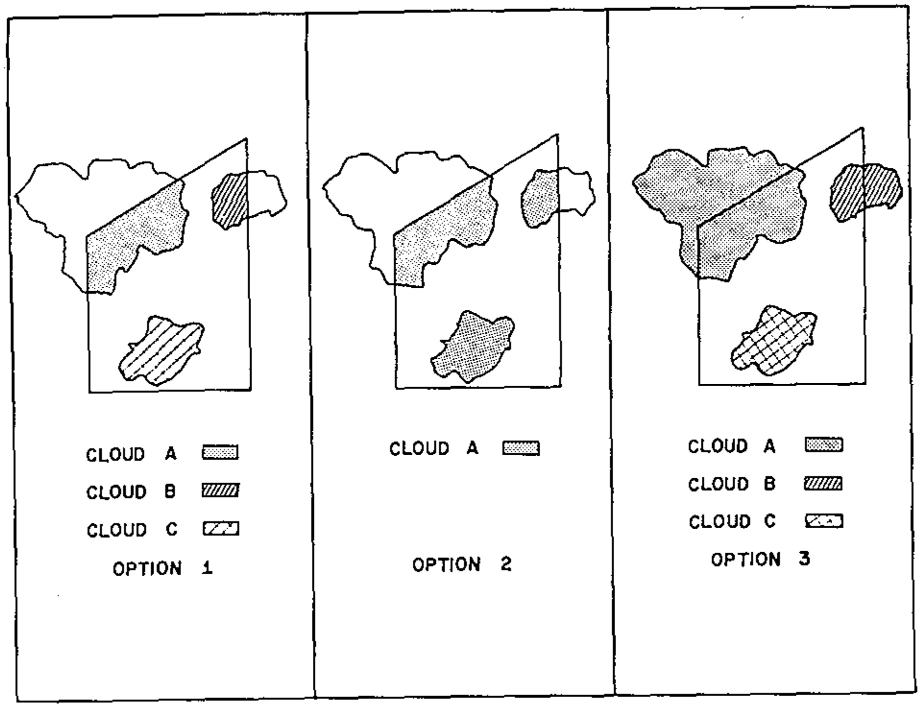

Figure 11. Three options for apportioning rain from clouds that are not totally inside an area. See text for interpretation.

tracings had to line up with the echoes when image times and magnifications were identical. This use of the radar depiction for gridding did not influence the way in which the tracings were made, nor how the rain volumes were subsequently computed. In fact, because of the tediousness of the manual area determinations, several days, or sometimes weeks, elapsed between gridding with the radar and making the calculations. Residual gridding errors arose from the following sources: parallax on the densitometer monitor, a small number of small echoes, or no echoes within 100 n mi of Miami. Conventional gridding was used on the Venezuelan and Honduran cases, sections 5 and 6.2, respectively. Inaccuracies arising from gridding should be minimized by the improved resolution of the SMS visible images.

4. VERIFICATION OVER FLORIDA

To verify the relationships of section 3.4, tests were conducted for two areas in south Florida, for an area in Venezuela, and for several hurricanes; these are described in the following sections. All tests shown here have been made with ATS-3 negatives and a scanning densitometer.

4.1 Rain Estimation in the FACE Target

In estimating rainfall in Florida from satellite imagery, only those days not used in deriving the method were eligible for analysis. During the Florida Area Cumulus Experiment (FACE) of 1973, roughly one-third of the days having simultaneous groundtruth and satellite imagery were set aside as possible verification days for the satellite rain estimates. These days were then rated based upon the quality of imagery in the Miami SFSS archive; the days with the highest rating were selected for analysis. This was done over a year before the method was actually derived.

The rain estimates in Florida were made for two areas: (1) the FACE target covering 1.3×10^4 km^2, and (2) a 333 x 333 km square (1.1×10^5 km^2) centered on the Miami WSR-57 radar. The rain groundtruth for the first area is described in Woodley et al. (1974) and was published before the satellite rain estimates were made, thereby assuring an unbiased standard. Derivation of groundtruth for the larger Florida area is discussed in section 4.2.

Rainfall was calculated from the 80 DC information only by the two methods of tracing cloud area for as long as the imagery permitted. Results from one day are shown in figure 12. The two top panels are calculations made with the old method of defining the cloud threshold, and the two bottom panels are the estimates from the revised method of defining cloud area. Hourly presentations are on the left and cumulative on the right. In each panel, the WSR-57 radar estimates of rainfall with and without gage adjustment are plotted for comparison. On all verification days, except 1 August 1973, groundtruth is defined to be the adjusted

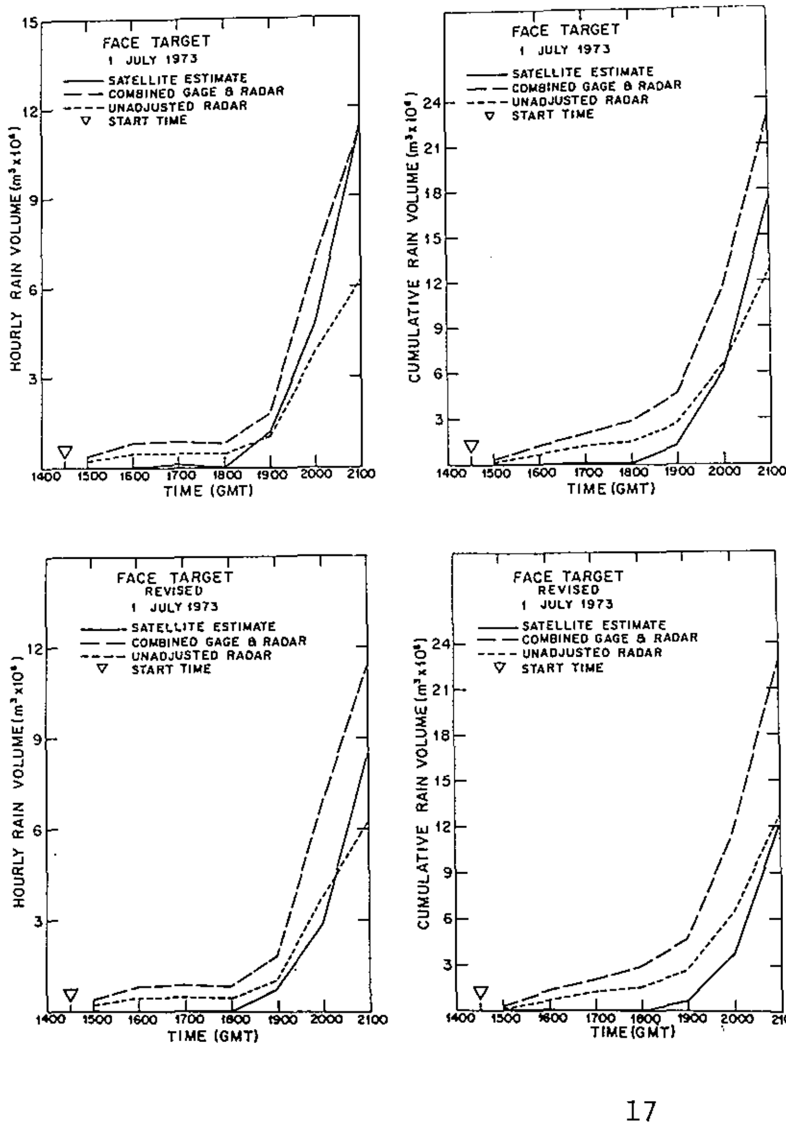

Figure 12. Hourly (left) and cumulative (right) FACE target rain results from the old (top) and revised (bottom) 80 DC areas. Satellite estimates, along with the gage adjusted and unadjusted radar volumes, are plotted. The calculation is for 1 July 73.

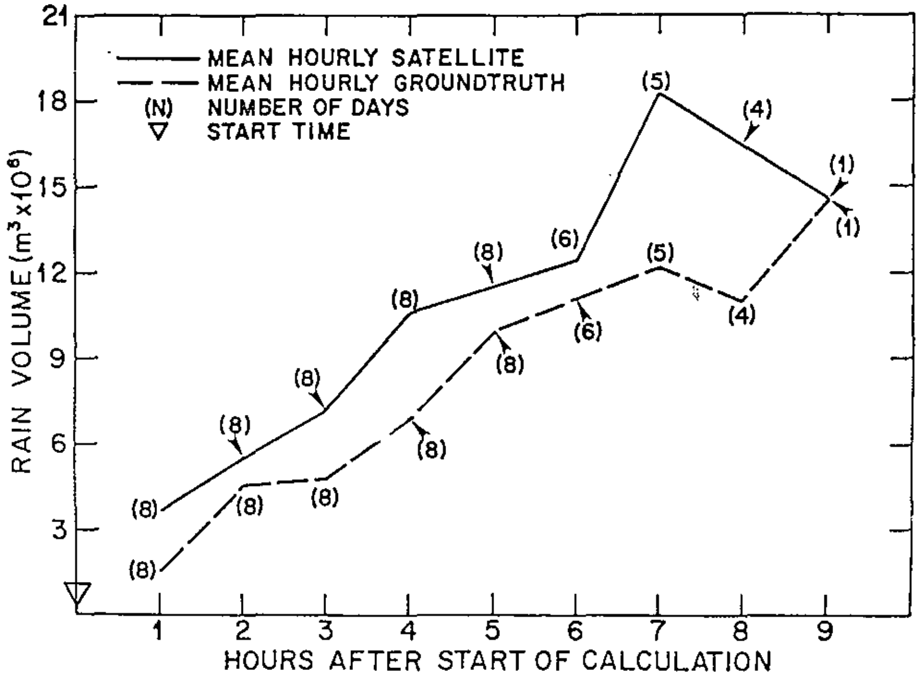

Figure 13. Mean hourly satellite target groundtruth for the old 80 DC contour. Data are composited from the calculation start time, and N, the number of days in the mean, is indicated.

radar measurements; these are probably the more accurate based on the findings of Woodley et al. (1974). The 1 August 1973 gage adjustment is less reliable because of light rainfall over the gages and the small number of gages available for adjustment. Similar presentations for the remaining verification days can be found in Appendix E.

A cursory examination of the daily results reveals that, as expected, the old and revised methods tend to overestimate and underestimate the rainfall, respectively. In either case, the estimates are usually well within a factor of 2 of the groundtruth by the end of the period of calculation. The old method has a tendency to overestimate because it gives too much weight to decaying anvil cirrus, whereas the revised method tends to underestimate, particularly on days with light rain, because it gives too little weight to the smaller showers that do not color-contour as solidly as their larger counterparts. With an objective determination of the fraction of cloud containing the threshold color, accuracy should improve even further.

Mean hourly results for the two ways of applying the method are presented in figures 13 through 15. Figure 13 (orginal method) and 14 (revised method) are mean hourly rainfall comparisons of the satellite method and the gage-adjusted radar groundtruth in the FACE target. The number near each plotted point is the number of days of data used to form the average. All results are referenced to the start time of calculation. In the mean, the old method tended to overestimate the rainfall and the revised method tended to underestimate it. In these analyses, the satellite rain results are remarkably close to the groundtruth measurements.

Figure 15 is a mean hourly absolute factor presentation that was obtained by forming the ratio of satellite to groundtruth rain estimates for each calculation hour of each day. All ratios for a particular hour were summed and the mean was obtained by dividing the number of values for each hour; ratios less than 1 were inverted. All infinities (hours when no rain fell and/or the

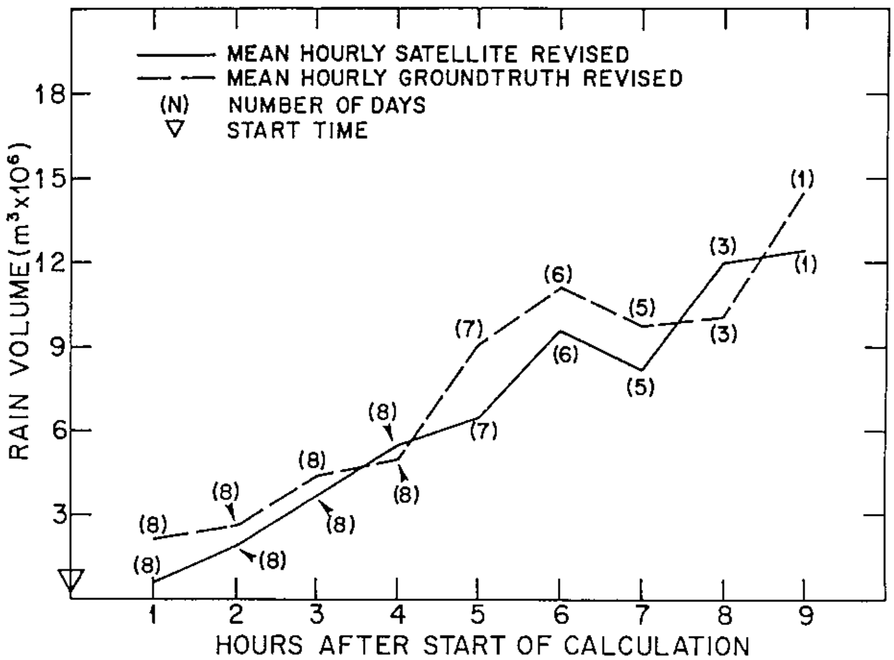

Figure 14. Mean hourly satellite target rain volumes compared to mean hourly target groundtruth for the revised 80 DC contour. Compositing and N as in figure 13.

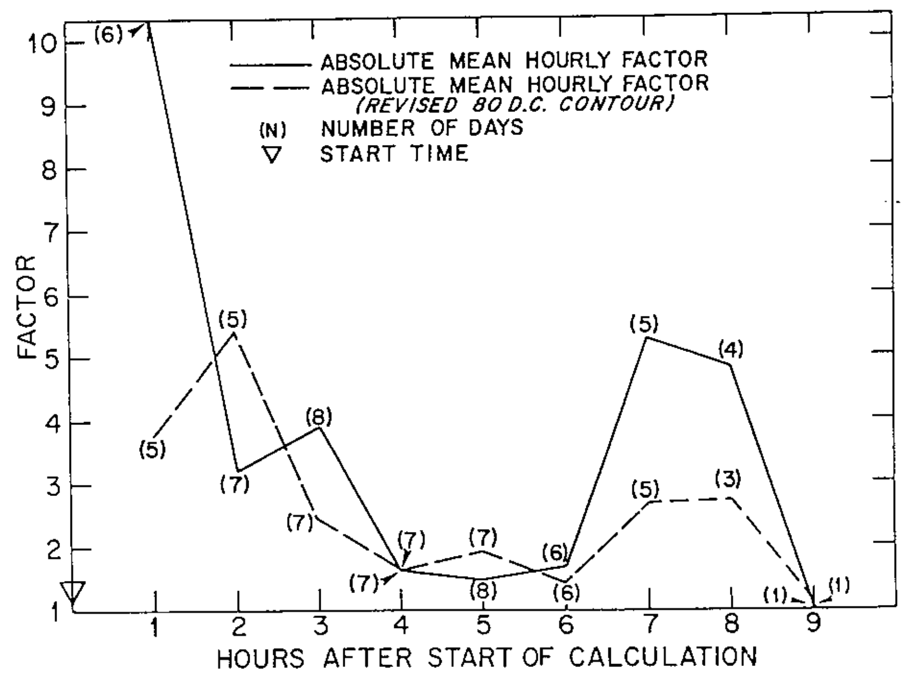

Figure 15. Absolute mean hourly factor (old method) compared to the absolute mean hourly factor (revised 80 DC contour) for the target area calculations. The factor is defined as the ratio of the satellite estimate to groundtruth, or the inverse, so that the ratio is always greater than one. Compositing and N as in figure 13.

method calculated zero m^3 of rain) were deleted to permit meaningful calculations of the averages. From this graph the results for both approaches, old and revised, suggest that one cannot expect method accuracy better than a factor of 2 of the standard for any one hourly rainfall calculation. However, volumetrically (figures 13 and 14), the satellite means for a particular hour are very close to groundtruth because the underestimates of light rains contribute minimally when combined with the estimates for the heavier rains.

The mean cumulative rainfall results for the two ways of defining the 80 DC contour are presented in figures 16 through 18. The mean cumulative rainfalls (fig. 16 and 17) agree to well within a factor of 2 regardless of approach, although the revised approach (fig. 17) performs slightly better than the original method (fig. 16).

The mean cumulative factor presentation (fig. 18) provides a measure of how well the method does within the day. The absolute mean factor is defined as before, but in this case it was determined hourly for the cumulative rainfall. Up to the fourth hour after the start of the calculation, neither approach is within a factor of 2 of the standard. After this time, the results are better than a factor of 2. This suggests that the longer the period of calculation, the better the comparison of satellite rainfall to the ground standard will be.

The results so far have dealt with hourly rainfall, but in many applications daily rainfall is of interest. Since none of the calculations was done for an entire day, we assumed that the results by the end of the period of calculation are representative of the performance of the method for the entire day. Because performance apparently improves with time, this assumption will probably underestimate method accuracy for the day. Having made this assumption, the satellite rainfalls for the period of calculation on each

Figure 16. Mean cumulative satellite target rain volumes compared to mean cumulative target groundtruth for the old 80 DC contour.

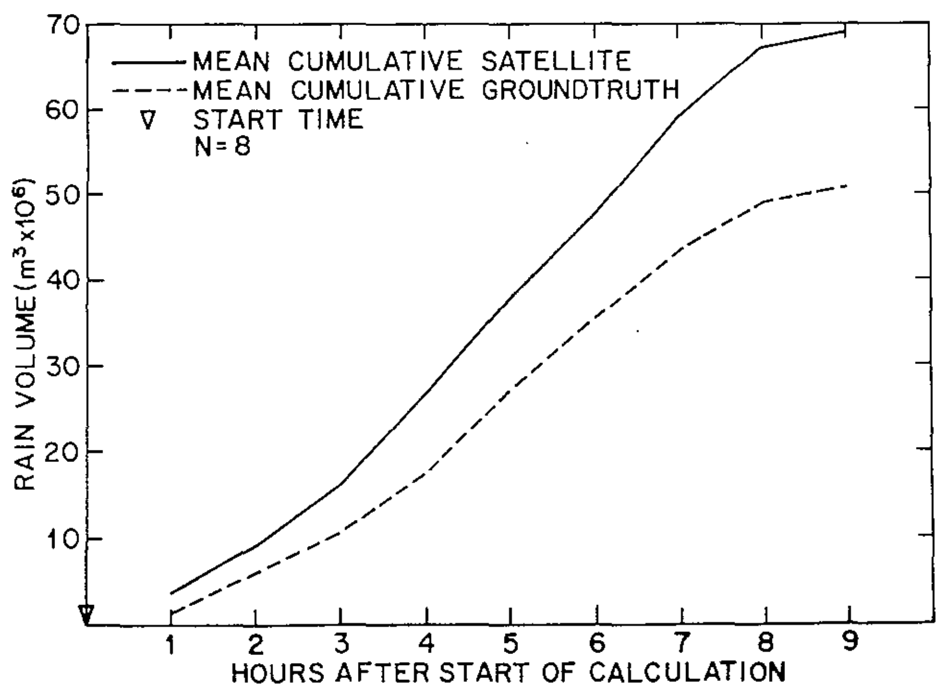

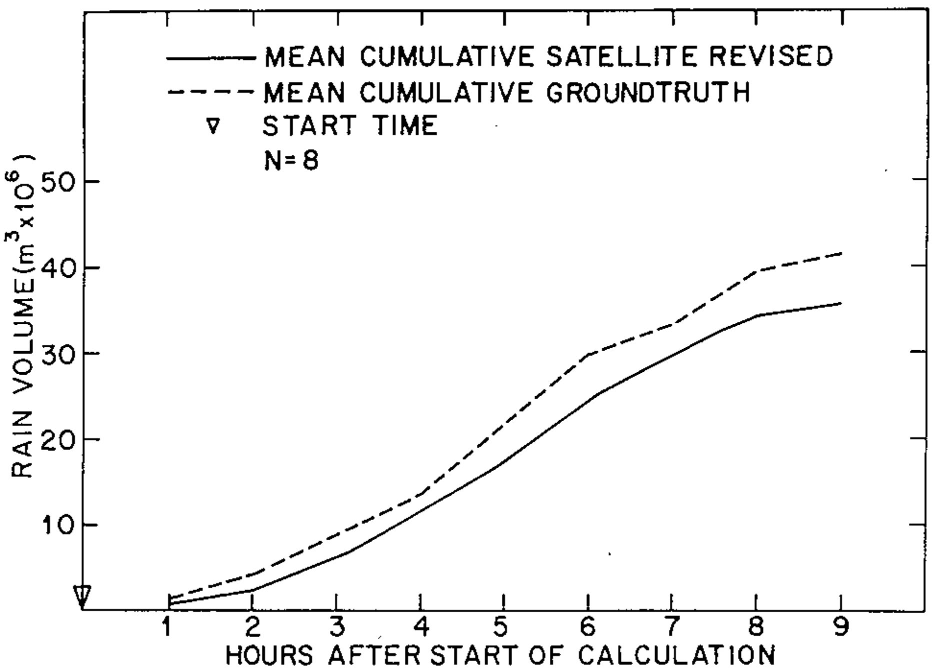

Figure 17. Mean cumulative satellite target rain volumes compared to mean cumulative target groundtruth for the revised 80 DC contour. Compositing and N as in figure 13.

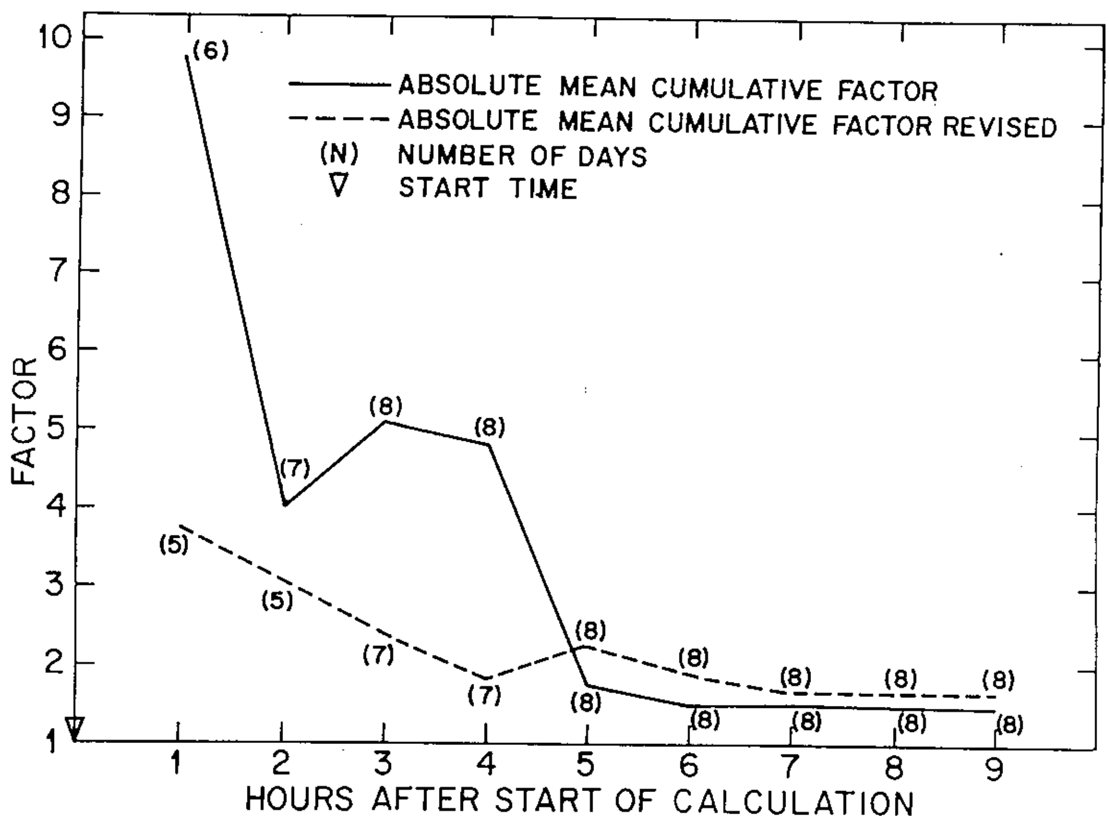

Figure 18. Absolute mean cumulative factor (old method) compared to absolute mean cumulative factor (revised 80 DC contour) for the target area calculations. The factor is defined as in figure 15. Compositing and N as in figure 13.

Table 2. Comparison of FACE target satellite rain estimates (S) with ground-truth (GT) for period of calculation

	Original method (8 days)*	Revised method (8 days)*
Daily mean ratio $\frac{\Sigma\ S/GT}{n}$	1.40	0.83 (1.21)†
Daily absolute mean ratio $\frac{\Sigma\ R}{n}$ where $R = S/GT$ or GT/S so that $R \geq 1.00$	1.47	1.65
Ratio for period of calculation $\frac{\Sigma\ S}{\Sigma\ GT}$	1.36	0.86 (1.16)†
Average duration of calculation (hours)	6.50	6.14

*Two days are not common to the two methods; 7/17/73 is in the revised method calculations only and 6/28/73, the original method only.

†The absolute factor, i.e. the inverse of the number given in the previous line.

day were compared to the gage radar standard. This type of presentation gives the same weight to a 4-hour calculation as to an 8-hour calculation. Results for both the original and revised approaches are presented in table 2.

The first row of table 2 shows the daily mean ratio, defined as the sum of the ratios of satellite to "true" rainfall divided by the number of days. The ratios are the mean accuracy to be expected for daily rain estimates. The mean ratio for the period of calculation for the old method is 1.40, compared to 0.83 (a factor of 1.21 when inverted) for the revised method of tracing clouds on the monitor.

The second row provides the daily mean absolute ratio, defined as the sum of the ratios of satellite to "true" rainfall, or the inverse depending upon which is greater than 1, divided by the number of days. These numbers represent the daily absolute error of the scheme. In this instance, the old approach is apparently better than the revised, although not significantly so. A mean absolute factor of 1.50 for the period of calculation is probably representative of the two methods.

The third row is the ratio of the summed satellite to summed groundtruth rainfall for all hours of calculation. This was computed to determine whether the performance of the method would be even better for periods of calculation greater than a day. As one might expect, our results suggest that the accuracies of the estimates will continue to improve for longer periods than the day.

In summary, both methods performed remarkably well, with the old approach generally overestimating the rainfall, and the revised approach tending to underestimate. On an hourly basis using hard copy, ATS-3 resolution images, one should not expect accuracies better than a factor of 2. Performance, both hourly and cumulative, improves as one lengthens the period of calculation. For one day, this limited sample suggests that one might expect accuracies within a factor of 1.50 of the ground standard. All errors should decrease when digital data or the higher resolution SMS data are used.

4.2 Rain Estimation in a Larger Florida Area

To determine whether accuracy is a function of space as well as time, calculations were done over an area centered on Miami and an order of magnitude larger than the FACE target (1.1×10^5 km^2 vs. 1.3×10^4 km^2). The satellite rain estimates were verified as before with radar measurements adjusted by gages. Although the accuracy of the standard is reduced because much of this lar er area is rather far removed from the adjusting gages, combined gage an radar groundtruth is still the best standard possible under the circumstanc .

Groundtruth rain volumes in this larger area were computed from the digitized radar data with an expanded version of the RSUM program[8] (Wiggert and Ostlund, 1975) called RSUM 360. (RSUM sums the rainfall in 1 n mi^2 bins over a specified time period and spatial region.) Because ground clutter is always present within 25 n mi of Miami, no rain from this circular area was included in either radar or satellite determinations.

Tracings, both old and revised, and gridding were done as previously described. Rainfall from clouds straddling the area's boundaries was apportioned as outlined in Appendix B.

Daily results for this larger area are shown in Appendix E. As before, hourly and cumulative rain volumes computed by both the old and revised methods have been plotted with the (possibly underestimated) unadjusted and adjusted radar rains. Based upon the composite ratios in table 3, it can be said that no significant changes in accuracy occurred when rainfall was calculated in the larger area. Thus, it seems that no area effect is inherent in this method, and that the conclusions reached for the target area are valid in the larger area.

5. RAIN ESTIMATES BY SATELLITE IN VENEZUELA

The opportunity for a test of the NHEML-SSEC method in another tropical location with groundtruth was provided by the Venezuelan International Meteorological and Hydrological Experiments (VIMHEX) of 1969 and 1972. VIMHEX was a cooperative effort between scientists from Colorado State University and from Venezuela, in conjunction with governmental agencies in

[8] An error has recently been suspected in RSUM 360. This error may have resulted in underestimations of groundtruth rainfall.

Venezuela. During the summers of 1969 and 1972, meteorological and hydrological measurements were made in Venezuela in the study areas shown in figure 19. The eastern stippled area is the location of the 1969 VIMHEX studies and the western circle (90 km radius), outlines the 1972 study area. Satellite rain estimates have been made over the eastern rectangle (1.1×10^4 km^2) for the 1969 days and in the circle (2.5×10^4 km^2) for the 1972 tests.

The recording raingage locations of 1969 in and around the study area are shown in figure 20. The rectangular rain estimation area was defined

Table 3. Comparison of satellite and groundtruth factors for three regions

I. Daily absolute mean factor comparisons $\frac{\Sigma R}{n}$ [a]

Satellite method	Florida Areas Target[b] (n=8)	Florida Areas Larger[c,d] (n=5)	Venezuela[e] (n=9)
Original	1.47	1.99	Nc[f]
Revised	1.65	1.40	2.33

II. Average period of calculation ratios $\frac{\Sigma S}{\Sigma GT}$ [g]

Satellite method	Florida Areas Target[b] (n=8)	Florida Areas Larger[c,d] (n=5)	Venezuela[e] (n=9)
Original	1.36	1.86	Nc[f]
Revised	0.86 (1.16)[h]	1.20	0.51 (1.98)[h]

[a] R is the ratio of the satellite and groundtruth rains, or vice versa, accumulated to the end of the calculation period. R is defined to be ≥ 1.00. "n" is the number of days in the summation.

[b] 1.3×10^4 km^2 area

[c] 1.1×10^5 km^2 area

[d] Groundtruth rainfall may be underestimated. See text.

[e] Results are from two areas in Venezuela, one 1.1×10^4 km^2, the other 2.5×10^4 km^2.

[f] Nc = No calculation made by this method.

[g] S is the daily satellite estimate; GT is the daily groundtruth; the summation is over the days of each area.

[h] Inverse of the average ratio given in the preceding line.

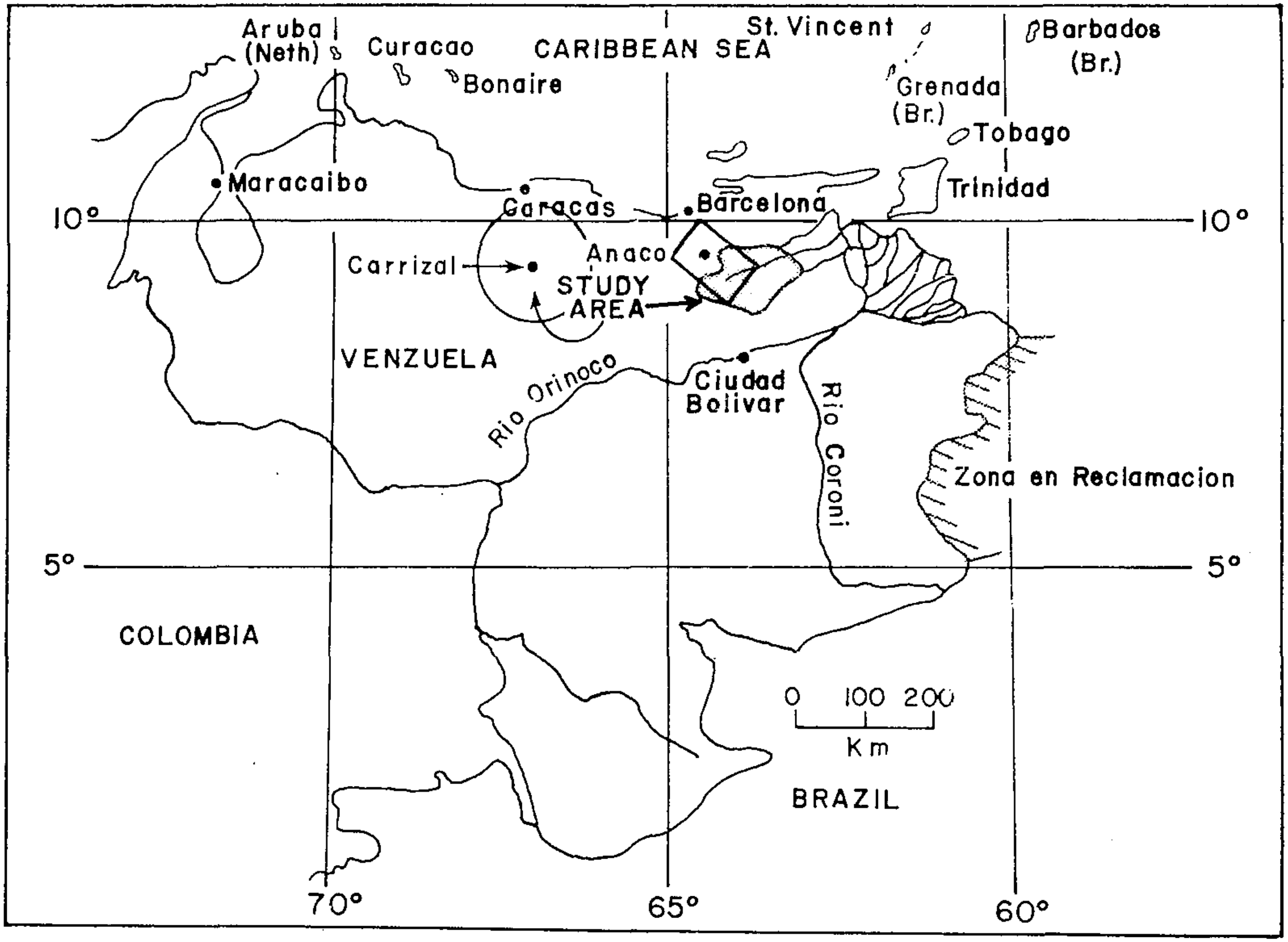

Figure 19. The 1969 and 1972 VIMHEX areas. The 1969 studies were located around Anaco. The stippled area is the VIMHEX study area and the rectangle is the satellite verification area, which was chosen to maximize area and gage density. The 1972 studies were in the circle centered on Carrizal. (The figure is after Simons et al., 1971, and Betts and Stevens, 1974.)

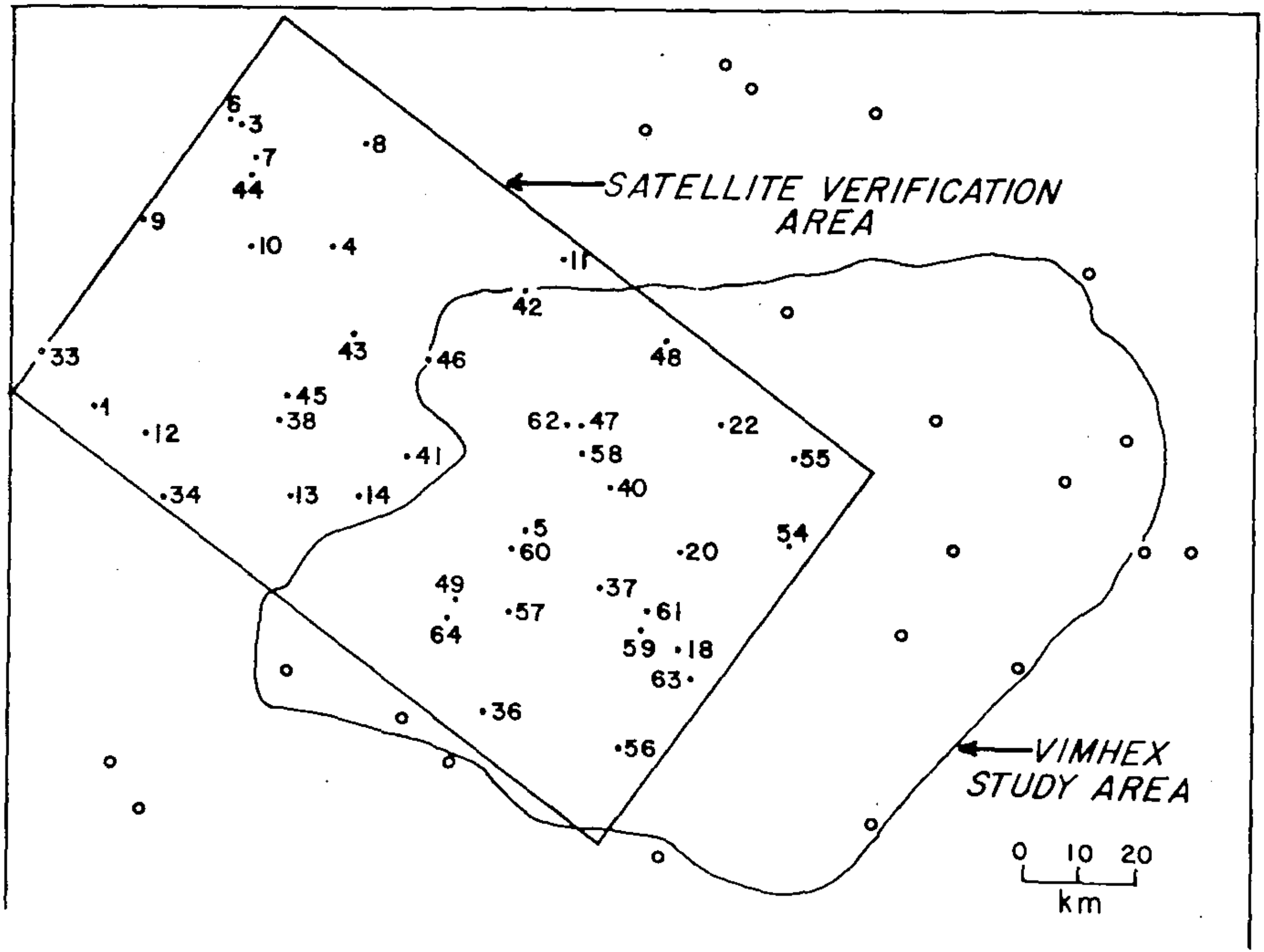

Figure 20. The 1969 VIMHEX study and satellite verification areas. The dots and open circles indicate rain gage locations. Gage identification numbers are also shown.

to maximize gage density. Area mean rainfall was calculated from the 42 numbered gages. The 82 recording and nonrecording gages of the 1972 groundtruth are shown in figure 21. As can be seen, the majority of the gages are circumscribed by the 60 km circle, whereas the estimates were made for the 90 km circle.

Groundtruth for the 1969 and 1972 verification tests was calculated from the gage data tabulated in Simons et al. (1971) and Betts and Stevens (1974), respectively. (No radar data were employed.) Area mean rainfall was determined by summing the individual daily gage amounts and dividing by the number of available gages. A sampling error was applied to these area means, in the manner described next.

In the Florida area tests, the gage-adjusted groundtruth was accepted as the standard based on the precipitation measurement studies of Woodley et al. (1974). However, these studies also indicate that gage accuracy in the areal measurement of precipitation is a function of gage density. Assuming that the temporal and spatial variability of the rainfall in Venezuela is similar to that in Florida, the Florida intensive studies can be used to provide a

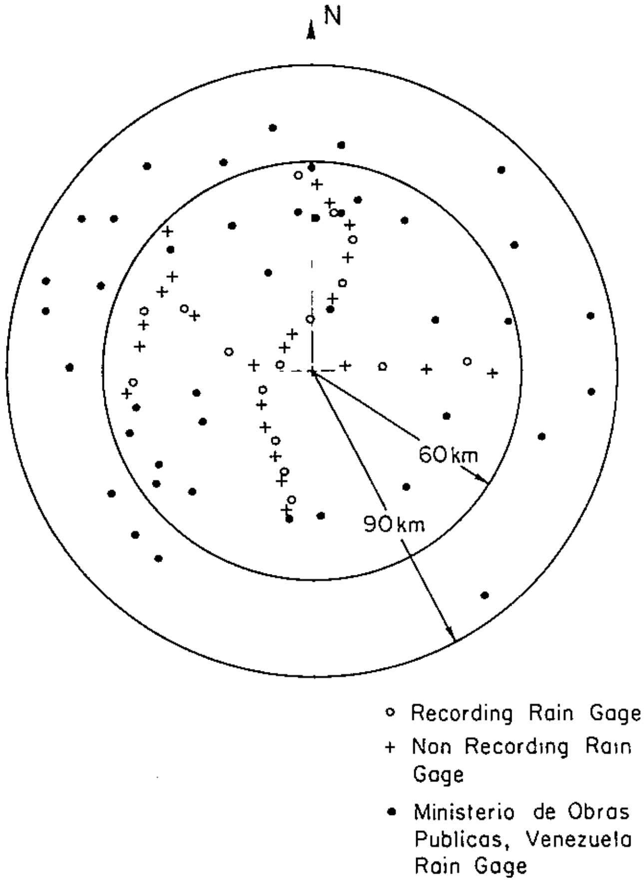

Figure 21. The 1972 satellite verification circle of 90-km radius. The city of Carrizal is located at the center and the several gage types are indicated.

first estimate of the probable error appropriate to the gage density of Venezuela. After the probable error has been determined, the comparison of Venezuelan groundtruth and satellite rain estimates can be made.

The gage density in the rectangular verification area in Venezuela is 261 km^2/gage, but the area itself is roughly comparable to (15 percent smaller than) the FACE target. The sampling error derived from the FACE target study for this 1969 area and gage density is shown in figure 22. In this presentation, the sampling error is a function of area mean rainfall and is defined as the absolute difference between the true mean rainfall (defined by one gage/3 km^2) and the area mean rainfall obtained by a lesser gage density, in this case, the 1969 VIMHEX density. Despite the fact that the 1972 verification area is 90 percent larger than the FACE target and has a gage density of 310 km^2/gage, this sampling error will also be applied to the 1972 data. Data from Woodley et al. (1974) suggest that this is a valid first order error approximation, because additional results show that for a given accuracy over the FACE target, the gage density required to achieve the same measurement accuracy over a larger area decreases. Accordingly, the 1969 and 1972 gage networks will have equivalent sampling errors in this study.

Verification days were chosen on the basis of available ATS imagery and the requirement that the bulk of the rain had ended in the study area before the last satellite picture. This proviso was necessary because the method

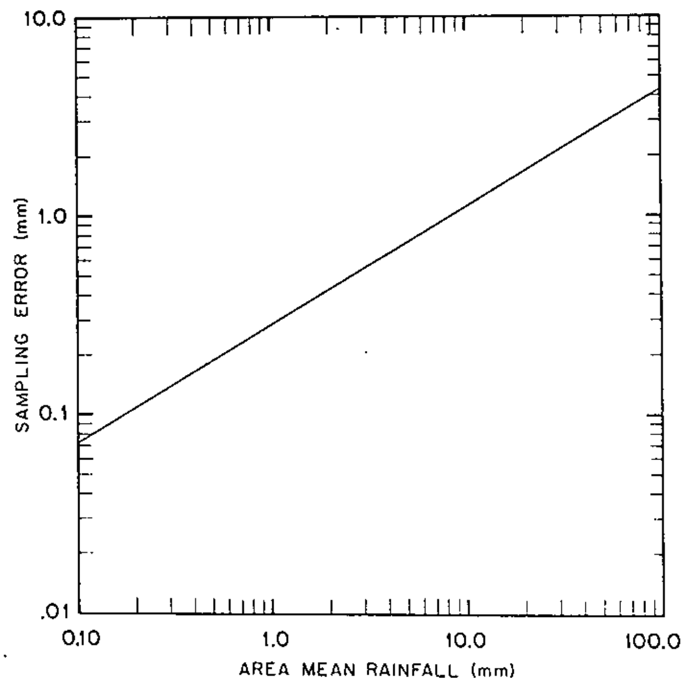

Figure 22. The sampling error relationship for the 1969 and 1972 VIMHEX satellite verification areas. The sampling error is the absolute difference between the mean error obtained for 1 gage/3 km^2 and the mean error from a lesser gage density.

requires a complete history of a rain system; when only a portion of the cloud life cycle is obtained, errors are introduced. High quality imagery was also needed. Consequently, all days on which the rain fell between 1400 and 1930 GMT (according to the VIMHEX recording gage data) were rated based on the quality and number of satellite photographs. As a result, comparison tests were made on nine days.

The rain estimates from the satellite imagery were made as described for Florida, with the exceptions that area averaged rain depths, rather than volumes, are shown and only the revised method of determining the cloud threshold was used. These satellite estimates and two groundtruth standards are presented in table 4. The first standard is the area average mean, the second is this area mean after adjustment by the most probable sampling error. The latter incorporates confidence limits on the groundtruth by adding and subtracting the sampling error obtained from figure 22.

As can be seen, the satellite rain estimates consistently fall outside the limits of groundtruth adjusted by the sampling error, and the majority of the results are underestimates. The underestimation can be attributed in part to use of the revised method of measuring cloud area, per the conclusions of section 4. However, table 3 shows that the Venezuelan mean daily and mean period errors are much greater than the Florida results. Although the specific cause of these errors has not been determined, the following items are sources of error:

(1) A mix of recording and nonrecording gage data has been used. Significant amounts of rain falling outside the period of the satellite estimation would cause groundtruth rainfall to be greater than that calculated from the images. This may be the case on 19 June 72, 11 July 72, and 11 Aug. 72.

Table 4. VIMHEX groundtruth, sampling error, and satellite estimates

Date	Groundtruth (mm)	Groundtruth ± sampling error	Satellite estimates (mm)
11 July 69	6.2	7.0 to 5.4	3.48
12 July 69	4.6	5.3 to 3.9	4.91
19 June 72	10.0	12.4 to 9.2	4.36
30 June 72	3.3	3.9 to 2.7	2.86
10 July 72	6.4	7.2 to 5.6	2.48
11 July 72	9.0	10.0 to 8.0	2.62
9 Aug. 72	8.4	9.4 to 7.4	10.25
10 Aug. 72	3.6	4.2 to 3.0	0.66
11 Aug. 72	7.4	8.3 to 6.5	2.44

(2) The inferred sampling error may be too low for the 1972 data, particularly because of the inhomogeneous distribution of the gages over the verification area. Although the overall gage density is 310 km /gage, the density over the interior circle is 180 km /gage, and that of the outer 30 km annulus is 744 km /gage. If, on a given day, most of the rain were to fall in the outer annulus, the sampling error of figure 22 would not apply. This apparently is the case in 10 August 1972.

(3) Gridding was more difficult in Venezuela than in Florida because of the prevalence of convection along the northern coast of South America.

(4) The 1969 picture sequences had gaps during the estimation period, and picture quality was poor because copy negatives were employed. The 1972 data were original negatives of good quality.

Because of the sources of error cited above, it would be premature to conclude that this estimation scheme cannot be applied to semitropical or tropical areas outside Florida. Additional tests with better controlled groundtruth and satellite data than used here would resolve the question.

6. RAIN ESTIMATES IN HURRICANES FROM SATELLITE IMAGERY

As a further test of the method, rainfall was estimated from selected hurricanes. Hurricanes Carmen and Fifi of 1974, Agnes of 1972, Edith of 1971, Celia of 1970, and Debbie in 1969 were selected for this purpose. Fifi had priority because verification of the satellite-derived rain estimates was possible using gage measurements in Honduras, where severe flooding occurred. Although no groundtruth exists for the other storms, relative comparisons of rain volumes and average depths were made.

6.1 Modification to the Method for the Calculation of Hurricane Rainfall

Before the hurricane analyses were initiated, it was obvious that brightness information above the 80 digital count contour had to be incorporated into the method. The methodology was developed from mesoscale systems in which significantly large brightness contours above 100 DC rarely occurred, and wholesale application of such a method to macroscale phenomena seemed unwarranted.

The results in figures 3 through 5 have shown that echo probability, and thus coverage, increases with cloud brightness. On the basis of these results, the echo area - rain volume relationships were modified to include the higher brightness information. For each contour above 80 DC, echo area, and thus resulting rain, was increased by a weighting factor which was composed of two parts - the brightness of the interior contour and the fraction of the system at this brightness. The former term was empirically determined from the cloud and the echo data base derived on McIDAS. The ratio of echo coverage at a higher brightness threshold to the ratio of echo coverage at 80 digital counts was formed. In this ratio, echo area cancels, for example, $(A_E/A_{90}) \ / \ (A_E/A_{80}) = A_{80}/A_{90}$. Given the data on hand, the following empirical coefficients were derived:

$$\frac{A_{80}}{A_{80}} = b_1 = 1.00 \qquad \frac{A_{80}}{A_{105}} = b_3 = 1.81$$

$$\frac{A_{80}}{A_{90}} = b_2 = 1.16 \qquad \frac{A_{80}}{A_{120}} = b_4 = 2.75$$

The second part of the weighting factor is the fraction of the storm occupied by successive brightness contours. For the empirical coefficients above the fractions are:

$$a_1 = \frac{A_{80} - A_{90}}{A_{80}} \qquad a_3 = \frac{A_{105} - A_{120}}{A_{80}}$$

$$a_2 = \frac{A_{90} - A_{105}}{A_{80}} \qquad a_4 = \frac{A_{120}}{A_{80}}$$

Thus, a hurricane with a maximum brightness exceeding 120 digital counts would employ the modified echo area (A_E) and rain volume (r_V) relationship of the form:

$$r_V = I \times 10^3 m^3 \times A_E \ (a_1 b_1 + a_2 b_2 + a_3 b_3 + a_4 b_4) \qquad (4)$$

where

$$I = \begin{cases} 1.30 \\ 0.98 \\ 0.66 \ . \end{cases}$$

The value that I assumes depends on the inferred trend of echo area, as treated in Appendix B.

For those hurricanes in which it was not intended to verify the calculated rain volumes, the analysis procedure was relatively simple. The areas covered by several brightness contours in the hurricane were calculated using the densitometer's electronic planimeter, and rain volumes were estimated using the cloud area - echo area diagram (fig. 8) with the modified echo area - rain volume relationship (4). Because we intended to verify Fifi's rain estimates with the Honduran gage data, it was necessary to determine the fraction of the storm's rain that fell in that country. This type of calculation required that the echo area - rain volume relationship be further modified, by brightness-weighting, to:

$$r_V = I \times 10^3 m^3/Km^2 \times A_E \, (a_1 b_1 f_1 + a_2 b_2 f_2 + a_3 b_3 f_3 + a_4 b_4 f_4) \quad (5)$$

where r_V, I, a_i, and b_i are as in (4), and

$$f_1 = \frac{A_{80\ \text{Honduras}} - A_{90\ \text{Honduras}}}{A_{80\ \text{Fifi}} - A_{90\ \text{Fifi}}} \qquad f_3 = \frac{A_{105\ \text{Honduras}} - A_{120\ \text{Honduras}}}{A_{105\ \text{Fifi}} - A_{120\ \text{Fifi}}}$$

$$f_2 = \frac{A_{90\ \text{Honduras}} - A_{105\ \text{Honduras}}}{A_{90\ \text{Fifi}} - A_{105\ \text{Fifi}}} \qquad f_4 = \frac{A_{120\ \text{Hondruas}}}{A_{120\ \text{Fifi}}}$$

where $A_{80\ \text{Honduras}}$ is the area of the hurricane's 80 DC contour which is located over Honduras, $A_{80\ \text{Fifi}}$ is the total area of the hurricane's 80 DC contour, and similarly for the remaining variables.

In performing the satellite analyses, the higher brightness contours employed were not necessarily 90, 105, or 120 DC. The actual levels (80 DC and generally one higher brightness level) were those resulting when the densitometer's standard test ramp setup (section A3.7) was used; these levels were more convenient for any hand processing that had to be done than a tighter gradient would have been. Because the b_i coefficients were calculated with data derived in the determination of the cloud threshold brightness, only those selected levels listed could be calculated. When one uses brightness information that does not correspond to the calculated coefficients, the coefficients appropriate to the higher density levels used[9] can be either interpolated or extrapolated as required from figure 23. In those instances the a_i and f_i change accordingly with the rain volume equation taking the form:

$$r_V = I \times 10^3 m^3 \times A_E \times \sum_i a_i b_i f_i \quad (6)$$

where "i" is defined by the higher brightness digital count values actually used. Appendix B gives an example of the use of (6).

[9] Section D3 describes the method for determining the digital count value of higher brightness contours.

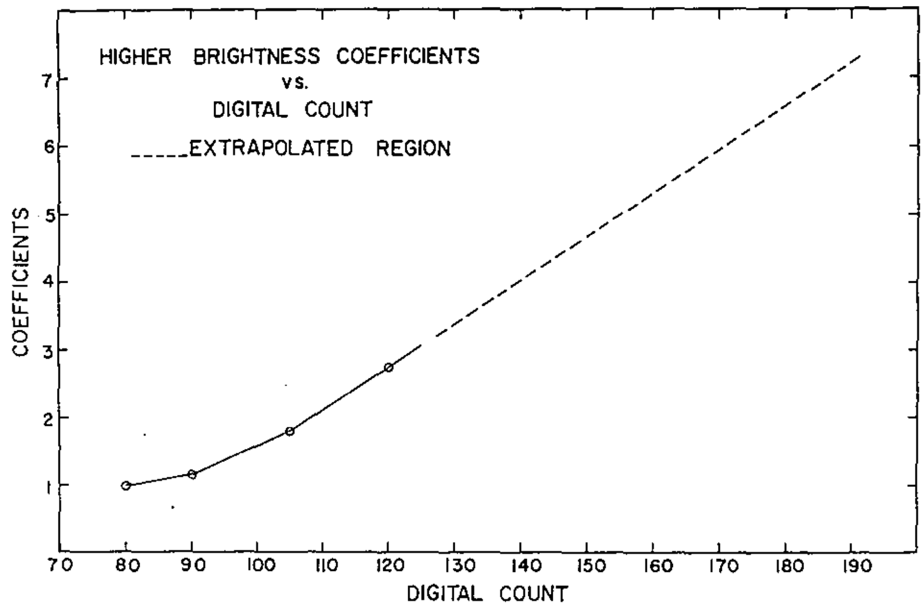

Figure 23. Coefficients for higher brightness contours to be used with the modified rain volume equations, (4), (5) or (6).

6.2 Satellite Estimation and Gage Verification of Fifi Rainfall over Honduras

The isohyetal analysis for Honduras (16 to 20 September 1974, inclusive) during the passage of Fifi is presented in figure 24. This analysis is based upon gage data provided by the Honduran National Meteorological Service. There is a clear relationship between topography and rainfall with a maximum of 592 mm (24 in.) on the north slope of the mountains along the coast. Overall, the heaviest rain fell as the storm approached from the east. In the region of southwest Honduras, the heaviest rain fell when the storm moved inland over Belize bringing a moist, southwest flow from the Pacific.

Rainfall was calculated from the satellite daily from 0700 Local Time to 0700 Local Time the next day to coincide with the time the raingages were read. Rain was estimated for the night hours by linear interpolation of the hurricane's areas from the last picture of one day to the first image on the next. When the method is adapted to the infrared imagery, calculation of hurricane rainfall thorugh the night hours from noninterpolated data will be possible.

Only ATS-3 imagery was used in the calculation because the SMS-1 satellite had a poor viewing angle for Fifi. The tracings of the hurricane were made by the revised method and the computations proceeded with the modifications described by (6). A representative tracing of Fifi along the northeast Honduran coast from the densitometer monitor is shown in figure 25. The asymmetry of this storm is apparently due to an enhancement of convection along the east-west coastal mountain range. Even the higher brightness contour (110 DC) appears to be elongated along the coastal mountain range. This is the first evidence that the method may be able to detect orographic effects. We obtained gage-derived area mean rainfall for Honduras during Fifi by summing the 100 to 106 gage readings per day and dividing by the

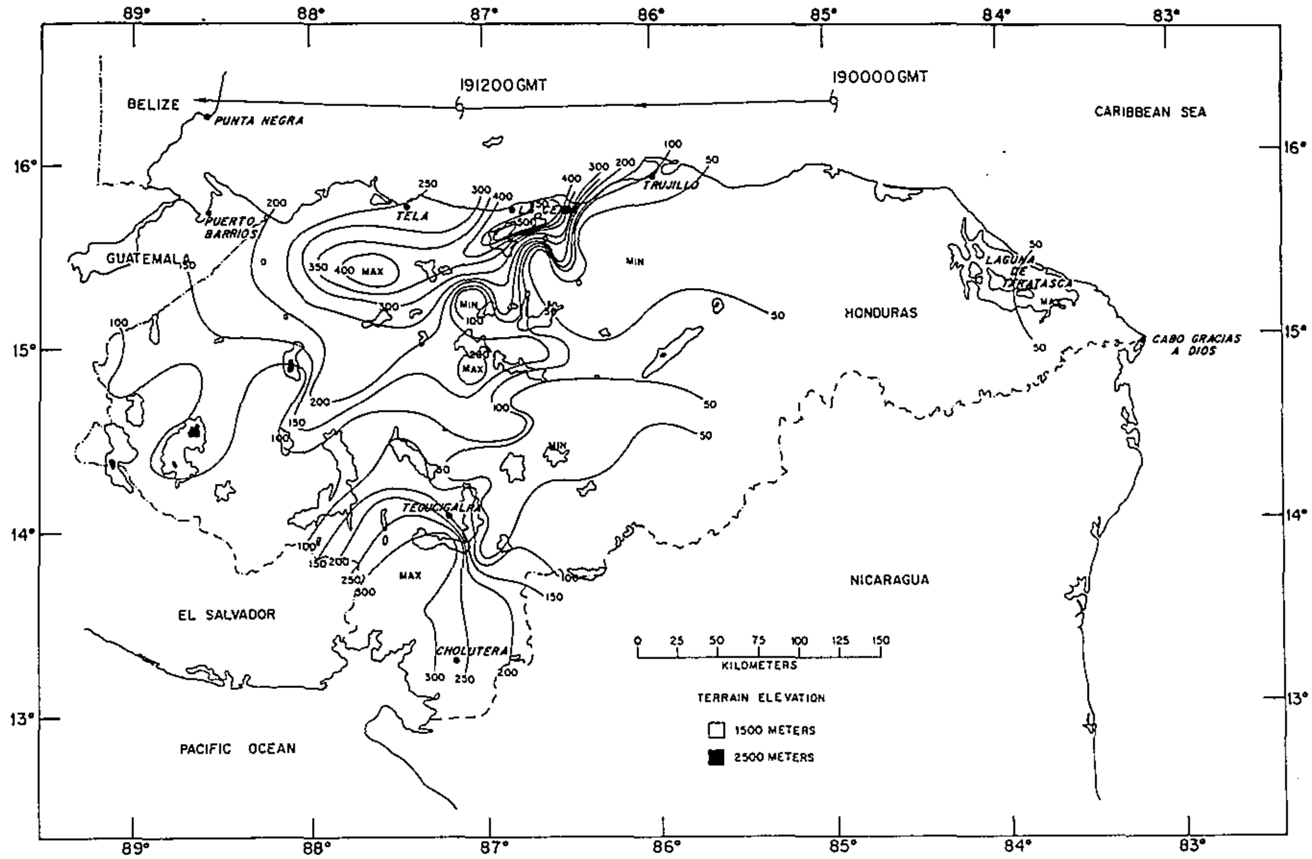

Figure 24. Isohyetal analysis (mm) of rains produced by hurricane Fifi over Honduras, 16-20 September 1974.

appropriate number of gages. The problems of gage accuracy in hurricane conditions and of the uncertainty in the area mean from a relatively sparse (100 to 106 gages in 1.1 x $10^5 km^2$) gage network are inherent in this ground-truth.

The daily gage and satellite rain estimates from Honduras are presented in table 5. The agreement between the satellite and gage estimates for the 5 days is excellent, the ratio of satellite to gage-derived rainfall at the end of this period being 1.13. Although the sample is small such excellent agreement is a compelling argument for the powers of this method in making relative comparisons of rainfall among hurricanes. If these results should be confirmed with additional tests, the satellite rain estimation method will be valuable for absolute calculations as well.

Figure 25. A schematic of two of the brightest contours over Honduras from the 17 September 1974 ATS-3 image. The outer contour is the 80 DC level, the inner, 110 DC. Note the brightness asymmetry over the mountains of northern Honduras.

Table 5. Satellite rain estimates in hurricane "Fifi" in Honduras, September 1974

Date*	Sept. 16	Sept. 17	Sept. 18	Sept. 19	Sept. 20	Sept. 16-20
Gage - derived area mean (mm)**	7.87	29.05	64.90	33.66	9.29	144.77
Satellite Estimates†	13.50	44.73	63.60	27.20	14.50	163.53
Satellite / Gages	1.72	1.54	0.98	0.81	1.56	1.13

*0700 Local Time on listed day to 0700 Local Time the next day
**Obtained by summing gages values and dividing by number of gages
†Rain Estimates for night hours obtained by interpolation

6.3 Rain Estimates in Selected Hurricanes

Rain estimates for five additional hurricanes were made with the modified satellite method of section 6.1. Even though it was not possible to verify these estimates, this exercise did allow relative comparisons among storms. Tabulations of daily hurricane rain volumes and area-averaged depths from these five storms and from Fifi are presented in table 6. We computed the area-averaged depths by dividing the daily rain volume by the mean area of the hurricane 80 DC contour. The calculations for each storm are referenced to the day on which it reached its minimum mean sea level pressure. Hurricane rain volumes and area average depths are plotted as a function of mean daily sea level pressure in figures 26 and 27, respectively.

Table 6. Daily hurricane rain estimates using satellite imagery

Name of Storm		Debbie (1969)	Celia (1970)	Edith (1971)	Agnes (1972)	Carmen (1974)	Fifi (1974)
Day relative to minimum sea-level pressure							
-3	$\overline{P}$(mb)				1000		1002
	Rain vol. ($m^3 \times 10^{11}$)				1.03		1.00
	Avg. depth (mm)				143		134
-2	$\overline{P}$(mb)	974	975	1001	995	998	984
	Rain vol. ($m^3 \times 10^{11}$)	0.29	0.75	0.32	0.91	0.40	1.17
	Avg. depth (mm)	59	65	122	131	112	145
-1	$\overline{P}$(mb)	964	980	989	985	983	974
	Rain vol. ($m^3 \times 10^{11}$)	0.30	0.14	0.39	1.00	0.59	1.43
	Avg. depth (mm)	80	33	99	135	164	108
0	$\overline{P}$(mb)	956	969	962	982	949	974
	Rain vol. ($m^3 \times 10^{11}$)	0.19	0.07	0.144	0.95	0.53	1.41
	Avg. depth (mm)	76	31	35	101	113	101
+1	$\overline{P}$(mb)	961	1000	-		965	996
	Rain vol. ($m^3 \times 10^{11}$)	0.17	0.04	0.09		0.28	0.90
	Avg. depth (mm)	66	28	25		75	57

Examination of these plots suggests that there is no relationship between storm intensity and either storm volumetric rain output or storm rain intensity. This finding is not particularly surprising (see Dunn & Miller (1960)) because tropical meteorologists have long suspected that it is the location of the latent releases in a hurricane and not its actual magnitude that determines storm intensity (Malkus and Riehl (1960)). Our study as well as the work with radar observations of hurricanes Carmen and Fifi Appendix F), lends credence to this finding.

A major concern in hurricane warning is the damage potential from storm rainfall. To demonstrate the use of our method to assess the flood potential of approaching hurricanes, we calculated the average total rain potential for the six hurricanes of study. We define the mean total rain potential for

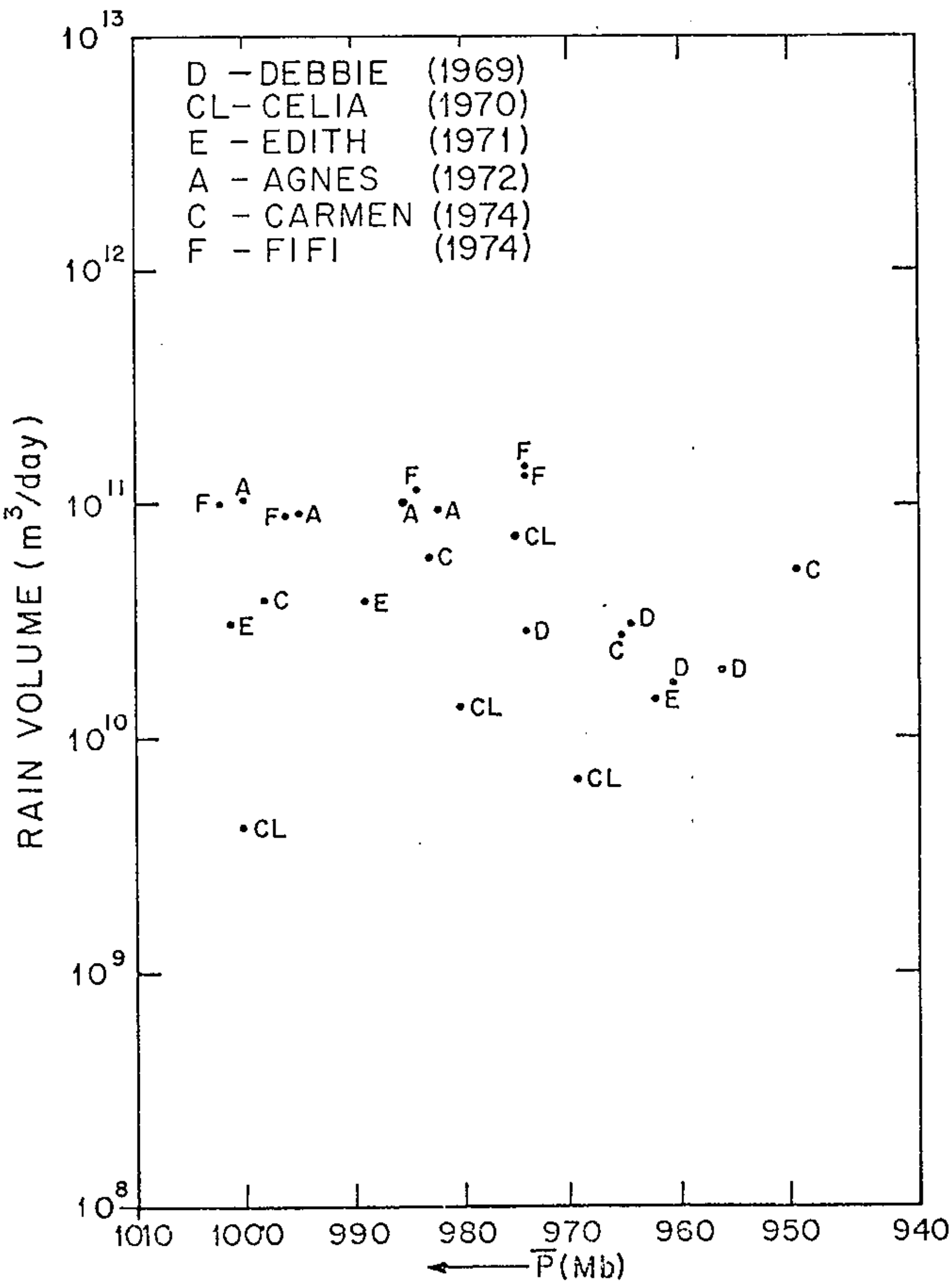

Figure 26. Daily hurricane rain volume (m³/day) as a function of mean daily sea level pressure (mb) for selected storms. Daily rain volumes have been calculated from ATS-3 images.

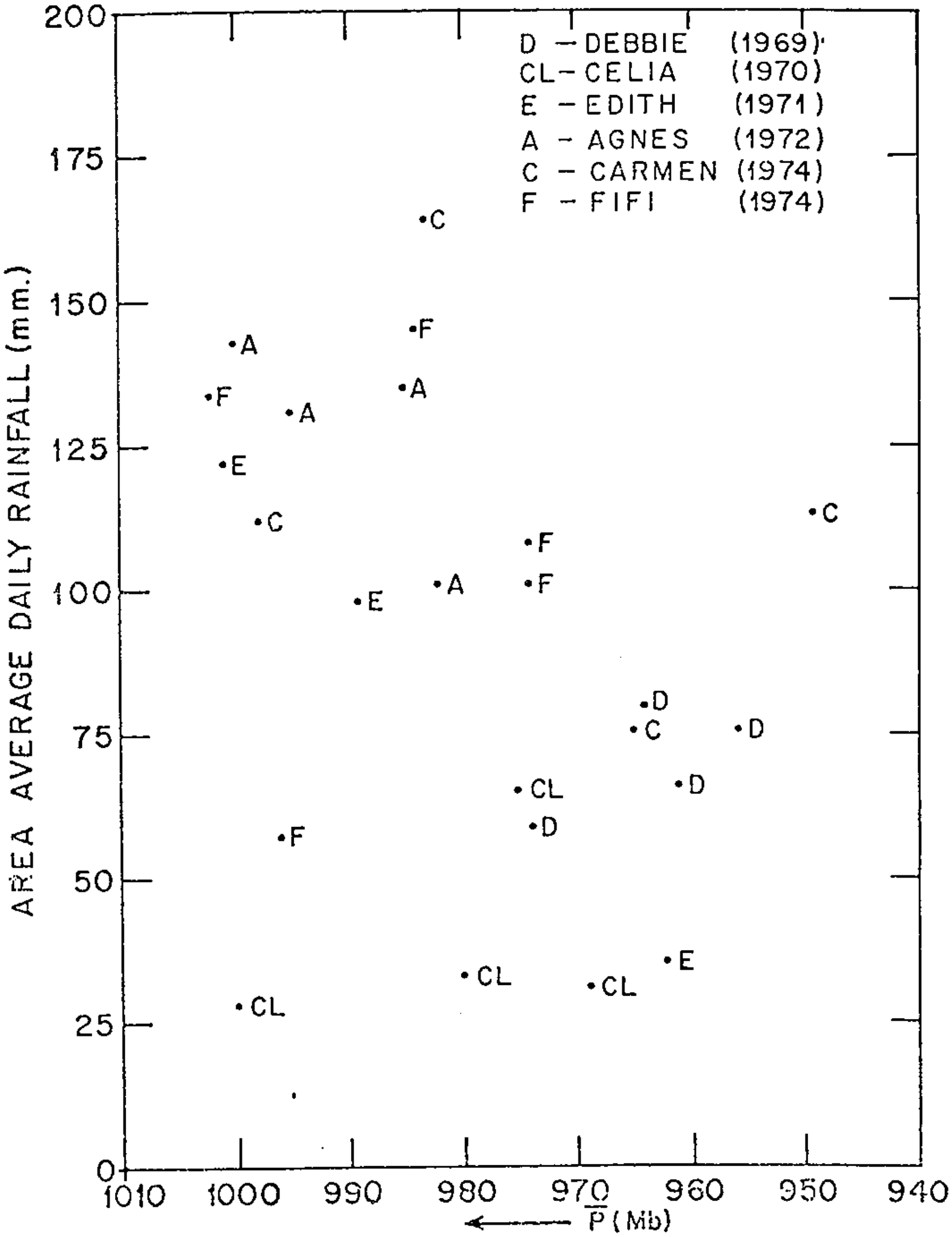

Figure 27. Area average daily hurricane rainfall (mm) as a function of daily sea level pressure (mb) for selected storms. Rain depths have been calculated from satellite derived rain volumes and satellite derived storm areas, measured at the 80 DC contour.

a point directly in the path of the storm as:

$$\text{mean total rain potential} = \frac{\overline{D}\ \overline{d}}{\overline{V}} \qquad (7)$$

where $\overline{D}$ is the daily area average storm rainfall (mm/hr), $\overline{d}$ is the mean cross section (km) of the storm in the direction of motion and $\overline{V}$ is the mean storm speed (km/day) over the period of calculation. One would expect the hurricane

Table 7. Mean hurricane rain estimates and derived flood potential

Name of storm	# Days	Mean daily rainfall: $R_v (m^3 x 10^{11})$	Rank	$\overline{D}$(mm)	Rank	Average total rain potential (mm)	Rank
Debbie (1969)	4	0.24	5	70	4	73	4
Celia (1970)	4	0.25	4	39	5	34	6
Edith (1971)	4	0.23	6	70	4	57	5
Agnes (1972)	4	0.97	2	128	1	393	1
Carmen (1974)	4	0.45	3	116	2	124	3
Fifi (1974)	5	1.18	1	109	3	232	2

$$\text{Total Rain Potential} = \frac{\overline{D}\,\overline{d}}{\overline{v}}$$

where $\overline{D}$ (mm/day) = Mean daily area average storm rainfall
$\overline{d}$ (km) = Mean cross section of storms in direction of motion
$\overline{v}$ (km/day) = Mean storm speed during period of calculation

rain potential to be directly proportional to storm size and rain intensity, and inversely proportional to its speed. Our computations are averages for the period of calculation. Similar calculations can be made for any time frame, although it is advised that periods of less than 3 hours not be used. The composite results in figures 16 through 18 show that the calculations become stable after about 3 to 6 hours.

Rain potential results are presented in table 7. Our calculations suggest that Agnes had the greatest rain potential of the five storms, with Fifi second and Carmen a poor third. Hurricanes Debbie, Edith and Celia must be classified as dry storms. Note that it was Agnes and Fifi that produced devastating floods during the last decade. Fifi resulted in the greater loss of life because of flash flooding in the mountainous terrain of Honduras. The good agreement between prediction (albeit after the fact) and result lends additional support to the use of our method to estimate rain in Atlantic hurricanes.

7. ACKNOWLEDGMENTS

This project has been completed through the continuing efforts of the many individuals and groups listed below.

Thanks are due to the NOAA GATE office, Dr. James Rasmussen and Mr. William Murray for continued support and encouragement.

The majority of the satellite imagery used was acquired by the Miami NESS facility. Don Gaby of the National Environmental Satellite Service, Vance Seiger of GE/MATSCO, and their respective staffs were most cooperative. The balance of the imagery was provided, through William Poust, by the National Climatic Center in Asheville, North Carolina and the Environmental Data Service, Washington, D.C. The fine quality of all the images is appreciated.

Thanks for significant contributions to the derivation of the method in all its stages, especially that of verification, are given to: Jaime Aguet, Joyce Berkeley, Robert Brooks, Pamela Grube, William Riebsame, George Sambataro, Fred Toepfer and Bill Walker.

We are indebted to the following persons for the rain verification data: Alan K. Betts and Pauline J. Martin of Colorado State University (VIMHEX), Ann S. McKinstry (Belize), Ramon Humberto Cruz Salgado of the Honduran National Meteorological Service and John C. Straiton of NOAA's Overseas Operations Division (Honduras), and Victor Wiggert, Stellan Ostlund, and John Stewart (the two Florida areas).

We are grateful to Cliff Dillon and the staff at the Data Analysis Facility of Kennedy Space Center's Earth Resources Office for use of their Digicol.

Maintenance of the densitometer was achieved by the electronic technicians of the National Weather Service, by Sam Calvert of the Research Facilities Center (RFC) and especially by James DuGranrut of the RFC.

8. REFERENCES

Allison, L.J., E.B. Rodgers, T.T. Wilheit, and R.W. Fett (1974): Tropical cyclone rainfall as measured by the Nimbus 5 Electrically Scanning Microwave Radiometer. Bull. Amer. Meteor. Soc., 55, 1074-1089.

Betts, A.K. and M.A. Stevens (1974): Rainfall and radar echo statistics, Venezuelan International Meteorological and Hydrological Experiment, 1972. Res. Rept., Dept. Atmos. Sci., Colorado State University, Ft. Collins, Colorado, 157 pp.

Chatters, G.C. and V.E. Suomi (1975): The applications of McIDAS. IEEE Transactions on Geoscience and Electronics, GE-13, 137-146.

Dunn, G. and B.I. Miller (1960): Atlantic Hurricanes. Louisiana State University Press, p. 110.

Griffith, C.G. and W.L. Woodley (1973): On the variation with height of the top brightness of precipitating convective clouds. J. Appl. Meteor., 12, 1986-1089.

Malkus, J.S. and H. Riehl (1960): On the dynamics and energy transformations in steady-state hurricanes. Tellus, 12, 1-20.

Malkus, J.S., C. Ronne and M. Chaffee (1961): Cloud patterns in Hurricane Daisy, 1958. Tellus, 13, 8-30.

Martin, D.W. and W.D. Scherer (1973): Review of satellite rainfall estimation methods. Bull. Amer. Meteor. Soc., 54, 661-674.

Martin, D.W. and D.N. Sikdar (1973): Calibration of ATS-3 images for quantitative precipitation estimation. Report to NOAA, Contract 03-3-022-18, Space Science and Engineering Center, Madison, Wisconsin, 12 pp.

Martin, D.W. and D.N. Sikdar (1974): Rainfall estimation from satellite images. Report to NOAA, Contract 03-4-022-22, Space Science and Engineering Center, Madison, Wisconsin, 8 pp.

Martin, D.W., J. Stout, and D.N. Sikdar (1975): GATE area rainfall estimation from satellite images. Report to NOAA, Grant 04-5-158-47, Space Science and Engineering Center, Madison, Wisconsin, 29 pp.

Martin, D.W. and V.E. Suomi (1971): A satellite study of cloud clusters over the tropical North Altantic Ocean. Final Rept. of Tropical Cloud Organization Studies, Task Order No. 3 to STAG, Contract E-127-69-(N), Space Science & Engineering Center, Madison, Wisconsin, 80 pp.

Meteorological Data Catalog for the Applications Technology Satellites, Vol. II, NASA, Goddard Space Flight Center, Greenbelt, Maryland, 353 pp.

Mosher, F.R. (1973): Cloud brightness contrast as viewed by a satellite, measurements from satellite systems. Annual Scientific Report, NAS 5-21798.

Reynolds, D. and T.H. Vonder Haar (1973): A comparison of radar-determined cloud height and reflected solar radiance measured from the geosynchronous satellite ATS-3. J. Appl. Meteor., 12, 1082-1085

Riehl, H. (1954): Tropical Meteorology. New York, McGraw-Hill, 392 pp.

Simons, D.B., E.V. Richardson, M.A. Stevens, J.H. Duke, V.C. Duke and H. Riehl (1971): Venezuelan International Meteorological and Hydrological Experiment (VIMHEX) hydrology Report, Vol. I: Precipitation data and analysis. Civil Engineering Dept., Colorado State University, Ft. Collins, Colorado, 424 pp.

Smith, E.A. (1975): The McIDAS system. IEEE Transactions on Geoscience Electronics, GE-13, 123-136.

Smithsonian Meteorological Tables. Smithsonian Institution, 1958, 527 pp.

Staff, Experimental Meteorology Laboratory (1974): 1973 Florida Area Cumulus Experiment (FACE) operational and preliminary summary. NOAA Tech. Memo. ERL WMPO-12, 254 pp.

Warnecke G. and W.S. Sunderlin (1968): The first color picture of the Earth taken from the ATS-3 satellite. Bull. Am. Met. Soc., 49, 75-83.

Wiggert, V. and S. Ostlund (1975): Computerized rain assessment and tracking of south Florida weather radar echoes. Bull. Amer. Meteor. Soc., 56, 17-26.

Woodley. W.L., A.R. Olsen, A. Herndon and V. Wiggert (1974): Optimizing the measurement of convective rainfall in Florida. NOAA Tech. Memo. ERL WMPO-18, 99 pp.

Woodley, W.L., A.R. Olsen, A. Herndon and V. Wiggert (1975): Comparison of gage and radar methods of convective rain measurement. J. Appl. Meteor., 14, 909-928.

Woodley, W.L. and B. Sancho (1971): A first step towards rainfall estimation from satellite cloud photographs. Weather, 26, 279-289.

Woodley, W.L., B. Sancho, and A.H. Miller (1972): Rainfall estimation from satellite cloud photographs. NOAA Tech. Memo. ERL OD-11, 43 pp.

APPENDIX A: Operation and Use of the I^2S Digicol System

CONTENTS

A1. INTRODUCTION

This appendix is a guide to the operation and use of the I^2S (International Imaging System) Digicol system (referred to as the densitometer) owned by the Miami NOAA Community. The motivation for writing was to present, in a form understandable to the neophyte, a description of the instrument, a component-by-component outline of the use of the equipment, and a summary of the techniques which users have found valuable. What follows is not meant to supersede the I^2S and Sierra Scientific Corporation manuals for the system, but to supplement. For further details the reader is referred to the appropriate manuals.

The beginning user is urged to skim the entire appendix, as well as the I^2S manual, then to return to section A3 and work through all the procedures at the densitometer. There are only two cautions:

1. Protect the camera from the full intensity of the light table using the camera lens cap and/or masks to keep out excess light.

2. Don't force any knob, button, toggle switch or potentiometer (pot). All pots have locks which are down when open.

A2. SYSTEM DESCRIPTION

Briefly, the densitometer is an instrument capable of converting a positive or negative transparency, or paper image into a false color display, the color being determined by the gray shades of the original. Since the human eye is ill-suited to distinguish shades of gray, the advantage of the densitometer is that the information is color coded, making it easier to pick out, for example, bright clouds, or cold ocean currents. Quantitative gray shade determinations, area measurements, and color enhancements can also be performed.

For convenience, the densitometer will be described as composed of the following five areas: work table, camera, monitor, density control unit (DCU), and digital image processor (DIP). Each component of these areas is described below. Words or portions of words in capitals appear as labels on the equipment.

A2.1 Work Table

The work table holds a light table, an attached frame of four adjustable metal masks, and, at the end furthest from the camera, the main power switch with auxiliary outlets. Several additional items should always remain at the work table: a calibrated Kodak step tablet (fig. A1), a focusing pattern (fig. A2), masks made from exposed film, and the Polaroid camera with mount. The power supply for the light table, containing the on/off toggle, is located beneath the work table. When in use, an image is placed on the light table, under the mask frame and is viewed by the camera.

A2.2 Camera

A Sierra Scientific Corporation (SSC) Minicon plumbicon camera is mounted on a vertical track above the light table. The height of the camera can be varied and is controlled by a large knob to the right of the camera. The lock, a smaller knob below the height control, turns counter-clockwise to open, clockwise to close.

The camera itself is equipped with two Nikon lenses (focal lengths of 24 and 55 mm) and one spacer, 1-inch long. Maximum magnification possible is about 33x using the 55 mm lens with spacer, at the lowest focussable camera height. (See table 1 in the main text.)

On the top of the camera is the on/off switch at the right-hand edge and synch toggle at the left back. The synch should always be in the EXT MODE. A potentiometer on the left side of the camera is the pedestal. Its use will be discussed in section A3.6.

A2.3 Monitor

The Conrac monitor located at the top of the electronics rack is controlled by four knobs. These are, clockwise from the upper left, BRIGHTNESS, CONTRAST, VIDEO and POWER/CHANNEL. The first two control brightness and contrast of the monitor. With the VIDEO control at 0 db an image is displayed; at -6 db the image is brightness attenuated; a monochrome image appears at MONO; at OFF, no image is displayed. The monitor is not turned off at the VIDEO OFF, but at the POWER/CHANNEL OFF. Identical images are displayed in the A, B, or REMOTE positions of POWER/CHANNEL.

A2.4 Density Control Unit (DCU)

Located directly below the monitor is the DCU. Quantitative gray shade determinations are made with this unit. The ON/OFF switch and the power-on indicator light are found at the extreme left. The DMIN and DMAX, and RANGE controls will be discussed in sections A3.8 and A3.5, respectively. Two modes of operation are possible, selectable by the DENSITY/TRANSmission switch. The latter (TRANSmission) produces a linear input measuring percent of light transmitted through a film and ranging from 0.1 to 100 percent. DENSITY, defined as $-\log_{10}$ (transmission), is a log input and is measured in density units (DU). The CONTOUR DENSITY mode is used with DIP to determine densities of individual colors and is discussed further in section A3.10.

Figure A1. A Kodak step tablet.

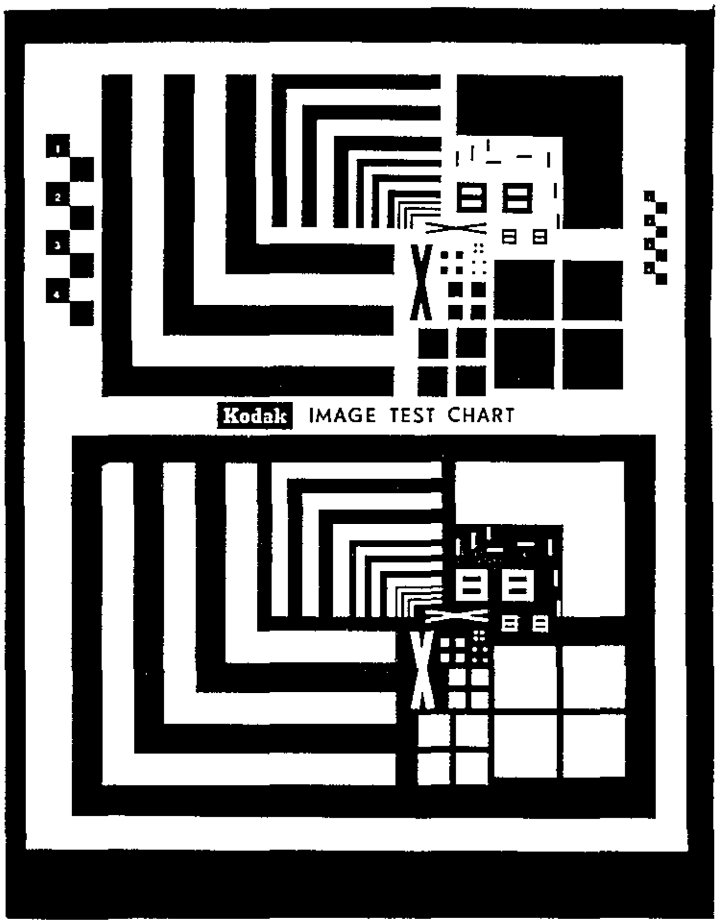

Figure A2. The focussing pattern.

On the right half of the DCU are found the MARKER, PROFILE, and four position controls. The MARKER is a movable crosshair, underneath which density or transmission measurements are made. (The measurement is displayed on the meter in the center of the unit.) The PROFILE consists of a solid vertical line and a dotted vertical line. The dotted line graphically represents the intensity of the image beneath the solid line. The black MANUAL CONTROL knobs position the MARKER and PROFILE in the x-y plane of the monitor, while the red START SCAN buttons will cause horizontal or vertical lines of the MARKER or PROFILE to scan automatically from the left (X SCAN) or top (Y SCAN) back to their original positions.

A2.5 Digital Image Processor (DIP)

Control of the color capability of the densitometer is in this portion of the instrument. The leftmost knob determines input to the monitor. TEST internally generates a color ramp for the monitor which displays the set up of the color as determined by all the remaining knobs and toggle switches of the DIP. A maximum of 32 hues, four shades of eight colors, is available. Displayed from left to right on the monitor are blues, yellows, greens, oranges, reds, browns, violets and magentas. In an image, the leftmost colors of the ramp are those gray shades approaching relative black; the rightmost represent grays approaching relative white. Of the other two positions of this knob, COLOR produces the false color enhanced view of the image under the camera, while the result of B/W is a black and white depiction.

Three banks of toggle switches, composed of two rows each, fill the DIP. The upper two rows consist of three-position switches which define the number of colors available to the range of gray shades in the image. In the middle position (N) the shade is shown normally. Contrary to what might be inferred from the labeling, when the toggle is up (R) the color becomes the shade of the color to its left; in the down (L) position the shade of the color on the right is assumed. The middle two rows of toggles determine whether a hue is COLOR, OFF, or a shade of gray (B/W). The bottom two rows control the electronic planimeter[10] and are also used in the CONTOUR DENSITY mode. At LEVel SELect the color becomes black.

Of the remaining knobs, buttons, and wheels, the OFFSET and GAIN knobs determine the location and width, respectively, of the test ramp, and the SCALE ADJust thumb wheels are used to calibrate the planimeter. Planimeter measurements are displayed on the DIP meter. The BLACK/WHITE knob determines contrast of an image in the B/W mode. The ON button of the DIP is located at the lower left. The LAMP TEST feature tests the DIP meter lamp. Three SLOPE ADJust potentiometers each effect color bar width changes over successive portions of the test ramp.

A3. SYSTEM OPERATION

A3.1 On/Off

A minimal one-hour warm-up is necessary before quantitative measurements can be made. During warm-up the following switches are on:

1. Main power at the right end of the work table.
2. Monitor POWER/CHANNEL at A, B or REMOTE.
3. DCU toggle ON.
4. DIP button ON. (If ON the square button at the lower right of the DIP is orange, otherwise it is white.)
5. Camera ON.

The light table needs no warm-up.

Turn off the above six switches (1 through 5, plus the light table) after use, unless the equipment has been reserved for later in the day.

A3.2 Monitor

To prevent blooming of the image on the monitor, the following procedure is suggested. This procedure will also prevent several shades of red and brown, or yellow and orange from being indistinguishable.

1. Place an image under the camera.
2. Select COLOR on the DIP.

---

[10] A planimeter is a device which determines the area of a plane figure from the measurement of the boundary of the figure.

3. Turn both BRIGHTNESS and CONTRAST counterclockwise until the monitor is blank.
4. Turn BRIGHTNESS clockwise until the image can just barely be discerned.
5. Turn CONTRAST clockwise until the colors are clearly visible.

A3.3 Camera Lens and Spacer

Removal of the lenses and/or spacer is accomplished by:

1. Pushing the metal button or gray plastic tab up, while turning the lens system to the right until the small white and red or white and black dots on each piece line up. At this point the lens is free to fall, so hold onto it.
2. To insert, align the white dot on one piece with the red or black dot on the other.
3. Turn to the left until the sections click into place.

A3.4 Camera Focus

The camera should be refocussed each time the height or lens system of the camera is changed. There is a focussing pattern at the densitometer for this purpose (fig. A2). To focus, rotate the lowest portion of lens. The best focus can most easily be seen in the B/W mode.[11]

A3.5 Camera f-stop and DCU RANGE Selection

Each image covers a range of gray shades. Thus, for each picture an appropriate f-number and RANGE setting must be selected. Generally, pictures of the same type (e.g., SMS/GOES infrared images) use identical f-number and RANGE settings.

To select the appropriate f-number[12]:

1. Set the camera at the height to be used, with the appropriate lens configuration.
2. Set the DCU to TRANS.
3. On the image visually pick out one of the brightest areas and one of the darkest.
4. Turn the PROFILE ON and locate the bright area under it.

---

[11] In the DENSITY mode an image appears fuzzier when displayed on the monitor than when viewed by eye from the original. The display in the TRANSmission mode is sharper than in the DENSITY mode.

[12] The f-stop determines the lens' aperture size - the larger the f-number, the smaller the aperture, and vice versa.

Table A1. Max and Min calibration steps for the corresponding f/number and RANGE setting

f/number	RANGE	DCU calibration steps* Max	Min
32.0	1	1	9
22.0	2	2	10
16.0	3	3	11
11.0	5	5	13
8.0	7	7	15
5.6	9	9	17
3.5	10	11	19

*Of a calibrated step tablet

5. Set the aperture at f/32. Mark the relative maximum displacement of the profile over this bright area and record the f-number.
6. Continue to mark the profile displacement while opening the lens (i.e., decreasing the f-number) to each f-stop.
7. Stop down to f/32.
8. Locate the dark area under the profile and mark its relative maximum displacement while changing the f-number, as before.
9. Use the f-number which results in the greatest displacement between the profile position of the darkest and corresponding brightest areas.
10. Set RANGE to the correct value as defined in table A1 by the f-number.

If the above selection procedure seems to result in inappropriate settings for the DENSITY mode, try the following. Starting at f/32, open the camera f-stop until the image is easily viewed at the dark grays, yet doesn't "bloom" or overdrive the camera at the bright portions. Again, as the f-number is changed, the corresponding RANGE number in table A1 should be used.

A3.6 Pedestal

The pedestal control located on the left side of the camera is set by the electronics technician and should be changed only according to the procedure in section A3.8. At the time of writing, the densitometer is calibrated so that the pedestal reads 6.05, where the 6 is indicated in the window, and the 0 and 5 from the circular scale of the vernier. With this calibration, the camera and DCU combinations of table A1 should be used. Depending on magnification, the wedge calibration steps may vary up to ± 4 steps.

With the 55 mm lens (no spacer) at the maximum height above the light table and viewing the wedge, the profile will appear linear in the DENSITY mode[13], as below.[14]

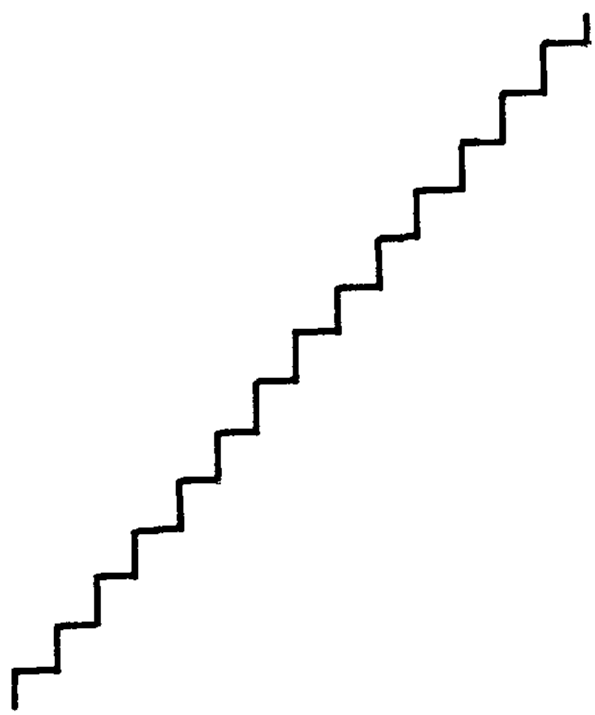

[13]The step wedge is linear in density, but varies exponentially in transmission.

[14]On the densitometer the three profiles shown here and on the next page will blank out before and after nine steps.

Use the pedestal to remove any extreme non-linearities such as:

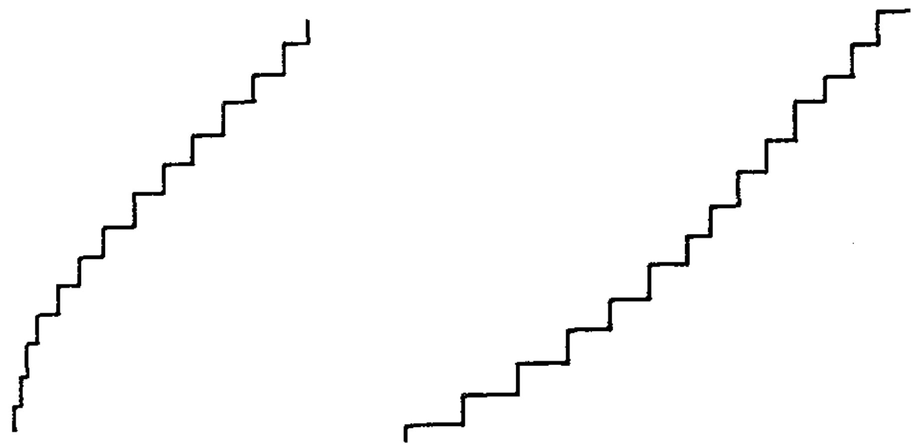

A3.7 TEST Ramp

To use the COLOR DENSITY feature, a calibration of the ramp is required. A ramp calibration may also be necessary for individual users, each user defining his or her own calibration procedure.[15] The procedure listed below is that necessary for use of the CONTOUR DENSITY mode, but is worth doing routinely. Often system "problems" turn out to be a previous user's settings.

1. Select the TEST mode on the DIP.
2. Check that all 32 colors are on and distinguished from another.
3. Adjust the OFFSET until the leftmost blue (color #1) touches the left edge of the monitor.
4. Adjust the GAIN until the rightmost magenta (color #32) touches the right edge of the monitor.
5. Repeat steps 3 and 4 as necessary.

It is often convenient (but not necessary for the CONTOUR DENSITY mode) to adjust the SLOPE ADJust pots until all color bars are as uniformly wide as possible.

---

[15]It should be remembered that the colors themselves are arbitrary and that the meaning ascribed to any color level is defined by the user.

A3.8 DCU Calibration

The DCU is calibrated with a calibrated Kodak gray wedge of 21 steps, approximately ranging from .06 density units (DU), or 87.1 percent transmission, to 3.00 DU (0.1 percent). Table A2 lists representative values of density and transmission for each step of a particular Kodak step tablet. The actual calibration of each step tablet is included with the tablet and that calibration is the one to be used in the succeeding sections. Although the densitometer is capable of measuring densities over the entire range of the wedge, the workable range for a particular f-stop and RANGE setting is about 1.30 DU. The max and min calibration steps for each f-stop and RANGE setting have been given in table A1.

Calibration is necessary only if quantitative density or transmission measurements are to be made. Before data analysis, all measurements must be corrected with an appropriate relationship from section A4.2 and the procedure of section A4.3, to account for drift that occurs in either the DCU or the pedestal.

After the pedestal check (section A3.6) has been made, calibration proceeds as follows:

1. Select the height of the camera, lock it, and focus. If the camera height is changed, the DCU must be calibrated at the new height.[16]
2. Turn ON the MARKER and center it on the monitor.[17]
3. Select the f-number and RANGE setting appropriate for the image to be analyzed. (See section A3.5.)
4. Select DENSITY or TRANSmission,
5. Refer to table A1 for the steps of the Kodak wedge on which the DCU will be calibrated. As an example, assume f/16 and RANGE number 3 are used. The densitometer will be calibrated on steps 3 and 11.
6. Place the minimum calibration step (in this example, #3) under the crosshair. Record its value, d_{lower}.
7. Place the maximum calibration step (in this example, #11) under

[16] Likewise, density or transmission readings taken at one image magnification cannot readily be compared with those made at any other magnification. Although the density or transmission measurement is made for a point, the measurement is the result of an integration over a finite image area. Thus a measurement made at a greater magnification (that is, with the camera closer to the light table) has been integrated over a smaller image area than a measurement of the same point made at a lesser magnification (a greater camera height).

[17] Because of the non-linearity of the camera across its field of view, the density or transmission of an image point changes as the point's position changes in the field of view. This can be seen by viewing an image in the COLOR mode. The color of any area of the image varies as the image is displaced from the camera center. For this reason it is urged that all measurements be made at a fixed point on the monitor, moving the image rather than the marker.

Table A2. Representative density and transmission values of a calibrated step tablet

Step number	Density (DU)	Transmission (Percent)
1	.06	87.1
2	.21	61.7
3	.36	43.7
4	.51	30.9
5	.66	21.9
6	.80	15.8
7	.96	11.0
8	1.12	7.6
9	1.28	5.3
10	1.44	3.6
11	1.60	2.5
12	1.74	1.8
13	1.88	1.3
14	2.03	0.9
15	2.18	0.7
16	2.34	0.5
17	2.49	0.3
18	2.64	0.2
19	2.78	0.17
20	2.93	0.12
21	3.08	0.08

the crosshair, and record its value, d_{upper}.

8. Determine the difference of the min and max calibration steps as measured above ($\Delta d = d_{upper} - d_{lower}$) and compare this to the difference of the values of the same two wedge steps as given on the calibration sheet provided with the step tablet, ($\Delta D = D_{upper} - D_{lower}$).
9. Adjust the DMIN[18] knob until the densitometer-measured difference equals the difference computed from the calibration sheet, that is, $\Delta d = \Delta D$. If $\Delta d < \Delta D$, turn DMIN clockwise and vice versa.
10. Once the difference is correct, use the DMAX knob to adjust the value of either calibration step to the correct measurement.

In some cases the above procedure does not converge the maximum and minimum calibration steps to the proper values, even after numerous repetitions. In that event if the difference between the achieved calibration and the Kodak calibration is greater than 0.10 DU, the following must be done:

---

[18]The DMIN and DMAX can be thought of as slope and offset controls, respectively.

11. Position the DMIN and DMAX knobs so that the dot on each control is at 12 o'clock.[19]
12. Place the minimum calibration step under the marker. Simultaneously turning DMIN clockwise and DMAX counterclockwise; adjust until the corresponding step value is measured on the DCU.
13. Placing the maximum calibration step under the marker, gently adjust the pedestal until the corresponding value is attained.
14. Repeat 12 and 13 until the appropriate readings are achieved on both wedge steps.

For the NOAA instrument in the DENSITY mode the darker gray shades are noisier (i.e., show more fluctuations) than the bright, complicating the DCU calibration at the dark end. In the TRANSmission mode the noise level is lower over the range of operation than is the noise level of the density mode. It has also been found that as the picture magnification is decreased, calibration becomes easier and more stable, and noise level decreases.

A3.9 Planimeter Calibration

The electronic planimeter of the DIP measures the percent of the image on the monitor covered by a selected color or colors. The planimeter can be calibrated in either the TEST, COLOR or B/W modes.[20] Depending on the use of the planimeter, the appropriate mode is selected as follows. For the area measurements on the image, calibrate in the COLOR mode; to measure the areas of the ramp's color bars, calibrate in the TEST mode. A re-calibration of the planimeter must be performed if the SLOPE ADJust, OFFSET or GAIN controls, camera pedestal, or camera height are subsequently varied.

The calibration procedure is:

1. Select TEST or COLOR.
2. Set up camera height, focus, f-number, RANGE, DENSITY or TRANSmission, DIP colors, SLOPE ADJust and test ramp if an image (COLOR mode) is to be analyzed. Lock the camera in place.
3. In the COLOR mode, OFFSET the test ramp so that no colors appear on the monitor outside the image area in the upper and left-hand borders. These borders contribute significantly to the total area, and must be offset so that they are not counted in the calibration. Depress all 32 toggles in the bottom two rows to LEVel SELect. (An individual color is blackened when the corresponding toggle is depressed, except in the B/W mode.)
4. Turn the SCALE ADJust thumb wheels until 100.0 appears on the AREA PERCENT meter. The left-hand SCALE ADJust can be thought of as the tens digit, the unit being the right-hand thumb wheel. Note that

---

[19]This is to avoid use of the non-linear ends of the pots.

[20]In the first two modes, the color(s) under analysis become black when routed to the planimeter for measurement. This change does not occur in the B/W mode.

the SCALE ADJust thumb wheels do not affect the planimeter calibration in a linear fashion, because the thumb wheels inversely control the instrument's dividers.

5. If the planimeter cannot be calibrated to 100.00 percent $\pm$ 1.5 percent, change one of the parameters in #2 above or use the apportioning scheme described below.

The planimeter cycles about once per second, and the meter reading fluctuates slightly at that time. Fluctuations in the measurement will range from 0.1 to 2 percent. Because of the fluctuations, the meter will never read a firm 100.0 percent.

If for some reason the image must be masked during use of the planimeter, the image appearing on the monitor must not be more than three-quarters masked. With more than 75 percent of the field of view masked, the planimeter cannot be calibrated to 100 percent. If the field of view must be masked, an apportionment scheme can be used, but is not recommended.

1. Measure the percentage area of the masked image, a_1.
2. Measure the percentage area of the color(s) of interest, a_2, by depressing the corresponding toggle switch(es).
3. Knowing the actual area A_1 (in km^2, ft^2, etc.) of the image seen on the monitor, the actual area of the portion of interest, A_2, is found by proportion:

$$\frac{a_2}{a_1} = \frac{A_2}{A_1}$$

A3.10 CONTOUR DENSITY

The CONTOUR DENSITY feature determines the density of a given color, once the instrument is calibrated.

1. Calibrate TEST ramp as in section A3.7.
2. Calibrate DCU as in section A3.8.
3. Turn CONTOUR DENSITY of DCU to ON.
4. On the bottom bank of toggle switches of the DIP, depress the toggle of the color for which a density determination is to be made, that is, place the toggle in the LEVel SELect position. The lower limit of the density range covered by the chosen color will appear in the DCU meter.
5. If more than one toggle in the lower bank is depressed, the reading on the DCU meter is the lower limit density of the color with the smallest identification number. For example, if colors number 2, 6, 12, 13, and 14 are at LEVel SELect, the density of color number 2 will be displayed.
6. After the density of the color has been determined, set CONTOUR DENSITY to OFF. If this mode is ON, subsequent density or transmission readings will be incorrectly calibrated.

At the time of writing the CONTOUR DENSITY mode appears to result in incorrect values of greater than .10 - .20 DU, with density determinations in the CONTOUR DENSITY mode being too high.[21]

A3.11 Polaroid Camera

There is a Polaroid Land camera with an industrial accessory mount available for photographing the monitor. The open end of the hood fits against the monitor. In this position the camera is focussed on the monitor screen. (There is no focus on the camera.)

It may be necessary to take several test shots to ascertain the best camera settings for the user's monitor set-up. Note that the MONITOR BRIGHTNESS and CONTRAST can drastically change the photographed image. Polaroid film was not found to result in color photographs of very high quality. (An alternative is suggested in section A4.7.)

A4. MISCELLANEOUS TECHNIQUES

Several techniques and correction procedures have been found to be useful or necessary for analyses performed with the I^2S Digicol system. These are described below. Since limited types of analyses have been made to date, it is left to future users to explore additional idiosyncrasies of the instrument which have not been discovered and cataloged here.

A4.1 Miscellaneous Enhancement Techniques

Several enhancement suggestions follow. No enhancement technique can produce information which is not contained in the image itself. Enhancements are only aids to the human eye, which is limited in discerning gray shades.

1. The SLOPE ADJust pots can be used to color enhance gradients in the image of interest. The narrower the width of the color bar, the smaller the density or transmission range covered by the color. Thus, a tight gray shade gradient of an image can be delineated with that portion of the TEST ramp that has been narrowed. It may be of some advantage to display each color in the gradient individually. To do so, turn off most of the shades surrounding the gradient and display the colors in the gradient one at a time.
2. It is often useful to make the background of the image one or two

[21]The CONTOUR DENSITY mode was checked with the step wedge after performing the calibration procedures of this section and of A3.8. The density of a specific color on the step wedge was then compared to the density of the same color as measured in the CONTOUR DENSITY mode. For example, step number 7, predominately color #14, measured 0.90 DU with the DCU, whereas color #14 was measured as 1.86 DU in the CONTOUR DENSITY mode.

colors, employing the remaining shades in the brightness range of interest.

3. Setting every other shade black (OFF on the middle bank of toggle switches of the DIP, or LEVel SELect on the lower bank) sharply defines the color contours. This arrangement makes a particularly pretty picture.
4. Combinations of black (OFF), gray (B/W) and color (COLOR SEL) of the middle bank of toggle switches can result in striking displays.

A4.2 Density and Transmission Correction Relationships

In section A3.8 it was mentioned that all density or transmission measurements made with the DCU must be corrected. The correction is necessary to compensate for the drift, with time, of the DCU calibration. At maximum magnification (that is, using the 55 mm lens and spacer at the lowest camera height for which the camera can be focussed), the drift is greatest, decreasing as the magnification is decreased. The corrections below transform the density or transmission measurements made with the densitometer (referred to as the "densitometer system") into "ideal" measurements, that is, measurements that would have resulted if the DCU were absolutely stable or able to measure perfectly. The correction relationship, (A1) for density, or (A6) for transmission, must be used on all data before any analysis is undertaken.

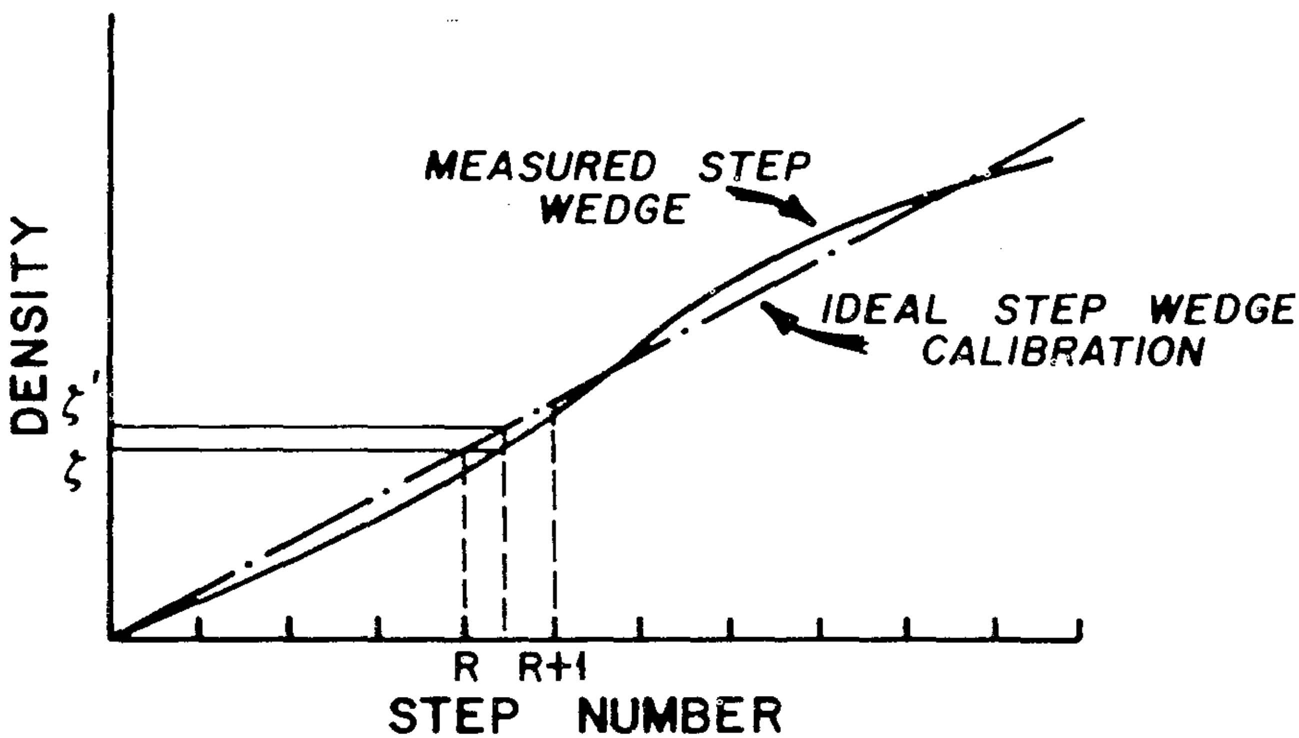

Figure A3. The linear relation of step number to density.

If the densitometer-measured densities of the Kodak step wedge are plotted versus step number, the plot may appear as in figure A3. It is inconsequential whether these data are taken immediately after calibration or 60 minutes later. To account for the measured wedge excursion from what should be, density data need to be corrected with the relationship:

$$\rho' = \left[\frac{(\rho - d_R)}{(d_{R+1} - d_R)} \quad (D_{R+1} - D_R) \right] + D_R \tag{A1}$$

where D_R = "ideal" density reading of the Rth step, that is, what the step should read according to the Kodak calibration.

R = step number of the Kodak wedge,

d_R = density reading of the measured Rth step, that is, what the densitometer measured,

ρ = density measurement (of an image point) which lies between d_R and d_{R+1},

ρ' = corrected density.

Equation (A1) can be derived in the following manner. The equation of an "ideal" wedge calibration line segment between steps R and R+1 is

$$Y = MX + B \tag{A2}$$

where by definition of the slope,

$$M = \frac{D_{R+1} - D_R}{(R+1) - R} = D_{R+1} - D_R.$$

Let $X = R$, then $Y = D_R$. Substituting the above values of X, Y, and M into (A2) results in the definition of B,

$$B = D_R - (D_{R+1} - D_R)R.$$

Therefore

$$Y = (D_{R+1} - D_R)X + D_R - (D_{R+1} - D_R)\ R. \tag{A3}$$

In a similar manner, the measured wedge line segment between steps R and R+1 is

$$y = (d_{R+1} - d_R)x + d_R - (d_{R+1} - d_R)R. \tag{A4}$$

Equation (A1) is the result of solving (A4) for x and substituting the results into (A3) letting

$x = X$
$y = \rho$
$Y = \rho'$
The rationale for these substitutions can be found in figure A3.

The correction for transmission measurements is of the same form as (A1), because by definition density is $-\log_{10}T$, and $\log_{10}T$ is a linear function of step number, T being transmission. Thus the following substitutions are made into (A1):

$\rho \Rightarrow \log \tau$
$d \Rightarrow \log t$
$D \Rightarrow \log T$

where all logarithms are base 10,

τ = transmission measured at an image point,
t = transmission measured from the Kodak wedge with the densitometer,
T = ideal transmission value per the Kodak calibration.

Then

$$\log \tau' = \left[\frac{(\log \tau - \log t_R)}{(\log t_{R+1} - \log t_R)} (\log T_{R+1} - \log T_R) \right] + \log T_R \tag{A5}$$

which can be solved for τ' and written as

$$\tau' = T_R \, 10^g \tag{A6}$$

$$g = \left(\log \frac{T_{R+1}}{T_R}\right) \left(\log \frac{\tau}{t_R}\right) \div \left(\log \frac{t_{R+1}}{t_R}\right) \tag{A7}$$

There are some analyses where a particular "ideal" transmission or density value is specified and subsequently needs to be determined in the densitometer system. An example of this is a brightness threshold which has been defined in the "ideal" system and must be converted into that value which the densitometer will measure according to its operating performance. The entire procedure is given in section A4.4, and makes use of the inverse relationships (A8) and (A10). For density the inverse relationship is the solution of (A1) for ρ:

$$\rho = \left[\frac{(\rho' - D_R)}{(D_{R+1} - D_R)} \quad (d_{R+1} - d_R) \right] + d_R. \tag{A8}$$

The inverse transmission relationship is

$$\log \tau = \left[\frac{(\log \tau' - \log T_R)}{(\log T_{R+1} - \log T_R)} \quad (\log t_{R+1} - \log t_R) \right] + \log t_R \tag{A9}$$

or

$$\tau = t_R \; 10^h \tag{A10}$$

$$h = \left(\log \frac{t_{R+1}}{t_R} \right) \left(\log \frac{\tau'}{T_R} \right) \div \left(\log \frac{T_{R+1}}{T_R} \right) \tag{A11}$$

A4.3 Density and Transmission Measurement Procedures

It is highly recommended that quantitative gray shade measurements be made in the following manner:

1. Warm up the densitometer, one hour before calibration.
2. Calibrate the DCU in the appropriate mode.
3. Measure and record each step of the Kodak wedge in the appropriate calibration range specified in table A1.
4. Make quantitative gray shade measurements (density or transmission), on the image of interest. Depending on the noise level and drift of the DCU, quantitative measurements should be made for no longer than 5 to 15 minutes at maximum magnification, or for a longer time period at lesser magnifications, before proceeding to the next step.
5. Remeasure and record the Kodak wedge.
6. Repeat steps 4 and 5 until all measurements are made. If the measurements of the Kodak wedge become grossly different from what should be, recalibrate the DCU.
7. In correcting the above measurements, use the average of the Kodak wedge readings as the values of d_R or t_R in (A1) or (A6). Make sure that the wedge values averaged are those which were measured immediately before and immediately after the gray shades to be corrected were measured. As an example, assume the following data have been measured from an image:

.04	.22	.34	(.47-.48)	(.62-.63)	(.82-.85)	(.96-.98)	(1.12-1.16)	(1.28-1.35)	I
	a	1.13							
	b	1.18	II						
	c	1.16							
.02	.19	.33	(.45-.47)	(.59-.60)	(.78-.80)	(.91-.94)	(1.09-1.14)	(1.28-1.34)	III
	d	1.09							
	e	1.25							
	f	1.08							
	g	1.18	IV						
	h	1.10							
	i	1.16							
.00	.17	(.29-.30)	(.43-.44)	(.57-.59)	(.78-.79)	(.94-.97)	(1.10-1.16)	(1.27-1.36)	V

In the first row labelled I, the densities measured on steps 1 through 9 of the Kodak step tablet are recorded. Enclosed in parentheses are the range of densities measured at a particular step. Values "a" through "c" are the raw density readings for points of interest, followed by a line labelled III, recording wedge measurements. Again, "d" through "i" are raw density points, followed by a wedge measurement, line V. The densities marked II are to be corrected by the average of wedge readings I and III; densities marked IV are to be corrected by the average of III and V. The densities were corrected by (A1) with the step values in table A2. The corrected densities are:

a'	1.12
b'	1.17
c'	1.15
d'	1.09
e'	1.23
f'	1.08
g'	1.17
h'	1.10
i'	1.15

A4.4 Color-Density Determinations

It is convenient, at times, to calibrate a given color to correspond to a particular density or transmission, rather than use the CONTOUR DENSITY mode to determine the density of a color. If so, the following applies:

1. Choose the appropriate mode, DENSITY or TRANSmission
2. Calibrate the DCU in this mode at the appropriate f-stop and RANGE, and record the wedge measurements.

3. Given a density or transmission value N, which is to be color coded, determine the corresponding value n of this cutoff N in the densitometer system, using the inverse equations (A8), (A9), or (A10) of section A4.2, and the wedge readings recorded in step 2 above.
4. Turn on the MARKER and fix it in the center of the MONITOR.
5. Search the image of interest for a point that has the value of n.
6. Choose a color to represent the cutoff; for example, red number 20. Set several colors to the right of the chosen color to LEVel SELect. (For example, set colors 21 through 24 to LEVel SELect.)
7. Turn DIP OFFSET until the chosen color just starts appearing under the MARKER.
8. To check this setting, measure the value of another point at which the color is just starting to appear. If the value of this new point is much greater or less ($\pm$ .05 DU) than the cutoff value n, adjust the OFFSET accordingly.

An example of this procedure, which arose out of a project to estimate rainfall from the ATS-3 satellite, follows.

1. Set up the camera and DCU according to the parameters given in table 1 in the main text.
2. After calibrating the DCU, find and measure the density of the brightest cloud, ρ_{cb}, on the picture of interest.
3. Measure the step wedge in the region of ρ_{cb}. Correct ρ_{cb} with (A1) of section A4.2 and the step wedge readings to obtain ρ'_{cb}.
4. Generate the salt flat correction factor, c, by

$$c = 1.09 - \rho'_{cb}$$

5. A cloud threshold was determined to be 0.86 density units. For the picture of interest determine the adjusted cloud threshold k' as

$$k' = 0.86 - c$$

6. Convert k', which has been calculated assuming an ideal wedge calibration, to k, the threshold for the picture of interest. This is done using the inverse density relationship, (A8). That is, knowing k', determine the steps of the ideal equation between which k' lies. Measure these steps on the densitometer to determine d_R and d_{R+1}. Then,

$$k = \left[\frac{(k' - D_R)}{(D_{R+1} - D_R)} \quad (d_{R+1} - d_R) \right] + d_R .$$

7. In the cloud field of interest find a point where the density is equal to k. Offset the test pattern until color number 18, for example, is just appearing at this point. Color number 18 then represents the threshold brightness for the particular picture displayed.

If a different normalizing standard is used, substitute the appropriate quantities in steps 2 and 4 above.

A4.5 Color Normalization

The following procedure calibrates the I^2S densitometer so that clouds of the same normalized density or transmission will be the same color from one picture to the next, regardless of differences produced by sun angle and processing. The color suggested in step #11 may be changed to suit the user's preference.

1. Set the camera at the appropriate height.
2. Select the density or transmission mode on the DCU.
3. Turn to TEST mode on the DIP and turn on MARKER. Adjust color ramp so that leftmost blue aligns with the left edge of the horizontal line and the rightmost magenta with the right edge. (This is the procedure of section A3.7.)
4. Check color ramp to see that desired colors will be used. Use the same number of colors in all pictures.
5. Use the SLOPE ADJust pots to make the color bar widths as even as possible.
6. Density contour mode switch on the DCU should be off (down).
7. Select f-stop and RANGE number.
8. Focus camera.
9. Calibrate the DCU with the Kodak step table according to the procedure in section A3.8.
10. Turn off PROFILE and MARKER.
11. Position transparency under camera so that the standardization area appears on the monitor. (See seciton A4.6.) Turn the offset control on the DIP so that color #20 (the leftmost red on the test pattern) is just starting to appear in the salt flat.
12. Position the transparency so that the area of interest appears on the monitor. Photograph the monitor, if desired.

A4.6 Standardization

No two photographic images are exactly alike. There is some variability from one picture to another caused by processing differences, or in the case of satellite images, signal level changes. To correct for these changes, a standardization procedure was performed on each satellite image. This procedure, outlined below, was derived for ATS-3 (visible) images on which the features of interest were clouds within 125 n mi of Miami, Florida. The user should be able to construct a normalizing procedure based on the procedure outlined and a suitable standard. Additional discussions of image standards and normalization appear in section 3 of the main text and in Appendix C.

A standardizing factor was generated from a Bolivian salt flat, Salar de Uyuni at 67°W and 20°S. The advantages of the salt flat were (a) it was included on almost every ATS-3 image, (b) it was cloud-free on almost every image[22], and (c) its brightness fell in the brightness range covered by the clouds. Item (c) is most important, as the gamma amplification curve of the ATS-3 images is composed of linear segments, and a relative change of gray scale in one portion of the gamma curve (i.e., brightness range of the image) is not directly applicable to any of the remaining segments. For this reason, a cloud normalization scheme employing cloud-free ocean resulted in thresholds which were too high for our purposes.

This standardization procedure also makes some correction for sun-satellite geometry. Unfortunately, the correction breaks down on pictures prior to 1430Z or later than 1930Z. The standardization procedure is as follows:

1. Record the step wedge calibration, once the DCU has been calibrated.
2. Measure the salt flat density on the picture of interest.
3. Measure densities at the clouds of interest.
4. Record the step wedge readings again after 5 to 15 minutes have elapsed.
5. Continue to make density measurements and step wedge readings, noting between which pair of step wedge readings each set of density measurement was made.
6. Correct the salt flat and all density measurements by (A1) of section A4.2. To obtain the d_R's. use the average of the step wedge readings which were made immediately before and after the density sets.
7. Using corrected salt flat density ρ'_{sf}, determine the salt flat correction factor c[23]:

$$c = 1.00 - \rho'_{sf}$$

8. Algebraically add c to all the corrected cloud density readings.

A4.7 Photographing the Monitor

Good photographic images were obtained from the densitometer using a Pentax Spotmatic camera and Kodak high speed Ektachrome film (EHB). Using f/2.8 and a shutter speed of one-eighth second, good color discrimination and sharp monitor resolution resulted.

Acknowledgment. Thanks are extended to Richard Bennett and Howard Roberts for reviewing the several versions of this appendix.

---

[22]Analyses were made in May through October. Clouds rarely occurred over the salt flat during these months.

[23]The relative standard slat flat is defined as 1.00 DU.

APPENDIX B: A Calculation of Rain Volume from an ATS-3 Image

The following is a sample rain volume calculation made using ATS-3 images and the scanning, false color densitometer described in Appendix A. In this particular calculation the rain volume within the Florida Area Cumulus Experiment target area is computed. If rain volumes from individual clouds are required, steps 5, 18, 19, 20 can be omitted.

1. Determine the cloud threshold density for the images of interest as described in section A4.4.
2. Trace these threshold contours onto acetates for each image in the sequence.
3. Determine cloud entities. A cloud entity is defined as those clouds which were or are merged at any time. When determining entities, the full sequence of both tracings and negatives is used. Beginning with one of the later tracings and the corresponding negative, uniquely label each cloud mass. Work backward in time to the next tracing and negative. Using both sets of images, compare and match cloud masses. Continue matching from image to image until all clouds on all pictures have been labelled. Rework through the sequence at least once to check the matching. Recombine and relabel clouds as necessary.

   An example of entity identification is shown in figure B1, which is the tracings of the cutoff contours and the quadrilateral target area for the first four images of the 6 July 73 sequence. Starting with figure B2, the last tracing from the sequence, cloud entities have been given unique, alplabetic identifiers. Note the time gaps in the sequence of figure B1. These gaps add to the difficulty of following cloud entities.
4. Determine and record the entity areas in units of km^2. In figure B1, individual cloud areas are recorded next to each cloud. These areas have been measured with a hand planimeter[24] and converted, by the appropriate factor, to km^2. The entity areas, that is, the sums of the individual clouds, are recorded at the edge.
5. Measure and record the areas of the entities within the target area. These areas, along with the percent of the entity within the target area, are also recorded at the edge.

The following steps are illustrated by figure B3 in which mass A of figures B1 and B2 is used:

---

[24] It is our experience that planimetering directly on the acetate is inadvisable. The small coefficient of friction of the material causes the planimeter to slip rather than roll and results in area measurements which are too small. The contours are usually retraced from the acetates onto tracing paper.

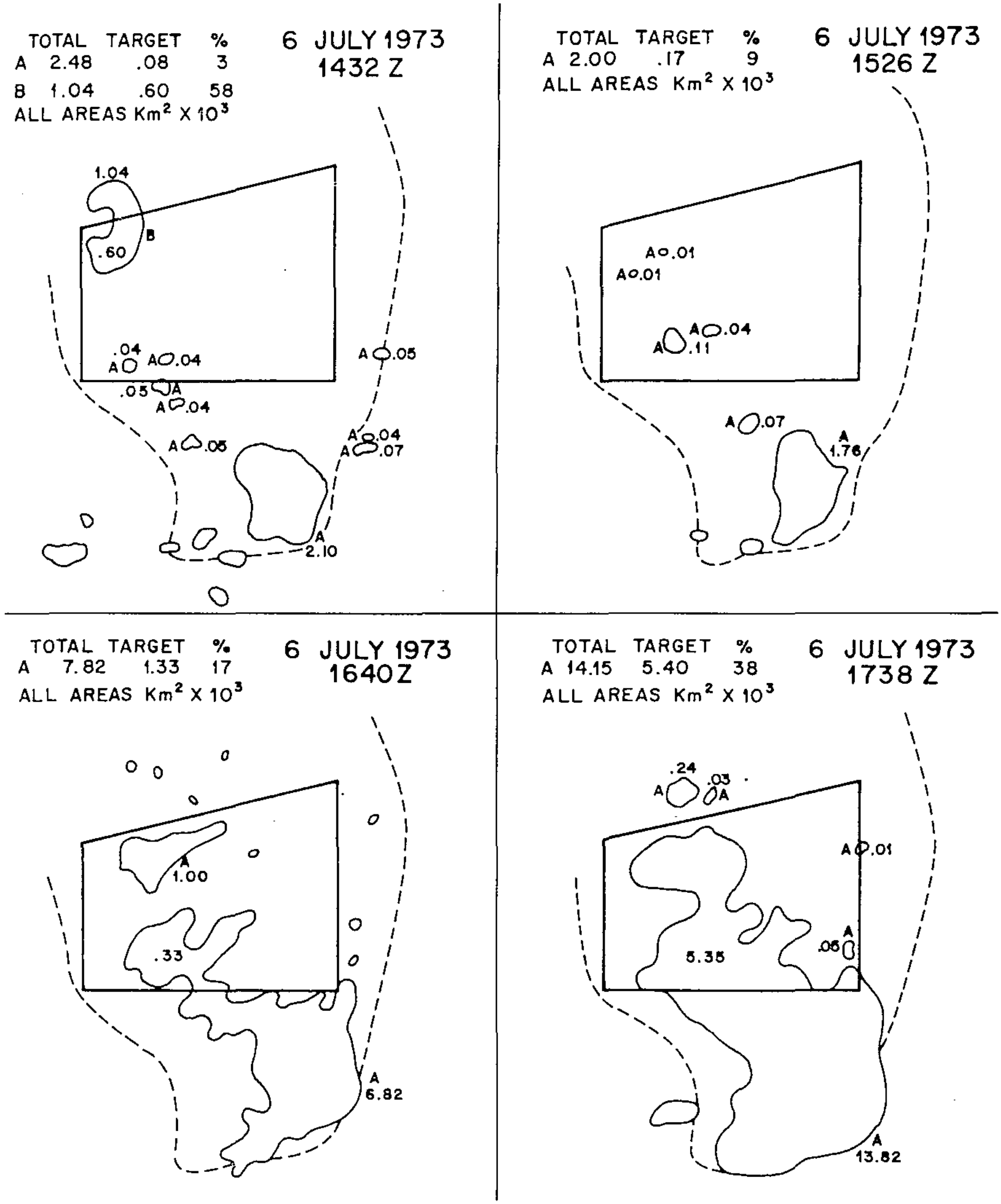

Figure B1. The first four tracings in the 6 July 1973 sequence. The solid black lines are the cloud 80 digital count contours and the dashed line is Florida. The quadrilateral is the FACE target, the region for which the rain calculation is to be made.

6. Plot the entity total area, A_C, versus image time GMT, for each entity, one entity per graph (see figure B3).
7. Draw a smooth curve through these plotted points.
8. Record A_M beneath each relative maximum. There may be several relative maxima per entity. For example, in figure B3, there are three relative maxima for the entity "Cloud A."
9. Compute A_C/A_M at appropriate intervals,[25] using the A_M specified by the criteria of step 10. In this example, the calculations have been made half-hourly, on the hour and the half-hour. Where the tangent to the curve changes rapidly, calculations were made at 15-min intervals, or less. It is not uncommon to use intervals of 5 and 10 minutes on the down side of A_M.
10. Criteria for relating A_C to A_M:

    a. All points for which cloud area is increasing with time are referenced to the relative max towards which they are increasing.
    b. All points for which cloud area is decreasing with time are referenced to the relative max from which they are decreasing.
    c. All relative mins are considered to be increasing to the next relative max and are therefore referenced to that max.

[25]The user's needs define the appropriate interval, although intervals shorter than 5 minutes are probably meaningless.

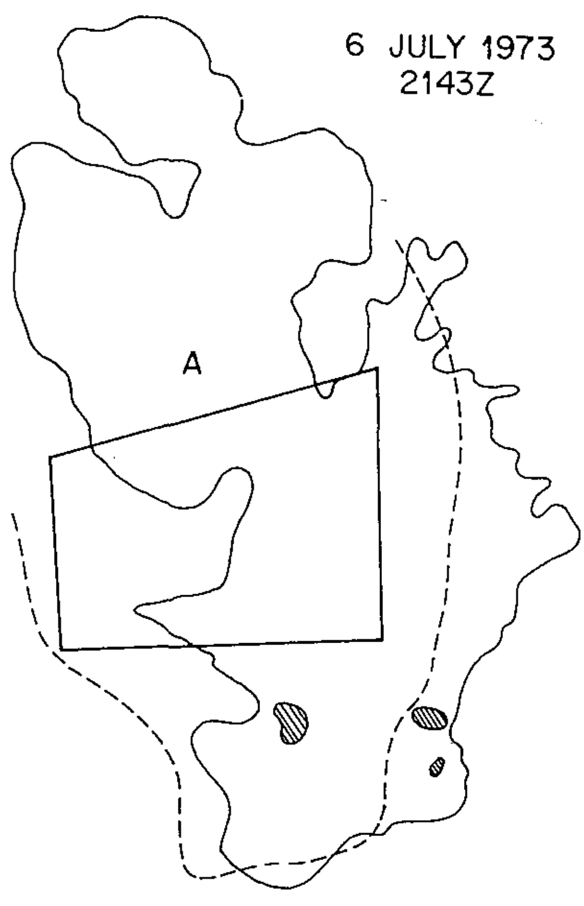

Figure B2. The last tracing in the 6 July 1973 sequence. The solid and dashed lines and quadrilateral are as in fig. B1. The shaded areas are holes in the 80 digital count contour.

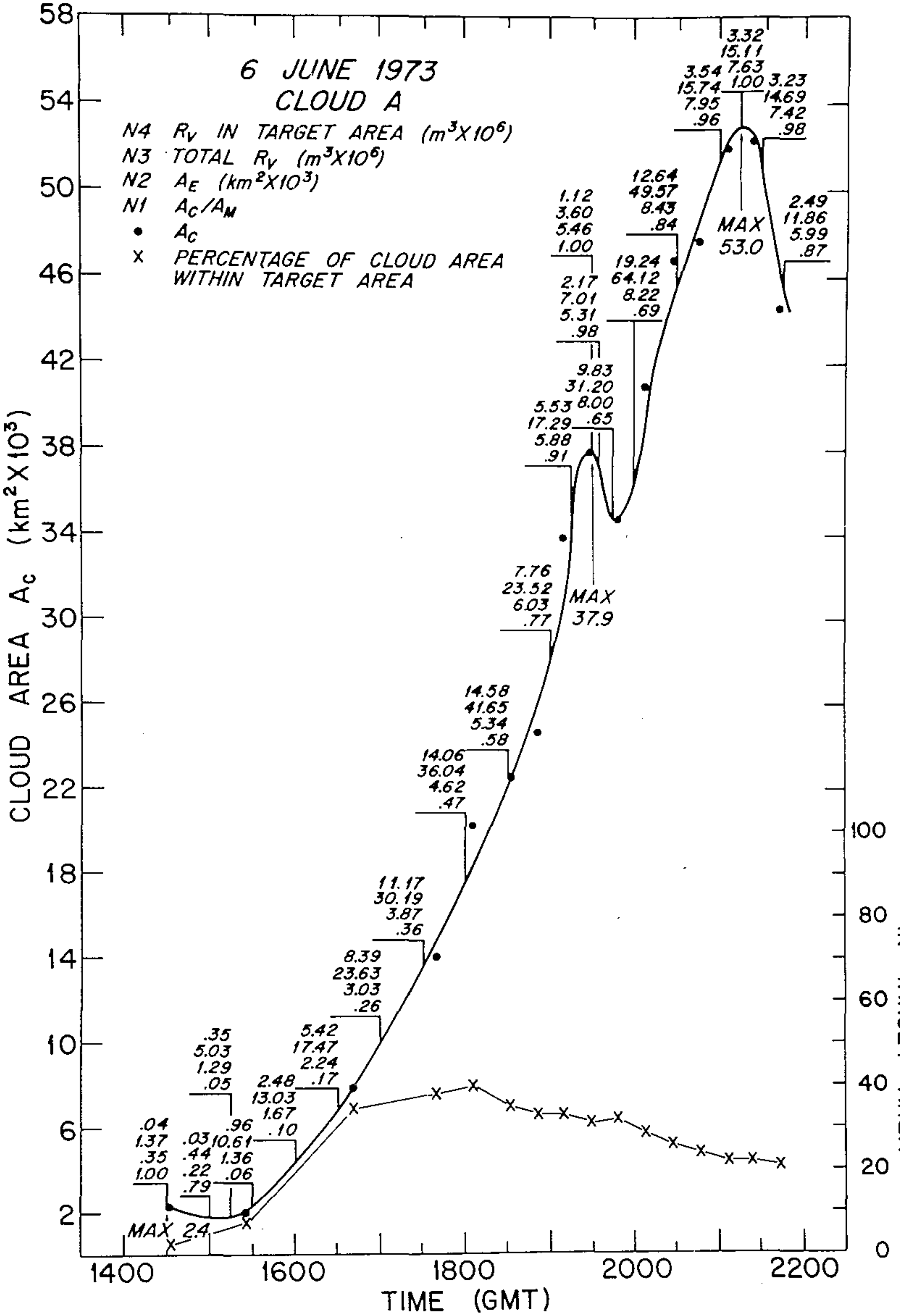

Figure B3. A sample rain volume calculation for one entity.

d. If no relative max occurs at the beginning or at the end of sequence, that is, if the cloud is increasing but the data stop before the area decreases again, or if the cloud is decreasing but the data begin after the area increase, then no computations can be made for those times associated with the unseen max.[26]

11. Record A_C/A_M on the cloud area graph along the time line at which it was computed.
12. Compute echo area, A_E, using the tabulated cloud area-echo area relationship (table B1). In table B1, "increasing" and "decreasing" refer to the time change of <u>cloud</u> area, and it is necessary to know whether cloud area is increasing toward or decreasing from the reference relative max, because the echo area inferred depends on this. For example, on figure B3 at 1935 Z, $A_C/A_M = .98$ and is decreasing. From table 1, $A_E/A_M = .140$. Since $A_M = 37.9 \times 10^3$ km^2, and is the referenced max for this time, then $A_E = .140 \times A_M = .140 \times 37.9 \times 10^3 \text{ km}^2 = 5.31 \times 10^3 \text{ km}^2$.
13. Record A_E on the graph at the appropriate time, above A_C/A_M.
14. Compute r_V, rain volume, with the following relationships:

    a. $r_V = (1.30 \times 10^3 \text{ m}^3/\text{km}^2)\, A_E$, A_E increasing with time

    b. $r_V = (0.98 \times 10^3 \text{ m}^3/\text{km}^2)\, A_E$, A_E intermediate

    c. $r_V = (0.66 \times 10^3 \text{ m}^3/\text{km}^2)\, A_E$, A_E decreasing with time

    where r_V is rain volume per 5 min, in m^3, and A_E is echo area in km^2. Use the criteria of the next step to decide whether A_E is increasing, decreasing, or intermediate.
15. I. A_E is increasing if:

    A_C/A_M is increasing and $0 \leq A_C/A_M \leq 0.80$

    II. A_E is intermediate if:

    A_C/A_M is increasing and is the <u>first</u> point where

    $0.80 \leq A_C/A_M \leq 1.00$

    IMPORTANT: THERE WILL ALWAYS BE <u>ONLY</u> <u>ONE</u> INTERMEDIATE A_E PER RELATIVE MAX.

    III. A_E is decreasing if:

    a) A_C/A_M is decreasing
    OR

---

[26]Calculations can be made assuming the first or last point to be the relative max, but this is not recommended, since this will probably result in gross underestimates.

Table B1. Cloud area - echo area relationship

	incr.	decr.		incr.	decr.		incr.	decr.
A_C/A_M	A_E/A_M	A_E/A_M	A_C/A_M	A_E/A_M	A_E/A_M	A_C/A_M	A_E/A_M	A_E/A_M
0	.025	.000	0.40	.109	.030	0.80	.159	.093
0.01	.027	.000	0.41	.111	.030	0.81	.159	.098
0.02	.029	.001	0.42	.113	.031	0.82	.159	.100
0.03	.031	.002	0.43	.115	.033	0.83	.159	.104
0.04	.032	.003	0.44	.116	.034	0.84	.159	.106
0.05	.034	.003	0.45	.117	.035	0.85	.159	.108
0.06	.036	.004	0.46	.12	.036	0.86	.158	.110
0.07	.038	.004	0.47	.122	.037	0.87	.158	.113
0.08	.04	.005	0.48	.123	.038	0.88	.158	.117
0.09	.042	.006	0.49	.125	.039	0.89	.157	.119
0.10	.044	.007	0.50	.127	.040	0.90	.156	.120
0.11	.046	.007	0.51	.129	.041	0.91	.155	.124
0.12	.048	.008	0.52	.13	.043	0.92	.154	.126
0.13	.05	.008	0.53	.132	.044	0.93	.153	.129
0.14	.052	.009	0.54	.134	.045	0.94	.152	.131
0.15	.054	.009	0.55	.136	.046	0.95	.151	.134
0.16	.057	.010	0.56	.138	.048	0.96	.150	.135
0.17	.059	.011	0.57	.14	.050	0.97	.149	.138
0.18	.061	.012	0.58	.141	.051	0.98	.147	.140
0.19	.063	.013	0.59	.143	.052	0.99	.146	.143
0.20	.065	.013	0.60	.145	.054	1.00	.144	
0.21	.068	.014	0.61	.146	.055			
0.22	.07	.015	0.62	.147	.057			
0.23	.072	.016	0.63	.148	.059			
0.24	.074	.017	0.64	.15	.061			
0.25	.077	.017	0.65	.151	.063			
0.26	.08	.018	0.66	.152	.064			
0.27	.082	.019	0.67	.153	.067			
0.28	.084	.019	0.68	.154	.069			
0.29	.086	.020	0.69	.155	.070			
0.30	.086	.021	0.70	.156	.073			
0.31	.091	.021	0.71	.157	.075			
0.32	.093	.024	0.72	.158	.077			
0.33	.095	.024	0.73	.158	.079			
0.34	.097	.025	0.74	.159	.081			
0.35	.098	.025	0.75	.159	.084			
0.36	.102	.026	0.76	.159	.086			
0.37	.104	.027	0.77	.159	.088			
0.38	.105	.028	0.78	.159	.090			
0.39	.107	.029	0.79	.159	.092			

A_C = area of bright mass at 80 digital counts

A_M = relative maximum of bright mass at 80 digital counts.

A_E = area of echo (with 1 mm/hr threshold) that corresponds to bright masses A_C or A_M

b) A_C/A_M is increasing, <u>and</u> $0.80 \leq A_C/A_M \leq 1.00$ and it is not the intermediate point.

16. Compute the total R_V, that is, the rain volume over the interval of calculation Δt, by

$$R_V = (r_V)\ (\Delta t/5 \text{ min}).$$

The interval of calculation, Δt, is the time from this calculation to the next.[27] In figure B3, Δt for the rain volume at 1915 Z is 15 minutes, whereas Δt for 1930 Z is 5 minutes. Table B2 lists the computation time and time intervals used in figure B3.

17. Record R_V above A_E.
18. On the same graph plot the percentage of cloud area inside the area of interest versus time. Draw straight line segments between these points.
19. To calculate the rain volume inside the area of interest, multiply each recorded R_V by the corresponding fraction of the cloud (read from the graph constructed in step 18) inside this area. The start time of the R_V calculation must be the time for which the fraction of cloud is determined. Fractional cloud areas used in figure B3 are recorded in table B2 (next page).
20. Record the rain volume inside the target area above the rain volume of step 16.
21. Repeat steps 6 through 20 for each entity.

The above procedure utilizes brightness information from the 80 DC level only. If higher brightness levels are considered, the following steps are to be inserted into the procedure, or replace a previously given step.

2a. Trace the higher brightness contour(s).
2b. Determine the density(s) and digital count value(s) of any higher brightness level(s), as described in section D4.
3a. Note: Cloud entities are determined with the 80 DC contour only.
4a. Determine and record the area(s) of the higher brightness contour(s).
5a. Measure and record the brightness area(s) within the target.
6a. Plot the higher brightness area(s) versus time.
8a. Note: A_M is determined from the 80 DC contour only.
14. Compute either total entity rain volume or the target area rain volume with the following appropriate relationship:

(i) $r_V = I \times 10^3 \text{ m}^3/\text{km}^2 \times A_E \times \Sigma a_i b_i$

(This computes total rain from an entity)

(ii) $r_V = I \times 10^3 \text{ m}^3/\text{km}^2 \times A_E \times \Sigma a_i b_i f_i$

(This computes rain from an entity over a given target)

---

[27] The Δt for the last calculation should extend to the nearest convenient time, but intervals greater than 30 min are inadvisable.

Table B2. Calculation data for figure B3

Start Time (GMT)	Δt	Fraction in Target Area
1430	30	.03
1500	15	.05
1515	15	.07
1530	30	.09
1600	30	.19
1630	30	.31
1700	30	.355
1730	30	.37
1800	30	.39
1830	30	.35
1900	15	.33
1915	15	.32
1930	5	.31
1935	10	.31
1945	15	.315
2000	30	.30
2030	30	.255
2100	15	.225
2115	15	.22
2130	15	.22
2145*	15*	.21

*Calculation interval is to the nearest hour, 2200 Z.

where:

r_V = rain volume/5 min

$$I = \begin{cases} 1.30, & A_E \text{ increasing, as inferred from step 15.} \\ .98, & A_E \text{ intermediate, as inferred from step 15.} \\ .66, & A_E \text{ decreasing, as inferred from step 15.} \end{cases}$$

A_E = inferred echo area (km^2)

a_i = the fraction of an entity occupied by a higher brightness contour.

$$a_i = \frac{A_J - A_{J+1}}{A_{80}},$$

A_J and A_{J+1} being entity areas at two successive brightness countours. At a_i, $A_J = A_{80}$.

b_i = the empirically derived weighting factor for higher brightness contours. (see fig. 23 for specific values)

$$b_i = \frac{A_{80}}{A_J}$$

At b_i, $A_J = A_{80}$.

f_i = the fraction of each brightness level within the target;

$$f_i = \frac{A_{JT} - A_{(J+1)T}}{A_{JC} - A_{(J+1)C}}$$

The J's represent the brightness levels. A_T is entity area within the target and A_C is total entity area.

Assume that there are three contours, 80, 110 and 140 D.C. Then six areas have been measured: the total cloud entity area defined by the 80 DC threshold (A_{80} or A_{80C}); similar quantities for the two higher levels (A_{110} or A_{110C}, and A_{140} or A_{140C}); the area defined by the 80 DC threshold which lies inside the target (A_{80T}); and, again, similar quantities for the two higher levels (A_{110T} and A_{140T}). For a calculation point, where echo area has been inferred to be increasing, the computation of rain volume within a target area (equation (ii)) becomes:

$$r_V = (1.30 \times 10^3 \ \mathrm{m^3/km^2}) \times (A_E) \times$$

$$\left[\left(\frac{A_{80C} - A_{110C}}{A_{80C}} \right) (1) \left(\frac{A_{80T} - A_{110T}}{A_{80C} - A_{110C}} \right) + \right.$$

$$\left(\frac{A_{110C} - A_{140C}}{A_{80C}} \right) (2.1) \left(\frac{A_{110T} - A_{140T}}{A_{110C} - A_{140C}} \right) +$$

$$\left. \left(\frac{A_{140C}}{A_{80C}} \right) (4.0) \left(\frac{A_{140T}}{A_{140C}} \right) \right] .$$

It is suggested that no more than a total of three contours be used; two contours are generally sufficient.

15a. A_C and A_M refer to measurements made at 80 DC only.

18.
19. } If target rainfall is required these steps have been superseded by equation (ii) in the new step 14.

APPENDIX C: Empirical Normalization of ATS-3 Visible Imagery

C1. INTRODUCTION

As noted in the main text and in section A4.6, a standardization procedure is necessary in order to make comparisons among quantitative data from several photographic images. During the course of this research four normalization standards were tested using the ATS negatives with a densitometer as in Appendices A and B. With the idea of reducing experimental redundancy, the successes and failures of each are documented here. Note that these standards were designed to normalize images on which the brightest clouds were the objects of interest. Dark features, such as the sea surface for oceanographic studies, or middle density features such as fog, require their own standards.

C2. WEDGE NORMALIZATION

In the early stages of this work it was thought that the grey wedge at the edge of the ATS negative would be a useful standard. However, no constant, or even quasi-constant, density differences among the steps of the wedge could be found by which the images could be standardized. The wedge was computer generated during ground processing, and applied to the image downstream from the point of data reception. As such, the wedge could not adequately reflect data changes prior to its generation. Moreover, the inclusion of the wedge, begun in April 1971, was discontinued during 1972. We were never able to incorporate the ATS-3 computer generated wedge as a standard. However, the grey wedge on SMS-1 images has been successfully used for standardization of those images.

C3. SALT FLAT NORMALIZATION

Advised of the existence of the Bolivian salt flat, Salar de Uyuni (20°S, 67°W), by our collaborators at SSEC, (Martin and Suomi (1971)), we investigated its potentiality as a standard. Its several advantages became immediately apparent. It is a large, bright feature contained on all 3/4 and full disk ATS images. During the southern hemisphere winter, May through October, the salar is generally cloud free. (This period coincides with the convectively active period in south Florida.) And, the salt flat is longitudinally close to Florida. For these reasons the salt flat was very successfully employed throughout most of this study.

A graph of the time behavior of the salt flat is shown in figure C1. The ordinate is maximum salt flat intensity measured in density units (DU), while the abscissa is time (GMT). Superimposed on the eye-ball fit to the salt flat data is a curve of the cosine of the solar zenith angle constructed from the Smithsonian Meteorological Tables (1958). The shapes of the curves are similar, particularly between the hours of 1500 and 1800 Z. The salt flat densities of figure C1 have been corrected for DCU drift, and the solar zenith curve has been constructed so that its amplitude is identical to the maximum salt flat density.

It remains to show that the salt flat has a time behavior similar to that of convective clouds, to infer the validity of a salt flat correction.

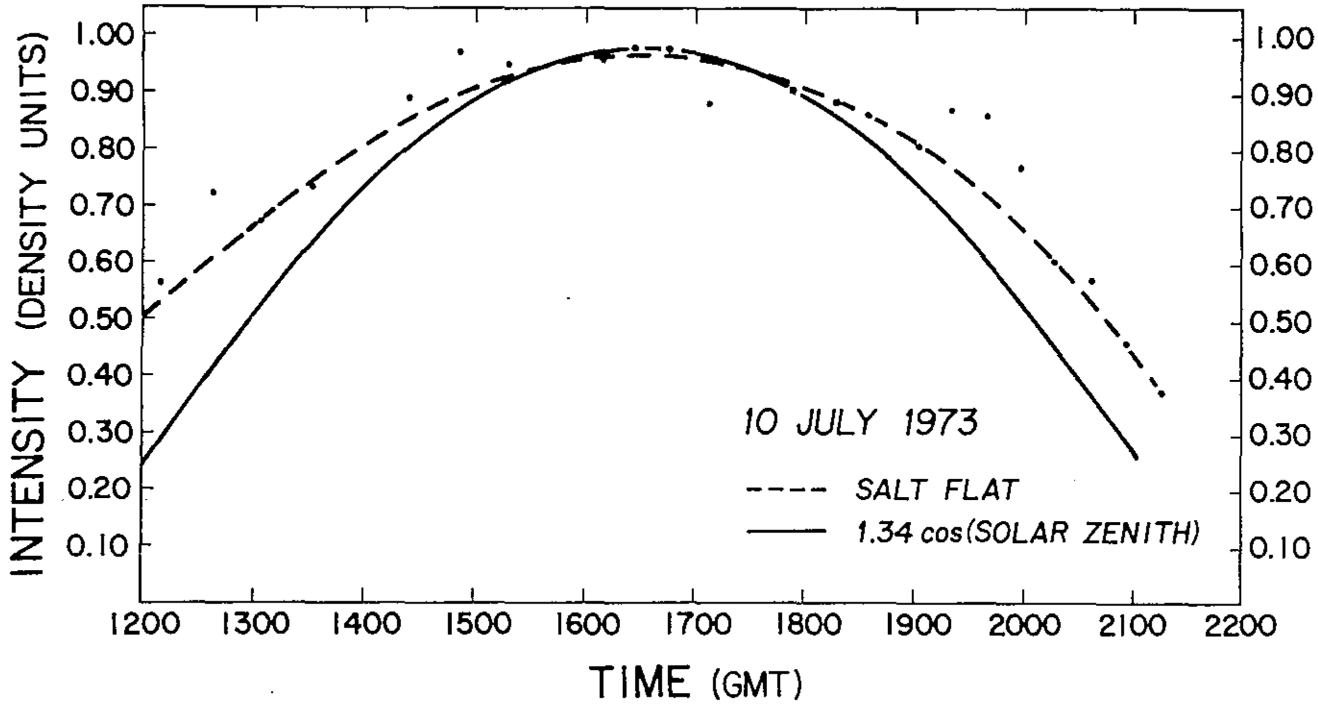

Figure C1. The time behavior of the Salar de Uyuni intensity. The dashed line is an eye-ball fit to the salar data (plotted data). A cosine of the solar zenith angle curve is shown for comparison.

Figure C2 presents a comparison of cloud intensity with the cosine of the solar zenith angle. To remove cloud intensity changes due to active growth, three masses in a persistent cloud system (tropical storm Agnes) were, investigated. In this figure the scatter is not really as great as shown because these cloud densities have not been corrected for DCU drift. The cosine curve has been constructed for a longitude and latitude intermediate to the three masses (18°N, 77°W). Again, as in figure C1, the maximum cloud densities of the three masses approximate very well the cosine function within the 1-1/2 hours either side of the relative max, and less well at earlier and later hours. Thus, the salt flat seems to exhibit a time-dependent intensity similar to that of clouds, at least to that of large systems, and should be a valid standard for cloud studies.

After making a few dozen salt flat readings at near local zenith, a standard salt flat value of 1.00 density units (DU) was chosen. This value is within the range of the salt flat measurements, is the value of the cosine when the solar zenith angle is zero, and makes correction factors easy to compute. (The correction factor is defined as 1.00 - (density of the salt flat). See section A4.6 for details.) With figure C1 it can readily be seen that this type of correction takes care of sun angle, as well as processing changes. The salt flat standard results in a relative, rather than an absolute, correction.

There were disadvantages with this standard. The high pressure cell over South America and the low in the south Atlantic, unfortuitously positioned, would cause clouds to funnel into South America directly across

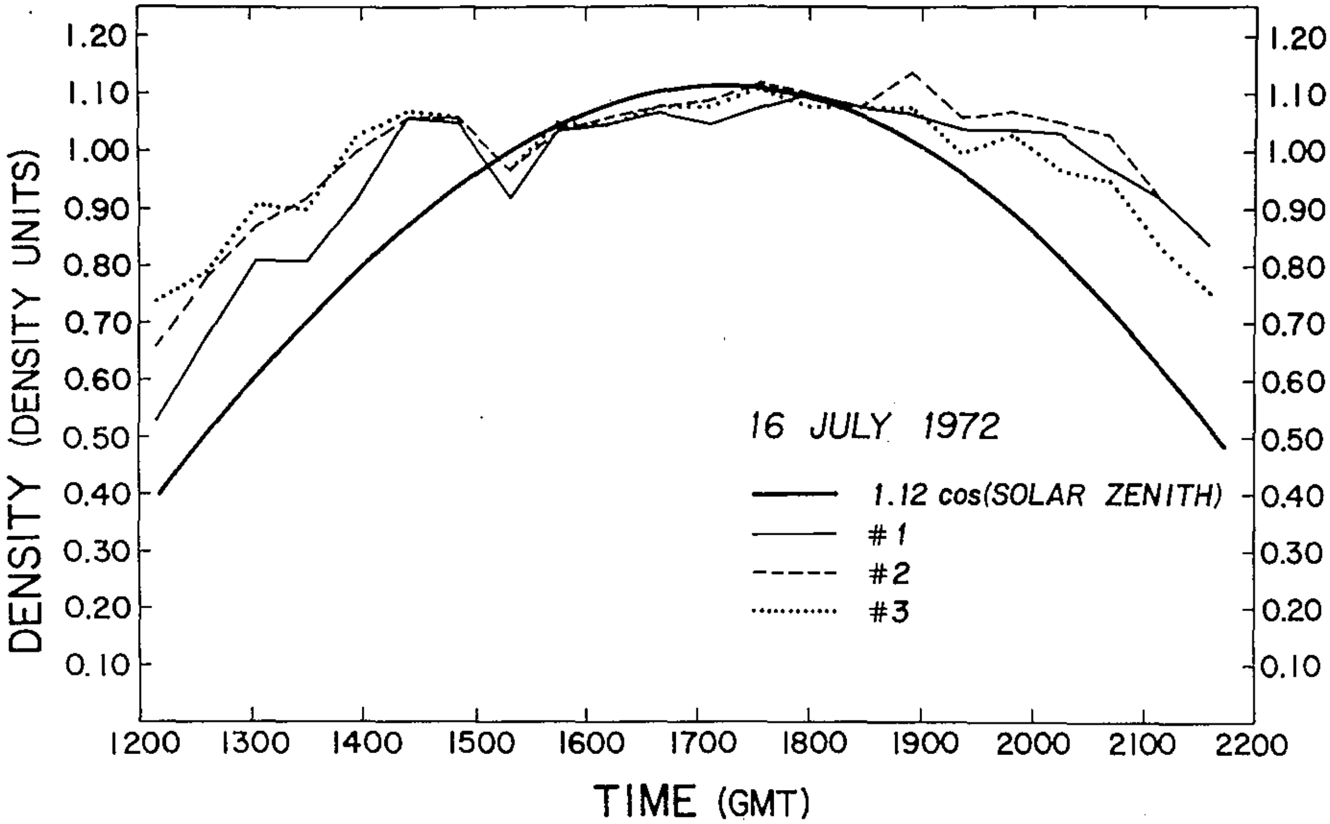

Figure C2. The time behavior of the intensity of three persistent masses in tropical storm Agnes. A cosine of the solar zenith angle is again shown for comparison.

the salar. Depending on the extent of the clouds, one or many pictures could not be normalized. If the salt flat did not appear on the image, or if there were a signal level change between Florida and the salt flat, again the data from that picture could not be normalized. Also, the salt flat normalization produced ridiculous results (a) at Florida, outside the hours of 1430-1930Z, and (b) for all hours, at locations significantly distant longitudinally from the salt flat.

During the early morning and late evening hours the normalizing difficulties are probably due to the approach of the sun's terminator to either the salt flat or the area of interest. Cloud shadows during these hours provide an additional complication which no simple normalization scheme can handle. At regions longitudinally distant from the salt flat, the sun angle difference between the location to be standardized and the salt flat becomes dominant and supersedes any processing changes. An attempt was made to eliminate the sun angle differences from the salar to the GATE B-scale area, centered at 10°N and 22°W. Of the several schemes tested, none produced satisfactory results, as judged by the capability of providing a reasonable-looking 80 DC threshold for the GATE area. This may be partly due to the differences in the convective activity between Florida and the B-scale area. The scheme which resulted in the best cutoff, although it failed badly with many images, was to subtract 0.29 DU from the salt flat correction factor c prior to the salt flat zenith, and to add 0.29 DU to c after salt flat zenith. The factor was arrived at from the longitudinal difference between the salt flat and the GATE area, $|67^o - 22^o| = 45^o$. Since the standard salt flat is 1.00 DU (= cos 0^o), then the longitudinal difference between the standard salt flat and the B-scale area is

$$\cos 0^o - \cos 45^o = 1 - .71 = 0.29$$

This scheme did not give satisfactory results and is not recommended.

C4. CLEAR OCEAN AND SPACE

The three disadvantages of the slat flat ennumerated above, plus the fact that the 1/2, 1, and 2 n mi resolution SMS visible sectors covering Florida do not contain the salar, revived the search for a standard. The dominant criterion became availability of the standard on any image from any satellite. For most studies, especially tropical and semi-tropical, clear ocean seemed to be an obvious choice. A close runner-up was outer space at the image corners. Yet, after finding both an average clear ocean density and an average space density, these standards resulted in cloud brightness thresholds which definitely included nonprecipitating cloud. The explanation of this error lies in the gamma curve for ATS images.

The gamma of an image controls the degree of contrast in the image, thus directly influencing the density or transmission value of every picture element. A gamma amplification curve, representative of the amplification applied to the ATS-3 data at the Wallops Island ground station, is shown in curve A of figure C3. This gamma is further modified by successive processing steps, such as computer processing at Suitland, Maryland (curve B) or recording on a Muirhead at the field station (gamma not shown). A more detailed discussion of the ATS gamma is presented in Woodley, Sancho and Miller (1972), and in Martin and Suomi (1971).

As can be seen, the resultant gamma[28] of figure C3 is composed of five linear segments. Clearly, a change in the slope or intercept of one section of the curve would not be indicative of the magnitude of a change in the slopes or intercepts of any of the other segments. Thus a correction factor inferred from clear ocean or space really cannot give a meaningful indication of the corresponding change in the bright cloud region.

C5. BRIGHTEST CLOUD STANDARD

Excluding clear ocean, only two other features appear on any and all images, namely land and clouds. There are potential problems with finding a representative density, regardless of terrain and vegetation, for a land standard, and most land densities are, again, not on the same segment of the

---

[28]Curve C is not the gamma of the ATS negatives used in this study, since it includes neither the Muirhead gamma, nor any of the amplifications appropriate to this study.

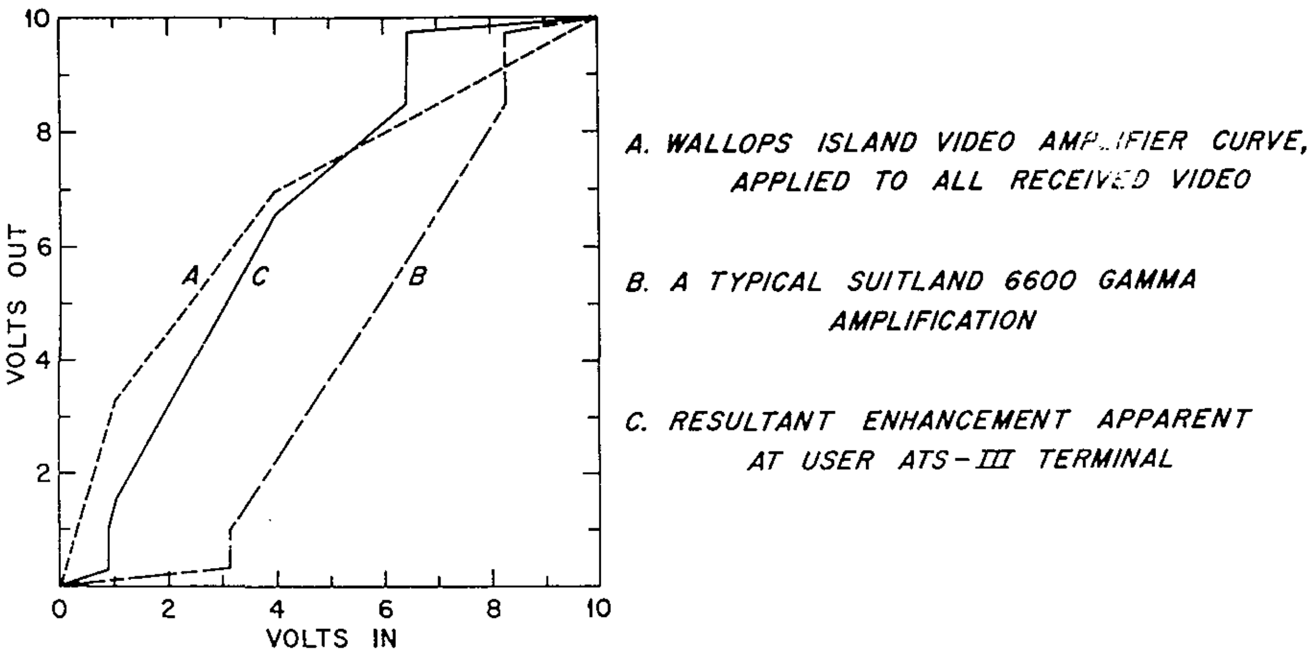

Figure C3. Typical amplification curves for ATS-3 data. As explained in the text these curves are not the actual gammas for the ATS data used.

gamma as cloud densities. Efforts were subsequently directed toward using a brightest cloud standard.

Measurements were made of the brightest clouds within 1 hour of longitude of the salt flat on the ATS-3 negatives closest in time to 1530Z (solar zenith at the salt flat). The brightest cloud and the salt flat densities were each recorded from 21 images in July and August, 1974. These brightest cloud densities were standardized to the salt flat, after being corrected for DCU drift, as described in section A4.6. The range of these 21 measurements was 1.04 to 1.16 DU, with an average of 1.09 DU and a standard deviation of 0.04 DU. The correction factor for the brightest cloud standard is $c_{CB} = 1.09 - \rho_{CB}$, where ρ_{CB} is the density of the brightest cloud, corrected for DCU drift (section A4.2).

The average difference between the correction factor c_{sf} as defined by the salt flat ($c_{sf} = 1.00 - \rho_{sf}$) and c_{CB} as defined by the brightest cloud is $\overline{\Delta c} = \overline{c_{sf} - c_{CB}} = +.02$ DU for 45 measurements within the hours of 1330 and 1930 Z. The range of these differences is −.07 to + .14 DU. The brightest cloud standard has been used to standardize most of the test cases of sections 4 through 6, and no problems have been detected up to the time of writing, even outside of the hours of 1430 and 1930Z, where the salt flat ceased to be useful.

APPENDIX D: Satellite Image Transfer Relationships and Applications

D1. STANDARD HEIGHT

The methodology described in this report was developed with ATS-3 full disk (10" x 10") negatives at a specified magnification, which was achieved with the settings given in table 1; this particular combination of satellite, image product, and instrument settings will be referred to as the Standard Height ATS-3, or simply, Standard Height. The use of the method with (1) a different image magnification, (2) a different ATS-3 product (e.g., a blow-up negative), (3) a different satellite, or (4) any combination of the above will require that transfer relationships involving the analysis height, satellite, and/or magnification under study be derived. The transfer relationship will provide the numerical value of any needed thresholds (e.g., 80 DC cloud area cutoff, or the value of the standard brightest cloud) for the magnification under analysis. The derivation of these kinds of relationships will be given in the next section, followed by a specific application.

D2. DERIVATION OF A TRANSFER RELATIONSHIP

The example given here is for a change in magnification of the ATS-3, 10" x 10" negative at a 33x magnification (Standard Height) to a 13x magnification. To effect a change in magnification, one must analyze a larger image area. The procedure, which follows, has also been applied for transfer relationships from:

a) Standard Height ATS-3 to SMS-1 visible, of any spatial resolution;
b) SMS-1 visible of one spatial resolution to SMS-1 visible of a second spatial resolution;
c) ATS-3 full disk negatives to ATS-3 blow-up negatives

Step c) is somewhat tricky and is the subject of the next section.

The basic transfer relationship procedure is the following:

1. With a calibrated DCU, record a number of density or transmission measurements at the Standard Height so that a meaningful range of measurements is acquired. That is, measure values over the expected range for the entity (e.g., clouds, under study).
2. Remeasure the <u>same</u> points at the second height.
3. Correct all measurements by the appropriate procedure(s); for example, densitometer drift (section A4.2) or picture processing (section A4.6).
4. Plot and/or fit a curve to the corrected pairs of measurements.

A sample plot and best fit line are shown in figure D1. The 33x magnification has been described elsewhere (table 1); the 13x magnification is achieved with a 55 m lens, no spacer, focused at ∿28 cm (as read off the lens), and ∿17.5 cm from the negative. At the greater magnification (lower camera height), the salt flat was thoroughly scanned to find its maximum brightness. This max brightness was recorded for several image times. The same procedure was again followed at the lesser magnification. All data were corrected for DCU drift by (A1). The corrected pairs of salt flat densities were fitted by the least squares method to a straight line.

The use made of this transfer function is the following. At the ∿33x magnification, two density values had been determined for the satellite rain methodology, 0.86 DU for a cloud brightness threshold, and 1.00 DU as a standard salt flat measurement. At the lesser magnification, the corresponding densities to be used are 0.81 DU and 0.95 DU, respectively.

D3. A TRICKY TRANSFER

As noted in section D2 , application c), a transfer relationship from the ATS-3 full disk negative, Standard Height to an ATS-3 blow-up negative at a nonstandard magnification, is a bit involved. Even though one is using an ATS-3 negative, the Standard Height settings will not result in the ATS-3, full disk, standard magnification, because the product is a blow-up. Therefore, the transfer procedure is modified as follows:

1. Knowing the latitude and longitude (λ_i, θ_i) of the center of the region to be analyzed, determine the amount of area (in degrees of latitude x degrees of longitude, or any convenient absolute units) viewed on the I^2S monitor at the Standard Height, with (λ_i, θ_i) at the center of the screen. This can be done with an ATS-3, 10" x 10" grid.
2. Again center the coordinates (λ_i, θ_i) on the monitor, but this time use the grid for the blow-up negative. Change the camera height and focus until the monitor scene shows the same area as in the previous step, or an area as similar in size as possible. This height and magnification is now the Standard Height for the blow-up.

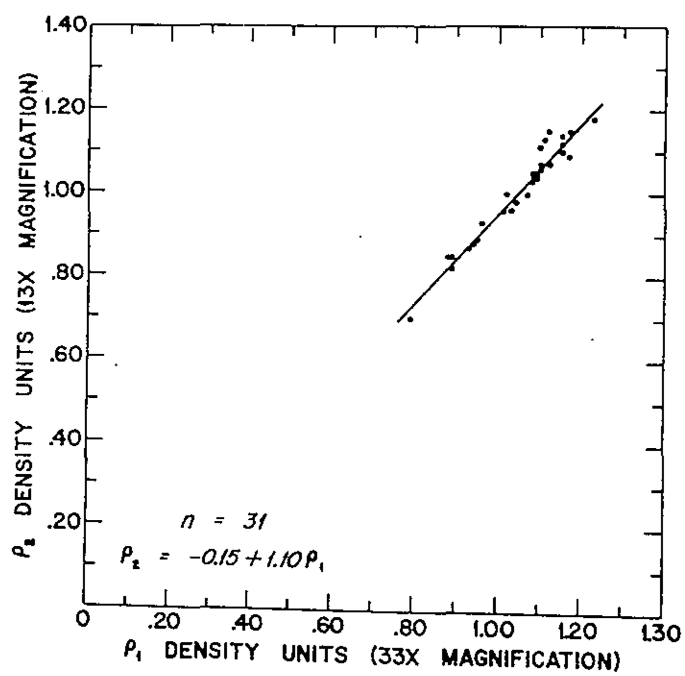

Figure D1. A sample transfer from the Standard Height (33x) to a 13x magnification.

3. Select the magnification at which the study of the blow-up is to be made.
4. Construct a transfer function as in figure D1, but take density readings between the Standard Height for the blow-up and the analysis magnification of step 3. The density unit value of any threshold derived at the Standard Height will be unchanged at the Standard Height for the blow-up. That is, 80 DC is 0.86 DU at both the Standard Height and at the Standard Height for the blow-up.

D4. DETERMINATION OF DIGITAL COUNT VALUES WITH THE TRANSFER RELATIONSHIPS

Assume one is estimating rainfall from hurricanes with the SMS-1, 1 km (1/2 n mi) resolution data at a nonstandard height. The standard brightest cloud and precipitation threshold are needed for this imagery. All magnification and satellite transfer relationships are derived according to the procedure of section D1 and, for reasons pertinent only to this example, the following transfer relationships exist from:

1. Standard Height ATS-3 to Standard Height SMS-1, 4 km (2 n mi), (fig. D2)
2. Standard Height SMS-1, 4 km to Standard Height SMS-1, 1 km (fig. D3) and
3. Standard Height SMS-1, 1 km to SMS-1, 1 km, height used for hurricane analysis (nonstandard height) (fig. D4).

The values of the required thresholds from the above three relationships are given in table D1. Notice that the transformation from SMS-1, 1 km Standard Height to SMS-1, 1 km, nonstandard height is one-to-one. This implies that the magnification change is not large enough to be detected by the DCU.

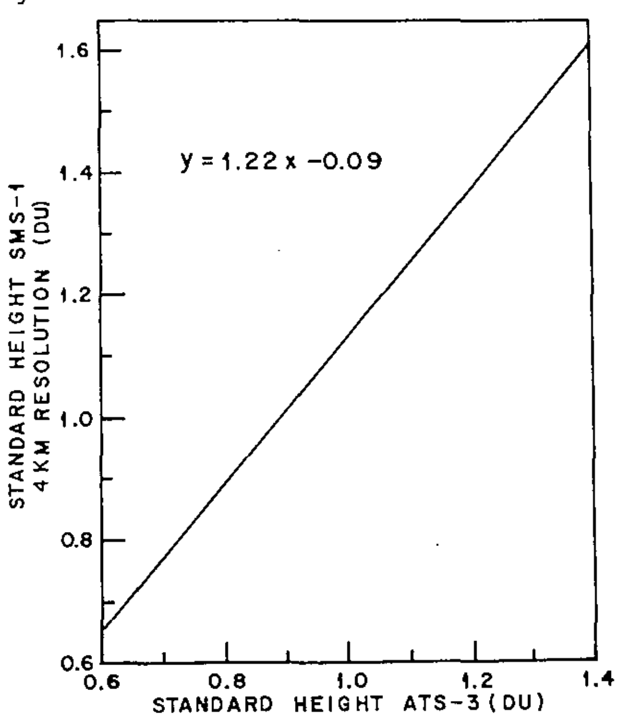

Figure D2. Transformation relationship from Standard Height ATS-3 to Standard Height SMS-1, 4-km resolution.

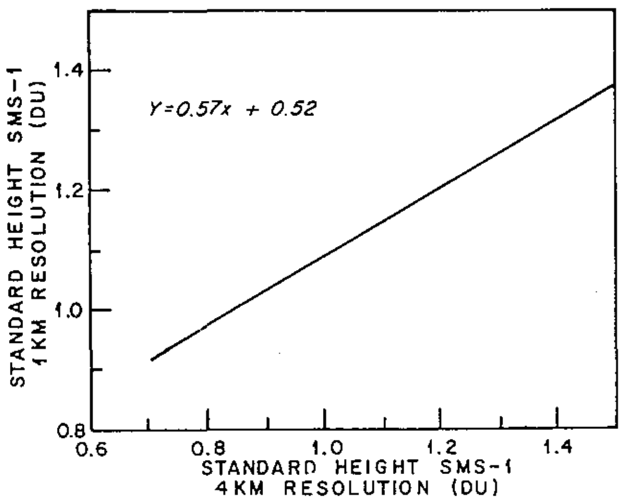

Figure D3. Transformation relationship from Standard Height SMS-1, 4-km resolution to Standard Height SMS-1, 1-km resolution.

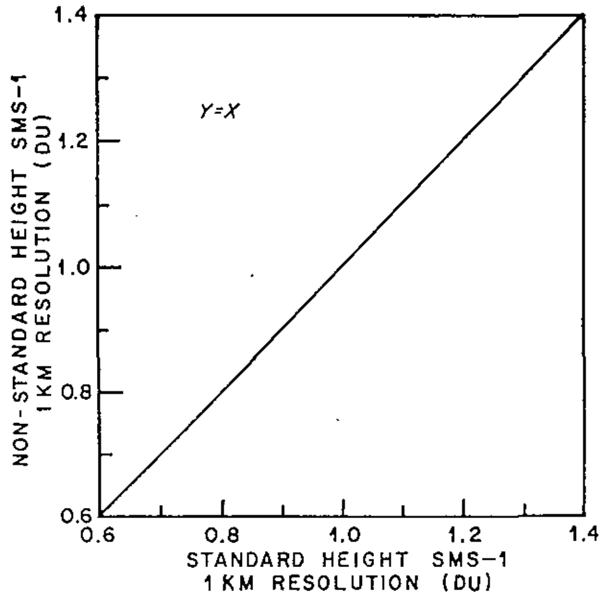

Figure D4. Transformation relationship from Standard Height SMS-1, 1-km resolution to a nonstandard height SMS-1, 1-km resolution. The relationship is one-to-one, as described in the text.

As the rainfall analysis proceeds, the following quantities are measured:

1. brightest cloud ("ideal") system: $\rho'_{CB} = 1.36$ DU
2. processing correction factor: $c = 1.22 - 1.36 = -0.14$ DU
3. 80 DC threshold ("ideal"): $k' = 1.07 - (-0.14) = 1.21$ DU
4. higher brightness contour ("ideal") system: $CD_2' = 1.30$ DU, where CD denotes Contour Division.

Table D1. Cutoff values (DU) for required transformations

	Digital Count value (DC)	Std. ht. ATS-3	Std. ht. SMS-1 4 km	Std. ht. SMS-1 1 km	Non-std. ht. SMS-1 1 km
k'	80	0.86	0.96	1.07	1.07
c	190	1.09	1.24	1.23	1.23

To calculate the hurricane rainfall using equations (4) or (6), the corresponding ATS-3 digital count value of this higher brightness contour must be ascertained. The first step in doing so is to arithmetically remove the correction for the processing of this particular image:

$$L' = c + CD'_2 = -0.14 + 1.30 = 1.16 \text{ DU} \qquad \text{(D1)}$$

This level value in the ideal system (L') has been derived at a nonstandard height with an SMS-1, 1-km negative. The three transfer functions described above must again be used to transform the L' value back to an ATS-3, Standard Height value. Then once the density value of this level at the Sandard Height ATS-3 is known, the digital count value can be determined. From figures D2 through D4 it can be seen that the values, shown in table D2, result.

The logic for (D1) and the subsequent transforms in table D2 can be understood by considering the following. For this nonstandard magnification, 80 DC corresponds to 1.07 DU. But in determining the 80 DC contour for this image, the correction factor c was subtracted:

$$k' = 1.07 - c,$$

and, the value of k' was calculated to be 1.21 DU. Now suppose a densitometer-corrected value of 1.21 DU were measured for one of the contours. What value would this correspond to in terms of the Standard Height ATS-3? According to (D1), $L' = c + CD'_1 = -0.14 + 1.21 = 1.07$ DU. And from table D1 it can be seen that 1.07 DU at this magnification is 0.86 DU at the Standard Height, which is 80 DC, as it should be.

Once the level value has been worked back through all the transfer relationships to the Standard Height ATS-3, the quantity can be expressed in terms of digital count through the relationship shown in figure 2, $D = \exp(1.070001 + 3.831051\,\rho)$, where ρ is the value in density units, and D in digital count. Therefore,

$$L' = 0.99 \text{ DU} = 129 \text{ DC}.$$

Table D2. Level value (DU) transformations

	Non-std. ht. SMS-1 1 km	Std. ht. SMS-1 1 km	Std. ht. SMS-1 4 km	Std. ht. ATS-3	Digital Count Value (DC)
L'	1.16	1.16	1.12	1.00	132

Thus the two levels that will be used for calculating rainfall from this hurricane will be:

$$i = 1,\ J = 80 \text{ DC}$$

and

$$i = 2,\ J = 129 \text{ DC}.$$

APPENDIX E: Daily Results from the Two Florida Tests

Daily results from the eight remaining FACE target tests and the five Florida larger area tests are shown in figures E1 through E8, and E9 through E13. Presentations are as described in the main text. It should be noted that groundtruth rainfall will not always be the same for the old and revised methods, because of differences in the time periods for which the old and revised calculations were made.

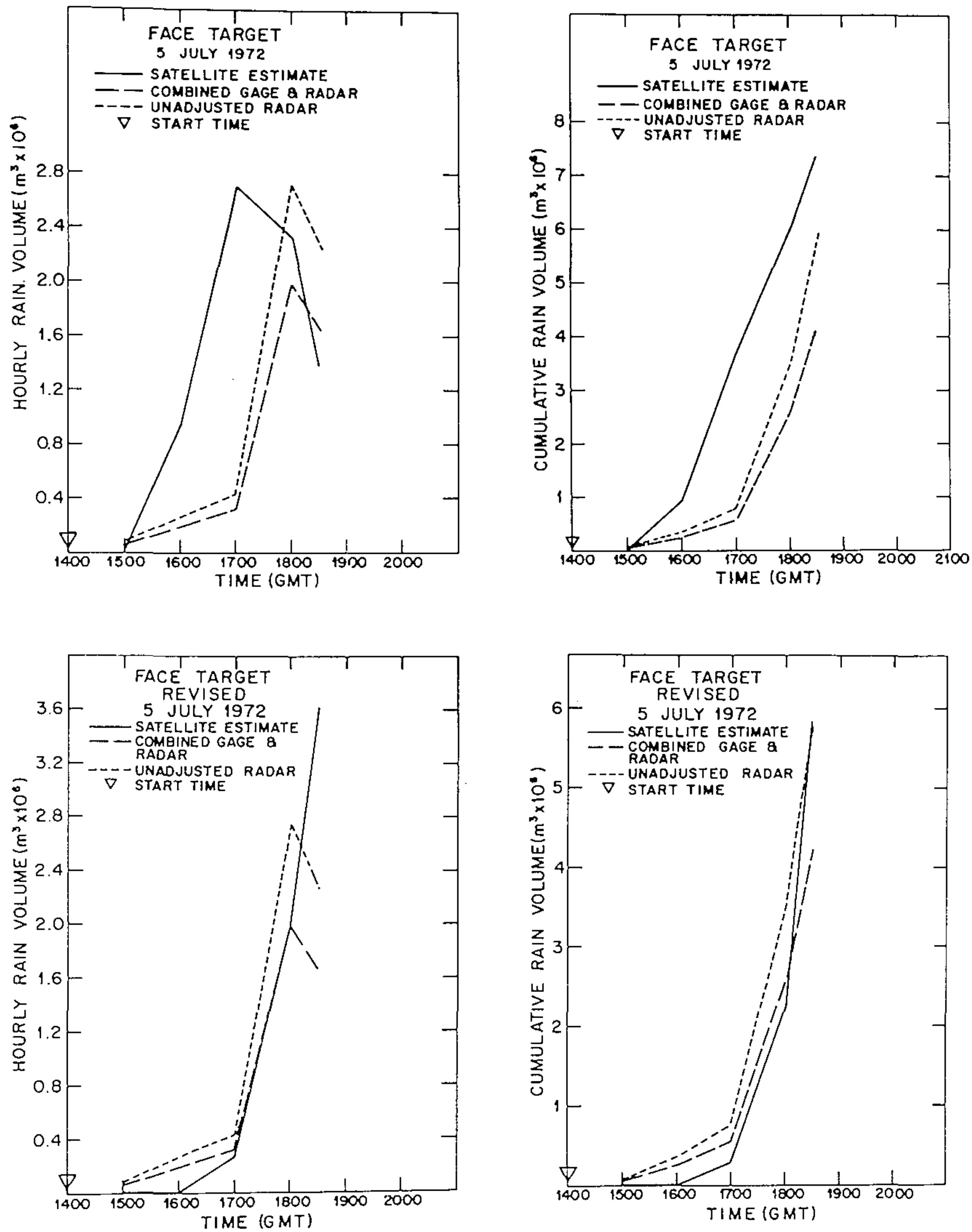

Figure E1. Hourly (left) and cumulative (right) FACE target rain results from the old (top) and revised (bottom) 80 DC tracings. Satellite estimates, and the gage-adjusted and unadjusted radar volumes are plotted. The calculation is for 5 July 1972.

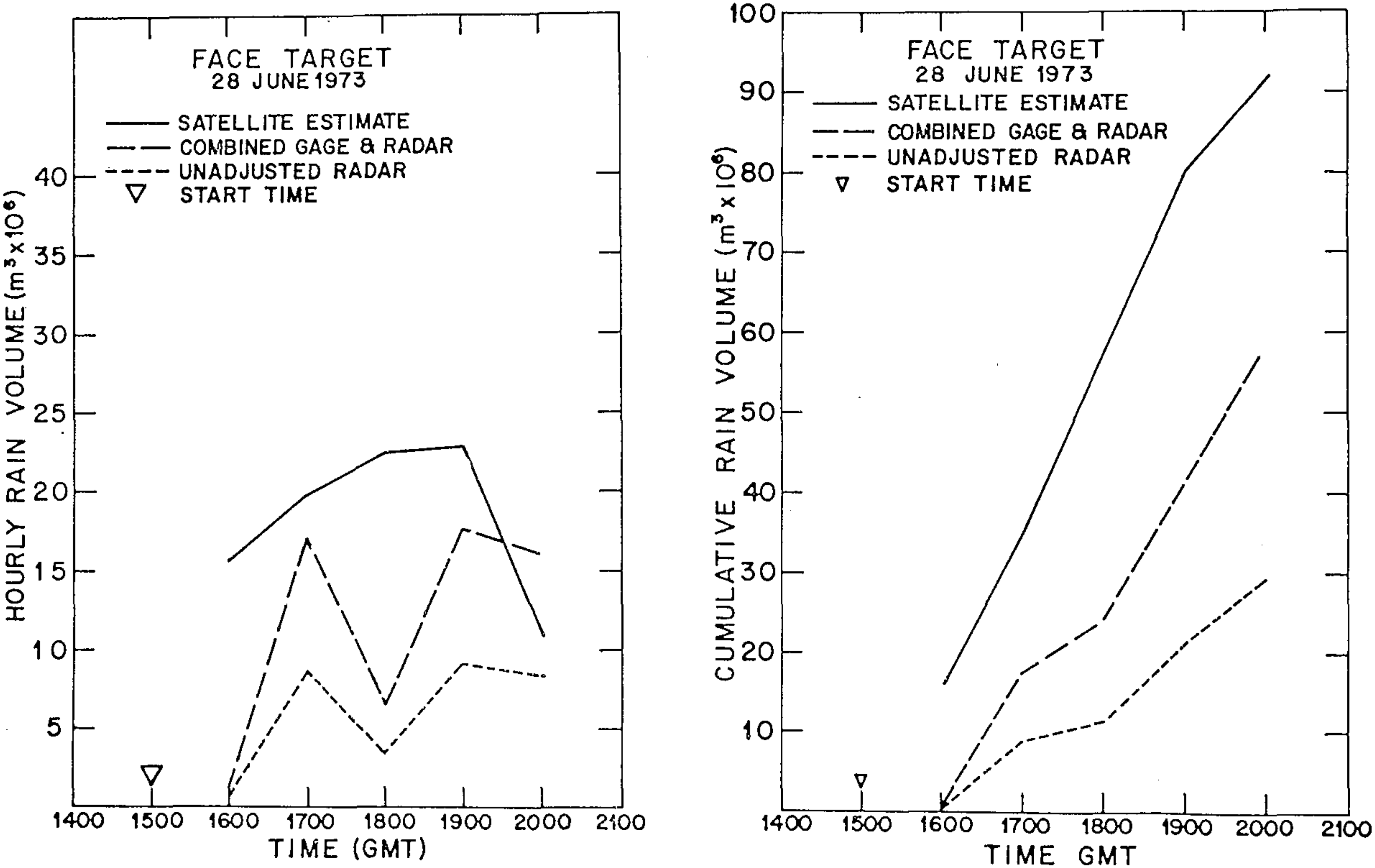

Figure E2. Hourly (left) and cumulative (right) FACE target rain results for the old 80 DC contour only. Satellite estimates, and the gage-adjusted and unadjusted radar volumes, are plotted. The calculation is for 28 June 1973.

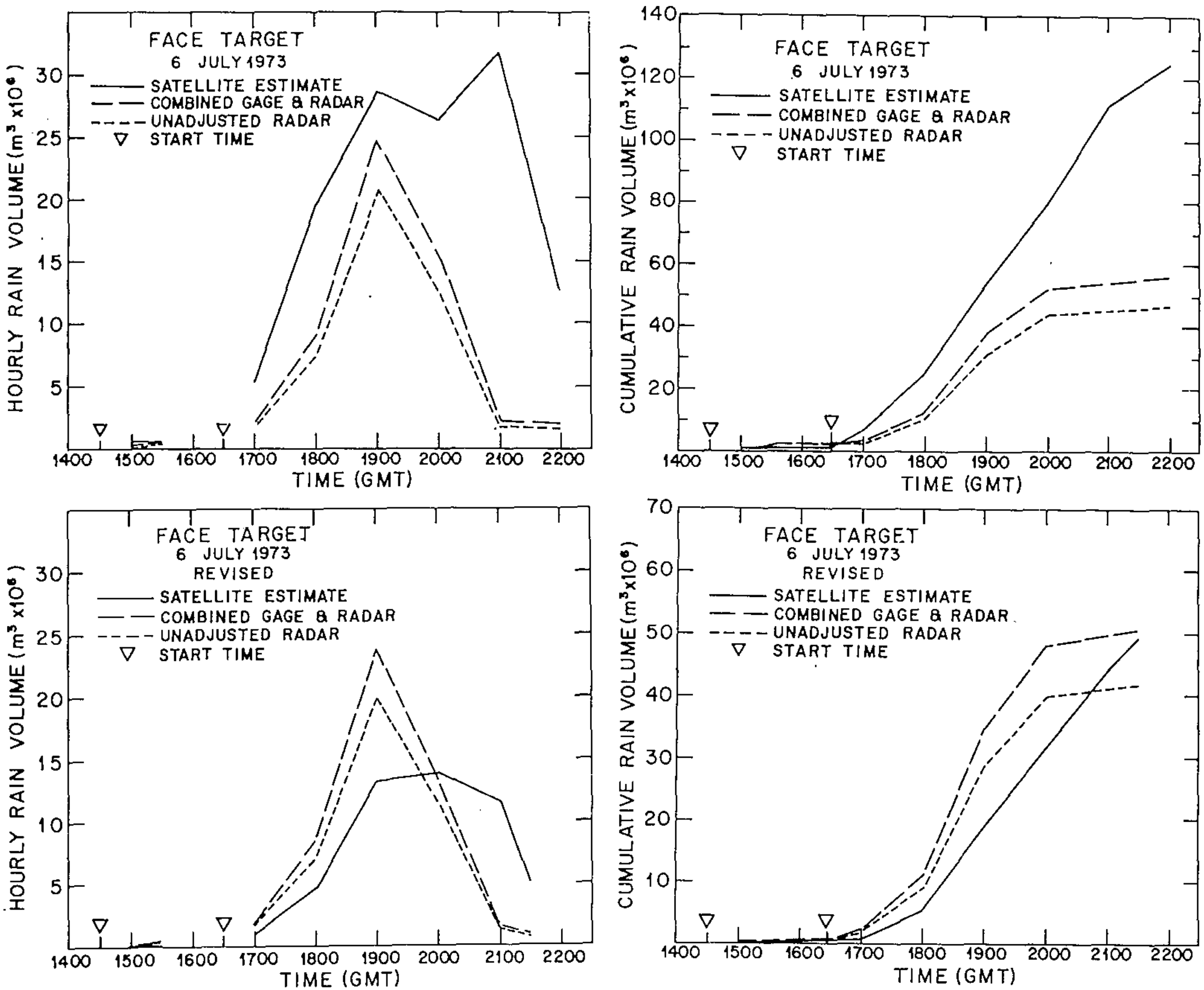

Figure E3. Same as figure E1, for 6 July 1973.

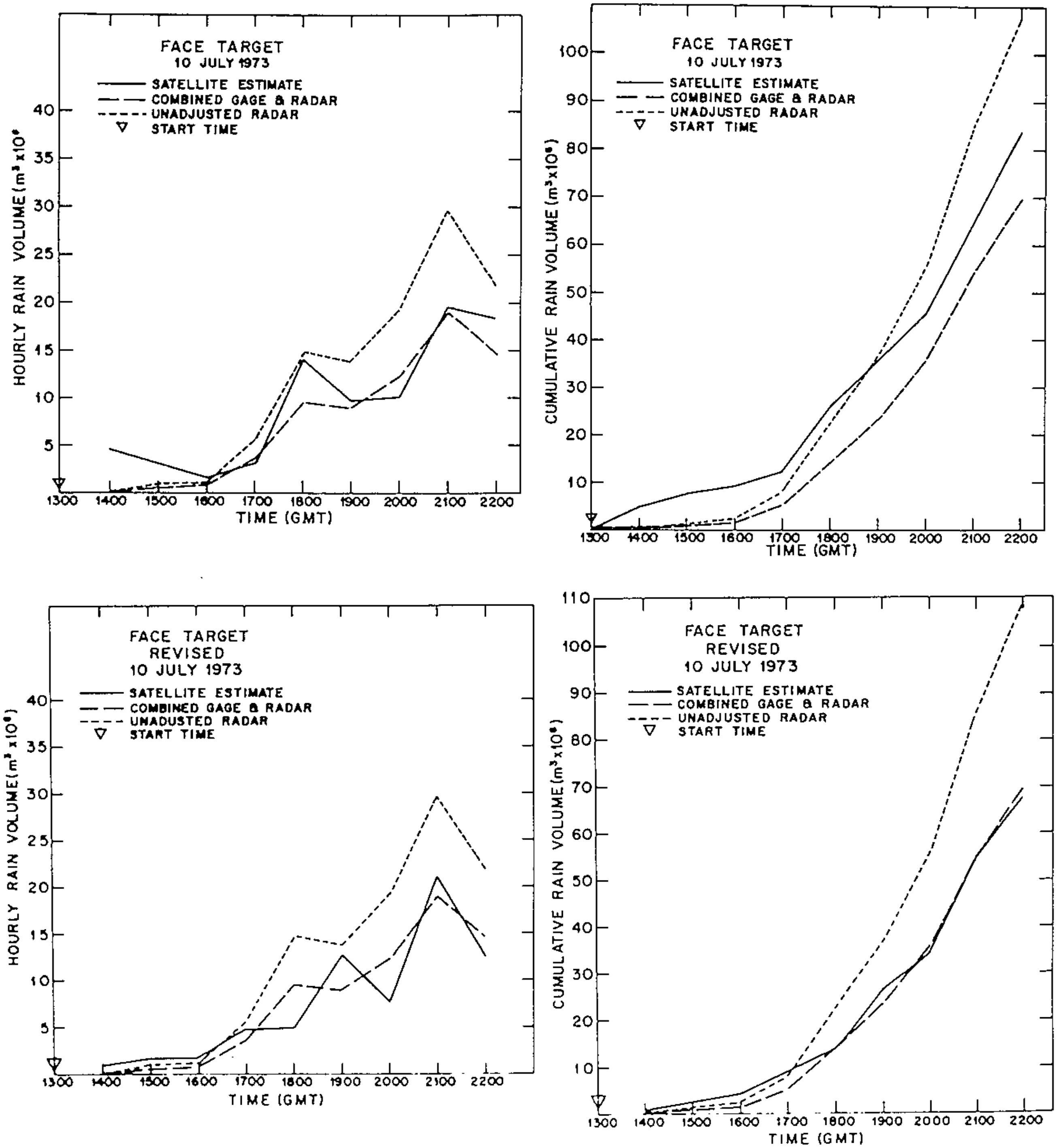

Figure E4. Same as figure E1, for 10 July 1973.

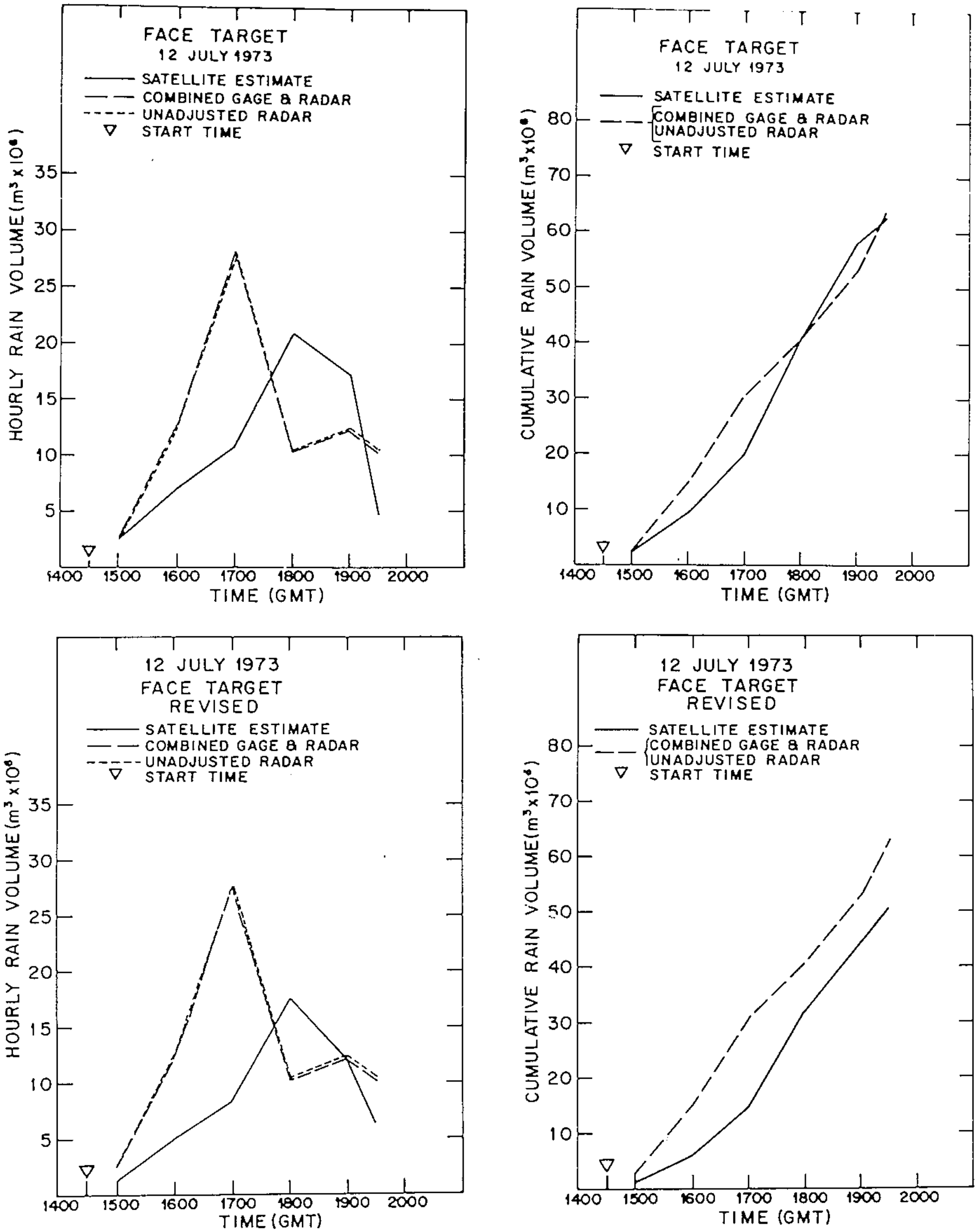

Figure E5. Same as figure E1, for 12 July 1973.

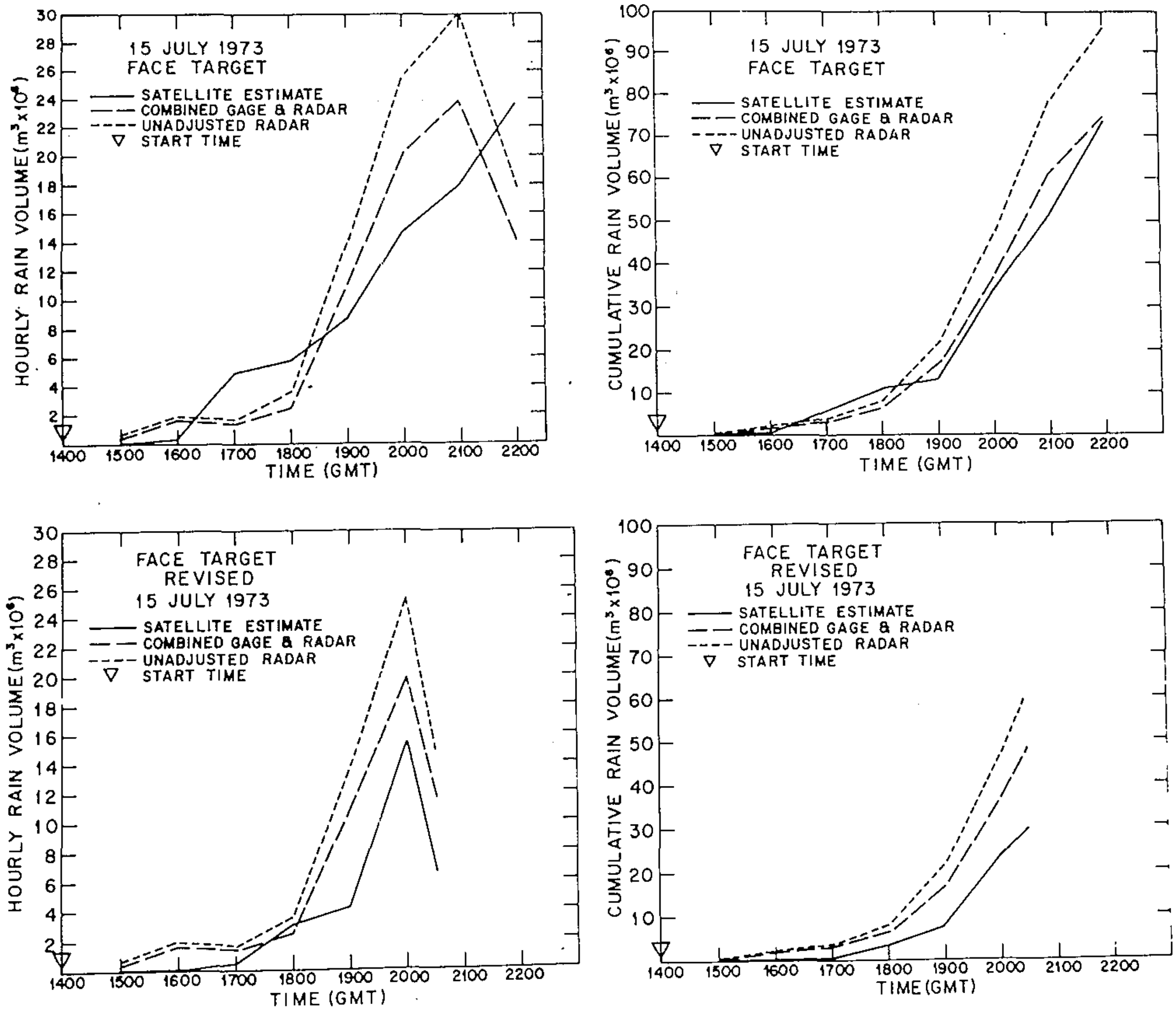

Figure E6. Same as figure E1, for 15 July 1973.

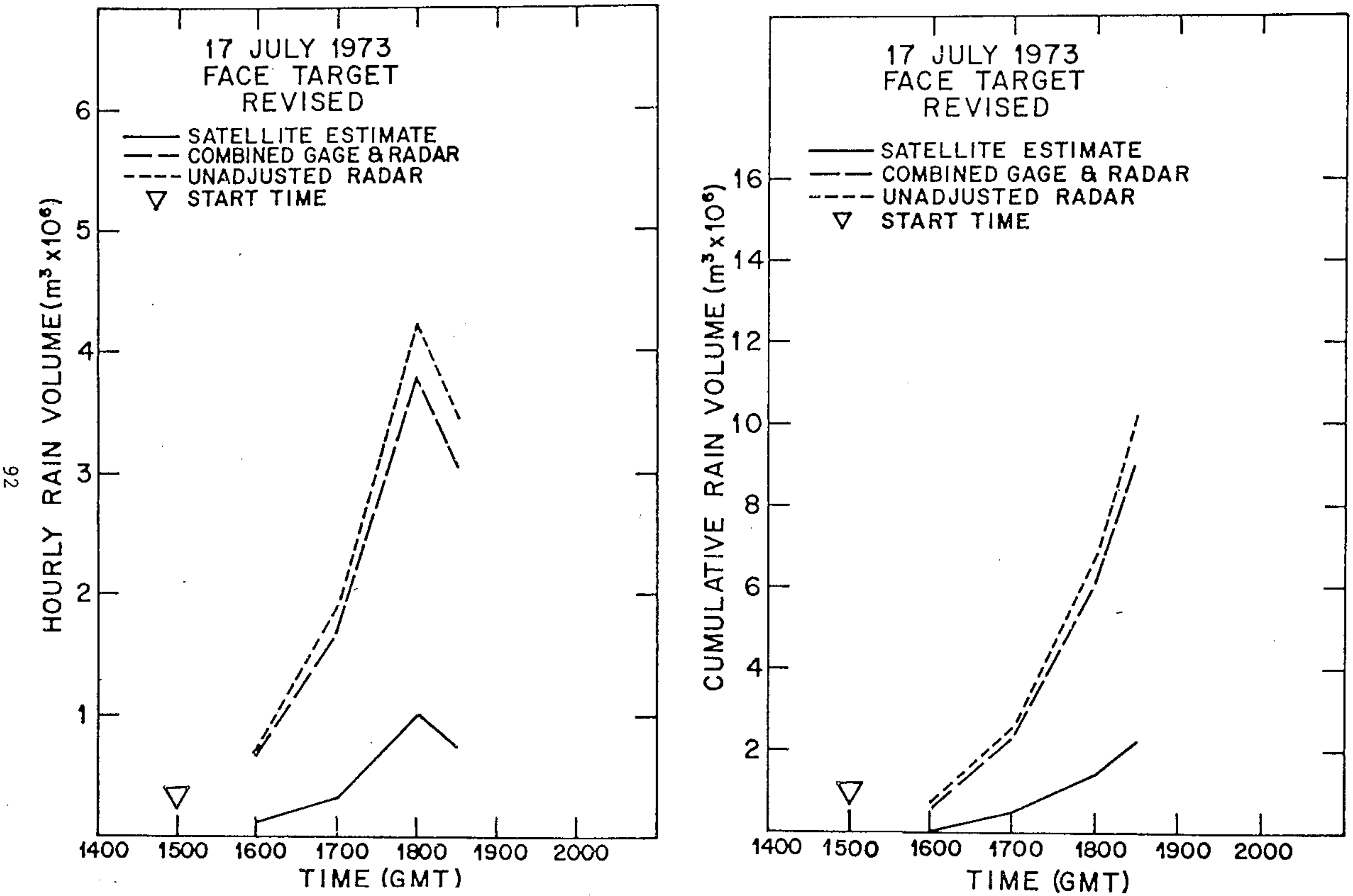

Figure E7. Hourly (left) and cumulative (right) FACE target rain results for the revised 80 DC contour only. Satellite estimates, and the gage-adjusted and unadjusted radar volumes are plotted. The calculation is for 17 July 1973.

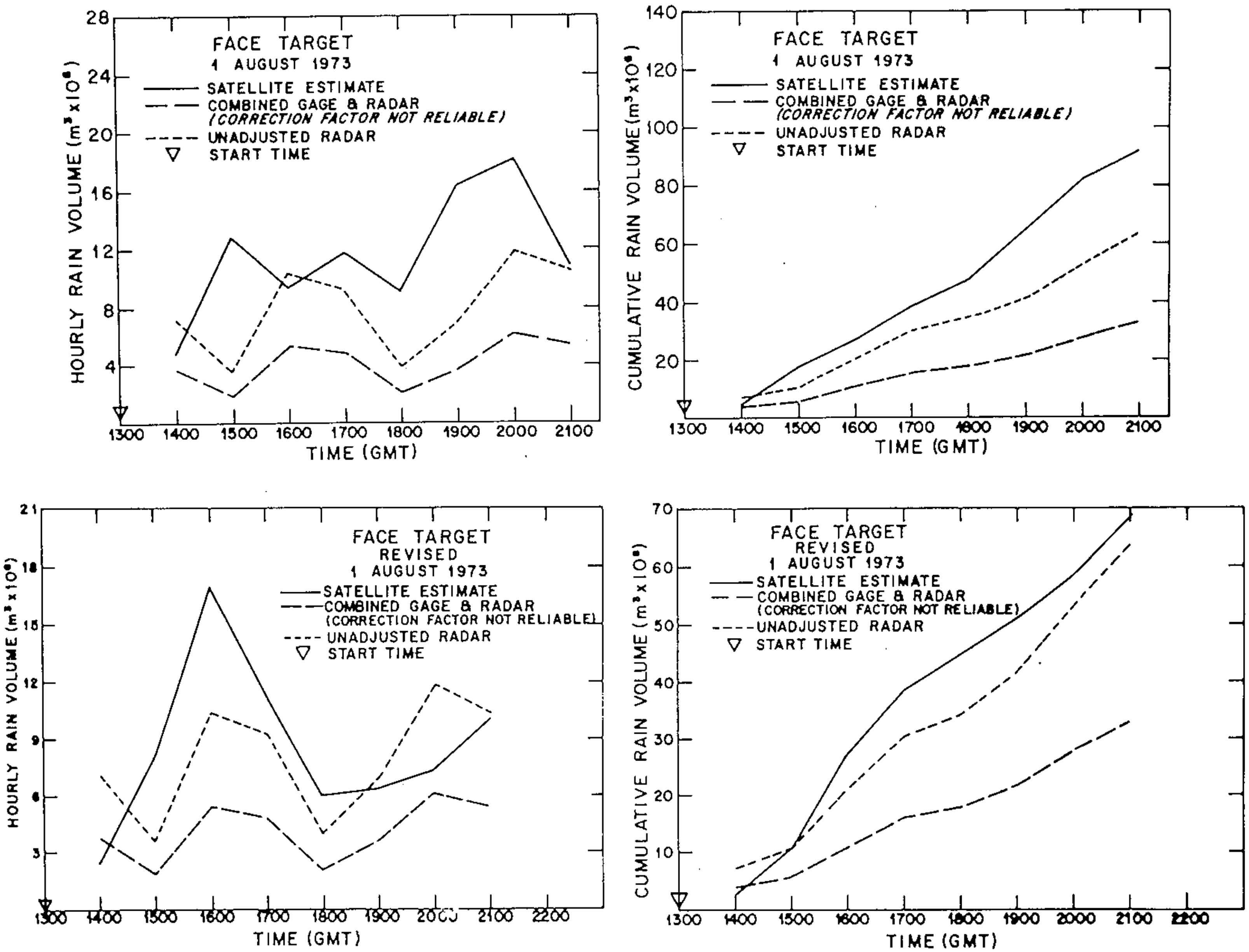

Figure E8. Same as figure E1, for 1 August 1973. The gage-adjusted rain volumes are unreliable because of small volumes and a limited number of gages.

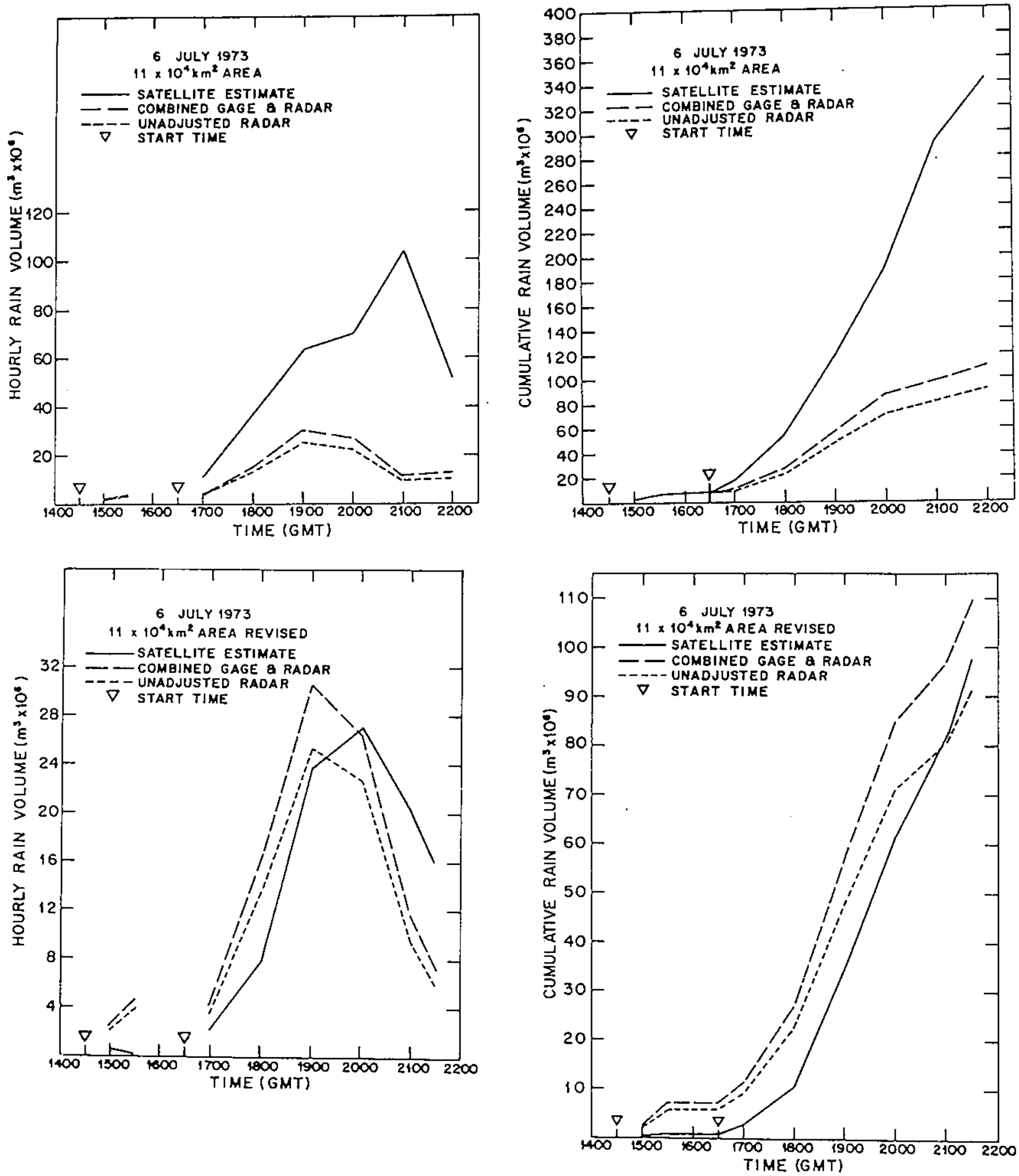

Figure E9. Hourly (left) and cumulative (right) rain results for the larger Florida area from the original (top) and revised (bottom) 80 DC tracings. Satellite estimates, along with the gage-adjusted and unadjusted radar volumes are plotted. The calculations are for 6 July 1973.

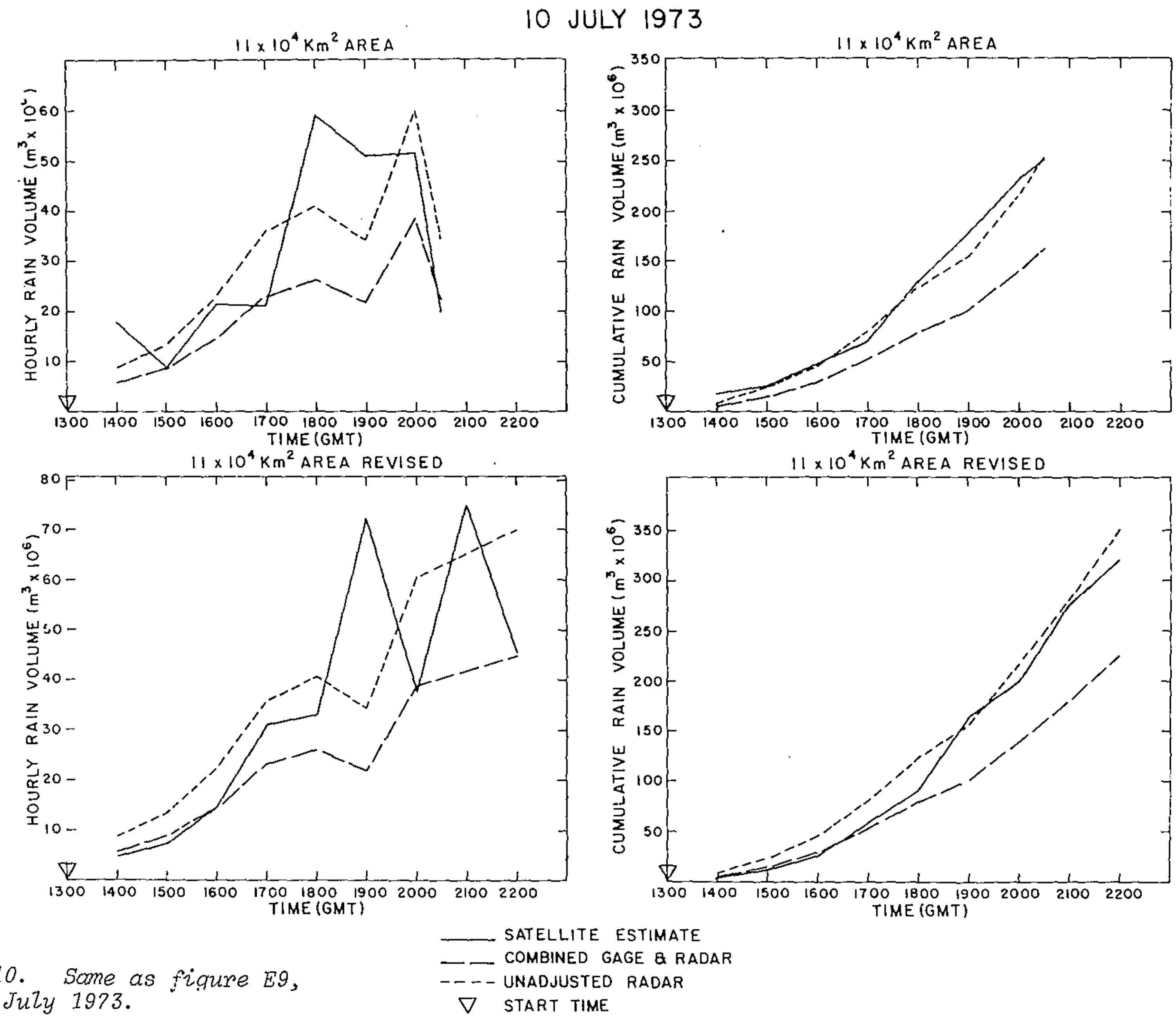

Figure E10. Same as figure E9, for 10 July 1973.

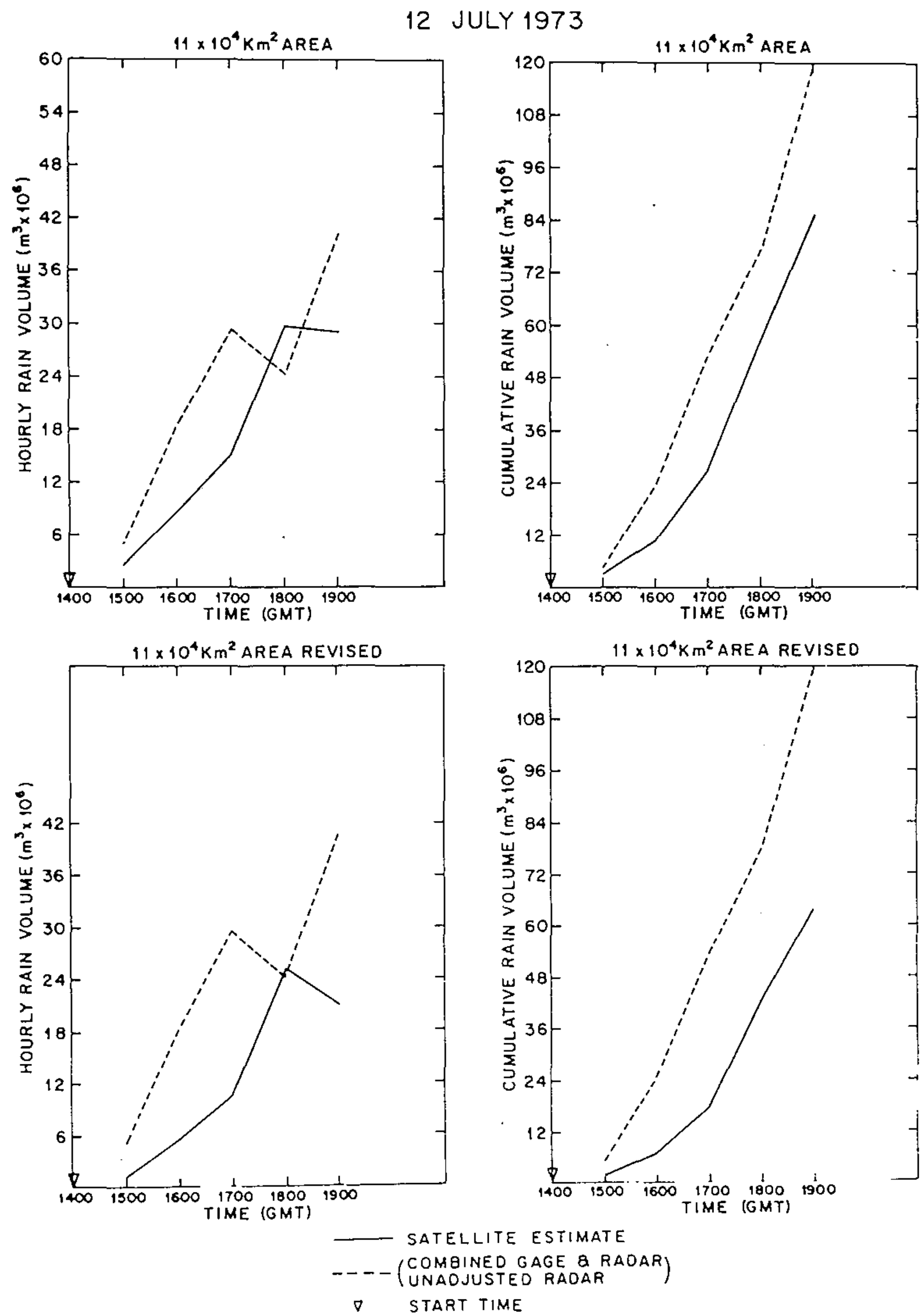

Figure E11. Same as figure E9, for 12 July 1973.

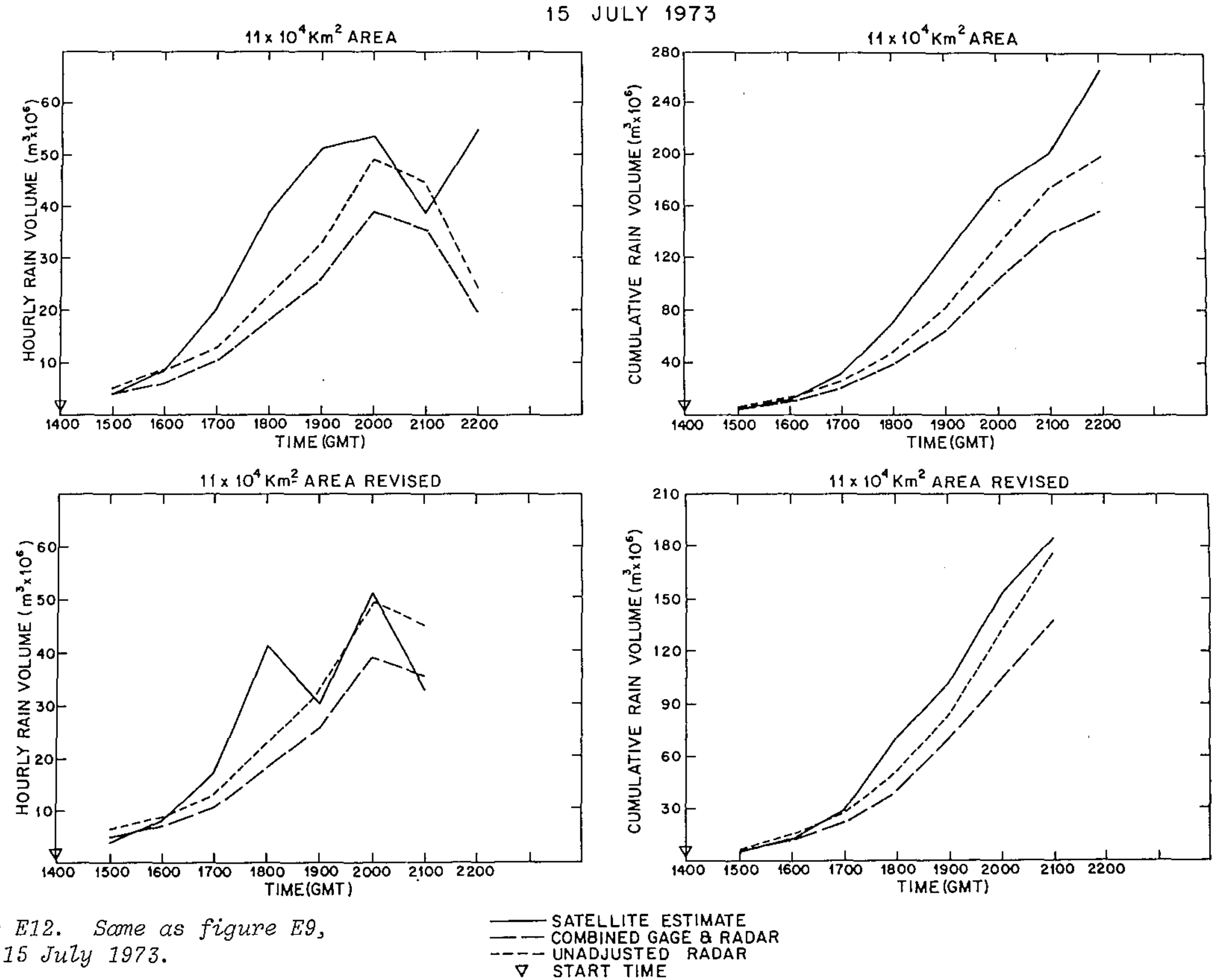

Figure E12. Same as figure E9, for 15 July 1973.

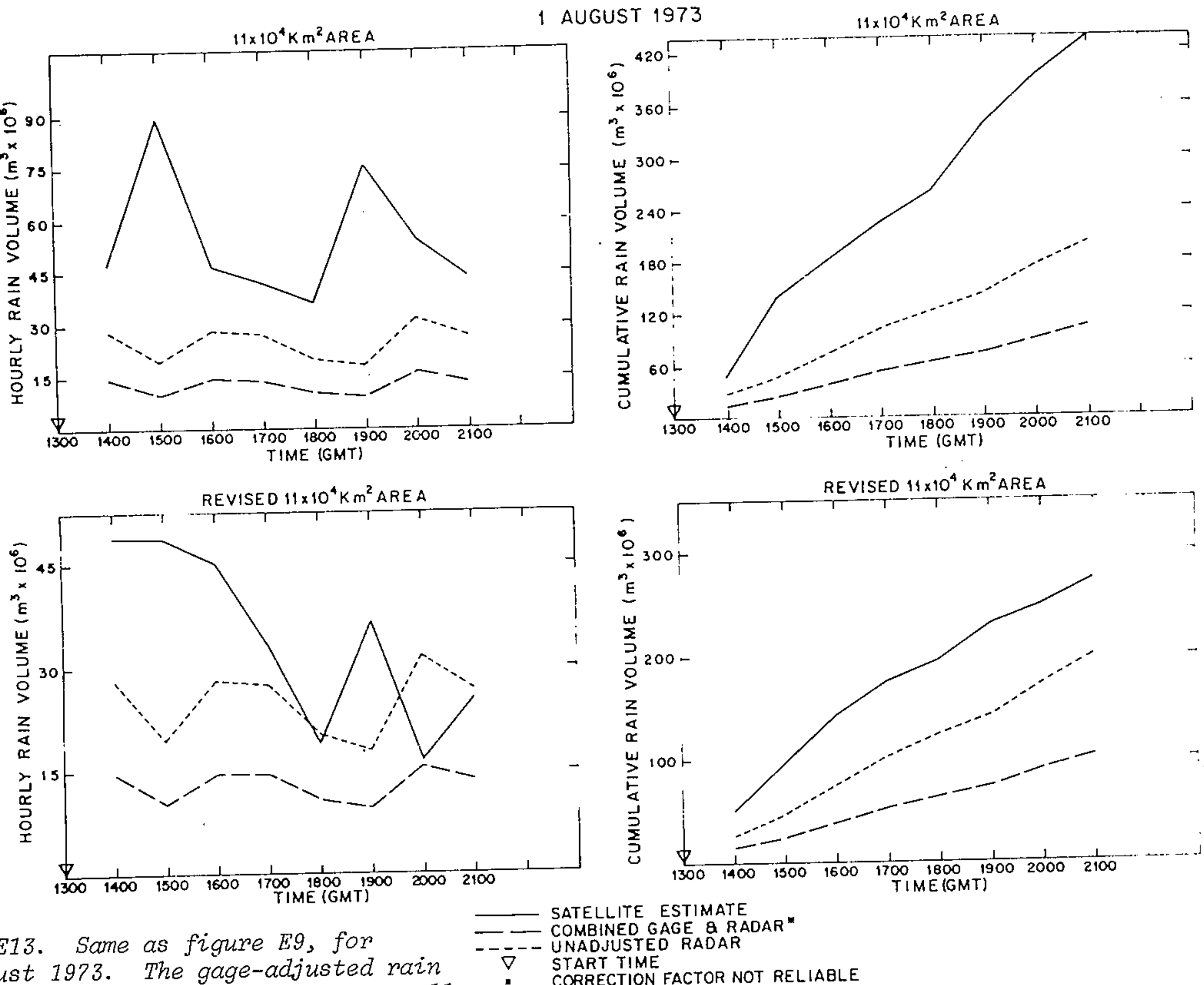

Figure E13. Same as figure E9, for 1 August 1973. The gage-adjusted rain volumes are unreliable because of small volumes and limited number of gages.

APPENDIX F: Radar Observations of Hurricanes Carmen and Fifi

Radar observations of hurricanes Carmen and Fifi of 1974 were analyzed to supplement the analyses of these storms made from satellite imagery (section 6.3). Both storms passed (fig. F1) within range of the S-band Mitsubichi model RC-32B radars in Kingston, Jamaica, and Belize, Belize that are part of the Caribbean Radar Network.

Basically, the radars are 10 cm with average transmitting powers of 0.5 Mw and beam widths of 1.9 degrees. Pulse widths are 0.5 μs and 4 μs in short and long pulse modes, respectively. Range normalization to 300 km and oxygen-attenuation corrections are normally applied. Linear and logarithmic outputs are available, as well as signal processing in an iso-echo unit. As a result, echoes can be displayed with or without range normalization from either output with manual or sequential automatic control of attenuation (in eight 5-db steps) of in any of three modes of multilevel contouring. The

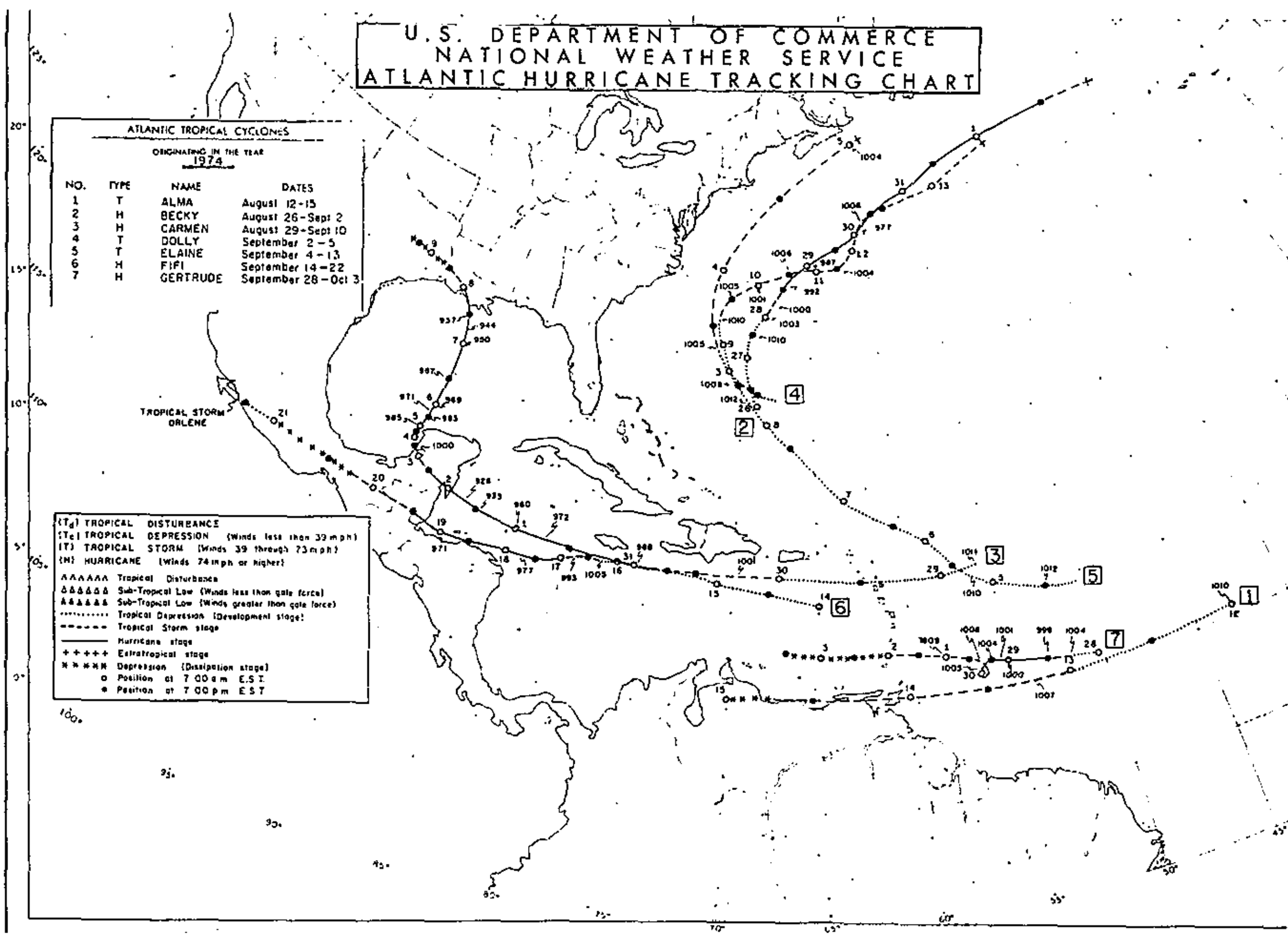

Figure F1. Tracks of Atlantic tropical cyclones during 1974. Note the paths of Carmen and Fifi.

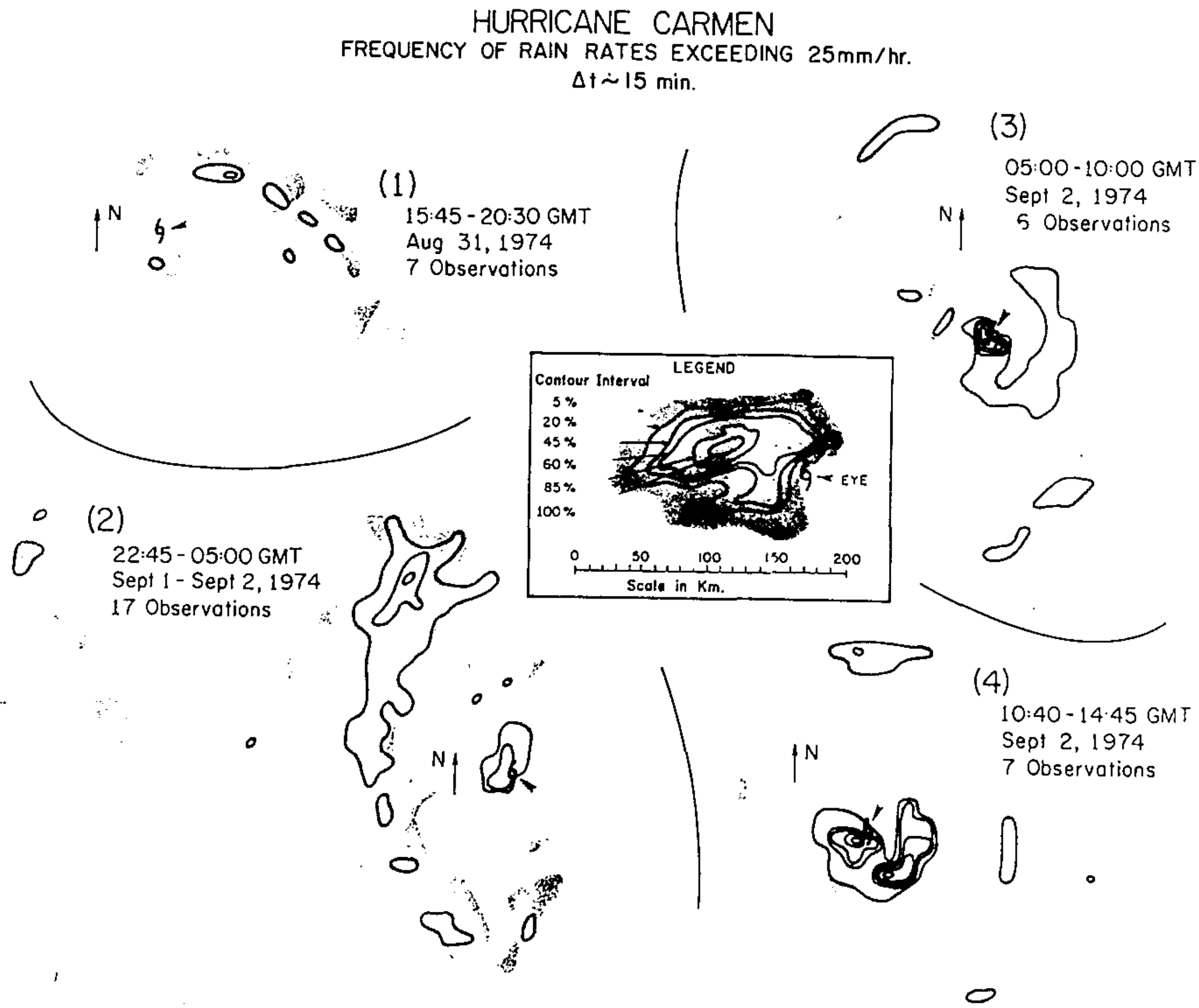

Figure F2. The frequency of echoes exceeding 25 mm/hr and surrounding the eye of hurricane Carmen for four selected periods, 31 August to 2 September 1974. Echo data were obtained from the Kingston, Jamaica and Belize, Belize radars.

mode used most in this study is "Grey Scale" whereby it is possible to represent the hurricane at five levels of brightness at 7.5 db intervals (grey, white, black, grey, white).

With the radar studies, we sought the patterning and evolution of the intense rain cores within the storm as a function of its intensity. Our initial intention was to calculate hurricane rainfall from the radar observations for comparison with the satellite inferences of storm rainfall. Upon second thought, this seemed inadvisable because of uncertainties in radar calibration as a function of time and our inability to check the radar estimates of rainfall against gages, as done with the Florida radar data. Consequently, we decided to examine the areal coverage of the most intense cores and their position in relation to the storm center by compositing the iso-echo presentation with respect to the storm center. Only echo intensities

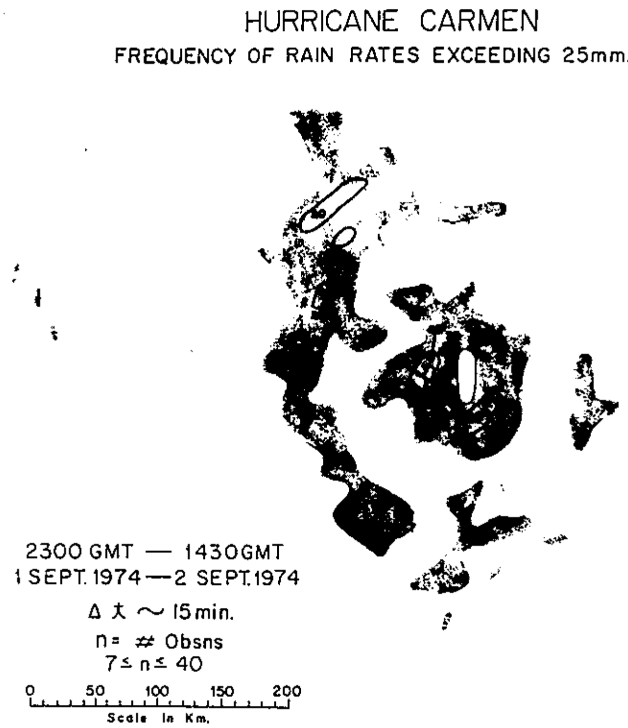

Figure F3. A composite analysis of echo frequency (exceeding 25 mm/hr) in hurricane Carmen from 2300 GMT on 1 September 1974 to 1430 GMT on 2 September 1974, using Kingston, Jamaica and Belize, Belize radar data.

corresponding to rainfall rates exceeding 25 mm/hr were composited.

The frequency of the spatial distribution of the intense rain cores in Carmen is shown in figure F2 for four periods and in figure F3 for 2245 GMT on 1 September to 1445 GMT on 2 September 1974. The rain core composite, when the storm was near Jamaica, is shown in panel 1 of figure F2. The core frequencies do not exceed 50 percent during this period and they are displaced some distance from the storm center. Carmen was next seen by the Belize radar (panel 2) about 24 hours later. Its pressure had decreased from 985 mb late on 31 August to near 950 mb by late in the day on 1 September. Storm organization changed accordingly, with a prominent band of high-core frequencies on the west side of the storm and near the eye. The transformations in storm organization as it deepened further to below 930 mb is shown in panels 3 and 4. Core frequencies continued to increase around the storm center with the exception of the right rear quadrant, but core frequencies decreased elsewhere in the storm. The deficit of strong cores in the right rear quadrant was apparently caused by strong divergence in this region. Eye diameter during the intensification process is shown in figure F4. A distinct double eye structure was present late on 1 September and early on 2 September.

Only a small fraction of Carmen's raining area was actually occupied by intense cores. The mean coverage of cores was only 2.5 percent of the raining area during the period this storm was observed by the Belize radar. If one assumes that these cores are indicative of strong convective regions,

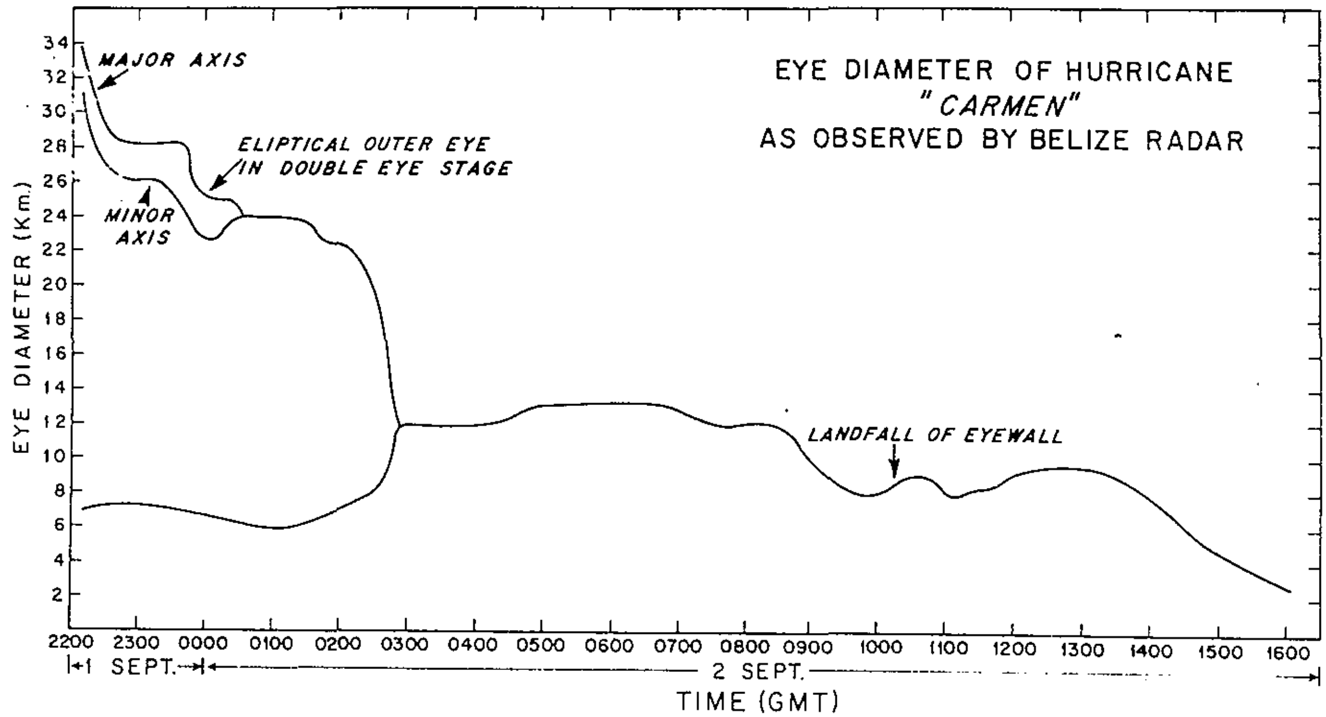

Figure F4. The eye diameter of hurricane Carmen as observed by Belize radars, 1-2 September 1974. Note the double eye.

then only a small fraction of this rather strong hurricane contains intense convection. This agrees very well with the work of Malkus, Ronne and Chaffee (1961).

The composite of the intense rain cores in Hurricane Fifi are shown in figure F5 from 0600 to 1500 GMT on 19 September 1974 as the storm tracked a westward course south of Belize (figure F1). Although Fifi passed near Jamaica several days earlier, the radar observation from Kingston could not be used for our purposes. The coverage of intense cores decreased during the period it was observed from Belize, particularly so in the east-west band to its north. Unlike Carmen, this band is as convectively strong as the region near the eyewall. The stronger convection near the eye of Fifi is also at a greater radius and has a lesser frequency than Carmen. The frequency and organization of the rain cores alone make it obvious Carmen was the stronger of the two storms.

The composite for Fifi for the entire period of observation is presented in figure F6. The band to the north of the eye and the convective region around the eye are the prominent features. Comparison of this composite with the overall composite for Carmen reveals higher frequencies of intense rainfall at lesser radii in Carmen than in Fifi. Only 0.5 percent of the area of rainfall in Fifi was covered by intense cores as compared to 2.5 percent for Carmen. Consequently, the rain was somewhat heavier in Carmen than in Fifi.

The radar analysis supports the findings in section 6.3 obtained with the method to estimate rainfall from satellite imagery. Both suggest that

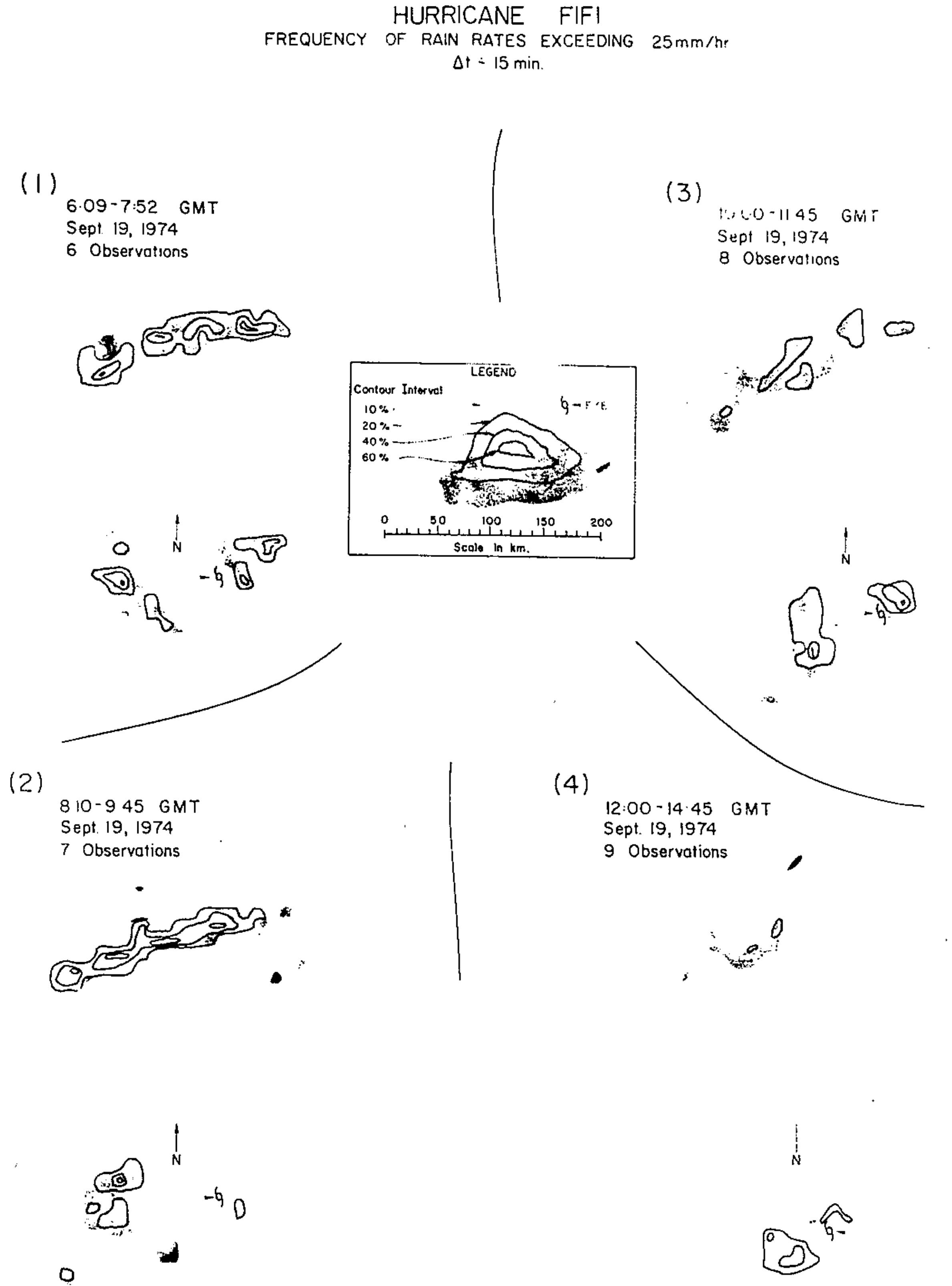

Figure F5. The frequency of echoes exceeding 25 mm/hr and surrounding the eye of hurricane Fifi for four selected periods on 19 September 1974. Echo data were obtained from the Belize, Belize radar.

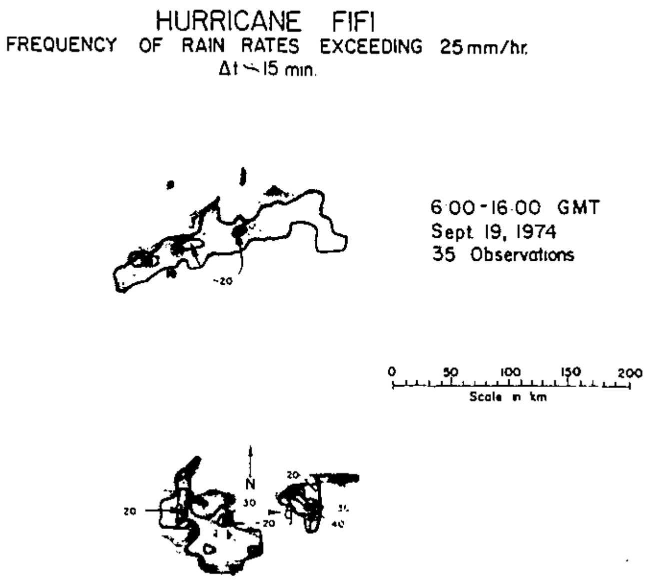

Figure F6. A composite analysis of echo frequency (exceeding 25 mm/hr) in hurricane Fifi, 0600 GMT to 1600 GMT on 19 September 1974, using Belize radar data.

the rain intensity in Carmen was somewhat greater than in Fifi, even though Fifi had the greater flood potential by virtue of its greater size. This agreement gives greater confidence in the method to estimate rainfall from satellite imagery.

Acknowledgment: Thomas Rascon and Matthew Bamberg ably carried out the analyses of this section.

Appendix G: Computer Automation of the Satellite Rain Estimation

The foregoing document presents a methodology that performs remarkably well for Florida and in hurricanes (although wholesale applicability to other tropical weather regimes has not been optimally tested) and that appears, after reading, to be a very complex and perhaps even mystifying technique. This complexity, as detailed below, arises from the product and the analysis tools available at the NHEML. Much simplification could be attained were the digital data to be used. Lacking an interactive display and computational device of the McIDAS[27] or IDAMS[28] variety, a scheme for computer automation of the method is also outlined.

The essence of the satellite rain estimation method is given in section 3.4. Quite simply, there are two approximately linear relationships, which are applied to a data set stratified by the growth trends of cloud expansion and decay. However, a large portion of the report describes manipulations that are necessary when hard copy satellite products are to be analyzed with a scanning densitometer. Thus, Appendix A is devoted to the operation of the particular false-color scanning densitometer employed, with several useful procedures included. The machinations of Appendix D arise primarily because the method's component relationships have been derived and first applied to a hard copy product of a particular geostationary satellite, which is analyzed at a specified magnification. The utilization of the new geostationary satellites, of different product formats, of different magnifications, or of any combination of these three calls for the techniques of the appendix. Lastly, the construct of "old" versus "revised" cloud areas and, consequently rain results, was necessary owing to the method by which cloud areas were manually determined from the densitometer display.

Since the value of this method has been shown by means of relatively crude data, the advantages of a fully-automated technique are numerous. Not only will data analysis time be reduced, but the accuracy offered by use of the taped, rather than the analog, data will be a major improvement, particularly for the area measurements. Additionally, no corrections need be made for densitometer drift or image changes caused by photographic processing, transmission line noise, etc. The cloud threshold levels need not be converted into density units, and no difficulties result from image magnification.

Subsequent use of the taped data by the NHEML will build on the experience of SSEC with McIDAS as well as on that of the NHEML with digitized radar. It is envisioned that the navigation and mapping routines (Martin and Sikdar 1973) and the normalization routines (Mosher, 1973) will be beneficially combined with digitized radar echo tracking software. As described in Wiggert and Ostlund (1975) the capability of a computer to isolate, identify and follow a field of digital echo data over a period of

---

27 Man computer Interactive Data Access System, Space Science and Engineering Center, Madison, Wisconsin.

28 Image Display and Manipulation System, NASA, Goddard Space Flight Center, Greenbelt, Maryland.

time (namely, the program TRACK) is proven and has been used since 1973 to evaluate Florida rainfall. This is conceptually similar to a human identifying and following cloud entities from a sequence of satellite images. The application of TRACK to a sequence of satellite data should then be relatively straightforward.

The goal of computerization is to convert TRACK into a general form that will be applicable to areas ranging from the meso- to the global scale with a meteorologically reasonable spatial resolution available for all scales. Ideally, the program would be independent of machine memory size and independent of special capabilities, such as partial work access. However, tape and disk (or drum) capabilities would be needed. The program would be composed of three major functions: the first does the pre-processing of navigation and normalization, and the second collects cloud information necessary to the rain calculations performed by the third. The required information minimally consists of entity designation (including a unique identifier, centroid location, and time of scan), area measurements at specified brightness thresholds (both total aarea within the defined geographic target), maximum cloud area at the 80 D.C. threshold, and the time interval to the next image. It is proposed that mass storage be of the following types: (1) an input tape of digital satellite data, (2) disk file storage of all cloud entity information, and (3) a save capability for the entity information in either file or tape form. To achieve the goal of machine independence, the current isolation algorithm of TRACK must be revised. Presently, the entire field of data from one radar scan is stored in memory during echo isolation, and the target area of calculation is then restricted by available core. An algorithm using only two east-west satellite scan lines of data in memory at any one time is planned. In this manner, total dedication of any single computer will not be necessary for running this program.

It may seem that the programing goals outlined here are rather grandiose. But a thoughtfully developed, efficient program will be better suited to any applications that may arise and the potential of the satellite rain estimation methodology warrants such careful design. Within the NHEML, this methodology is being applied to three distinct problems: the evaluation of extra-area effects from cumulus seeding (in the context of the Florida Area Cumulus Experiment), the derivation of a rain atlas for the tropical Atlantic Ocean (with the NOAA GATE Office), and, during the hurricane season, the estimation of flood potential for storms (data provided to NOAA's National Hurricane Center). In terms of other applications, precipitation estimates will enable accurate energy budget calculations to be made. Verification of global weather models will be possible from the satellite-generated rainfall, especially over the oceans, where data is sparse. Certainly, an automated methodology would be of interest to such agencies as the WMO or the National Weather Service for providing near-real time rainfall data.

It is estimated that the computerization outlined here would take 6 months to complete. The cost would be absorbed by the NHEML budget.

Acknowledgment: The details of the computerization have been formulated by John Stewart.

☆U.S. GOVERNMENT PRINTING OFFICE: 1976 — 677-347 / 1253 REGION NO. 8